EMISSION MECHANISMS OF InGaN-BASED

III-NITRIDE HETEROSTRUCTURES

By

GORDON H. GAINER, JR.

Bachelor of Science
The Ohio State University
Columbus, Ohio
1982

Master of Science
Air Force Institute of Technology
Wright-Patterson AFB, Ohio
1987

Submitted to the Faculty of the
Graduate College of the
Oklahoma State University
in partial fulfillment of
the requirements for
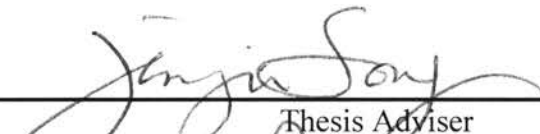the Degree of
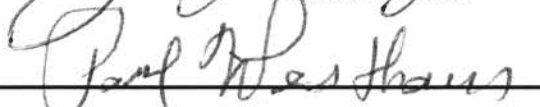DOCTOR OF PHILOSOPHY
August, 2001

EMISSION MECHANISMS OF InGaN-BASED

III-NITRIDE HETEROSTRUCTURES
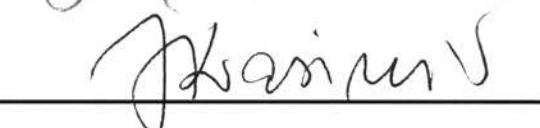
Thesis Approved:
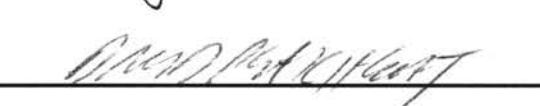
_____

Thesis Adviser

_____

_____

_____

_____

_____
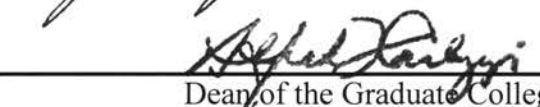
Dean of the Graduate College

ACKNOWLEDGEMENTS

TABLE OF CONTENTS

iv

LIST OF FIGURES

NOMENCLATURE

AFM   atomic force microscopy

BX   bound exciton

CL   cathodoluminescence

ELO   epitaxial lateral overgrowth

ELOG   epitaxial laterally overgrown GaN

LEO   lateral epitaxial overgrowth

FWHM   full width at half maximum

FX   free exciton

HVPE   hydride vapor phase epitaxy

LD   laser diode

LED   light emitting diode

MD-SLS   modulation-doped strained-layer superlattice

MOCVD   metal organic chemical vapor deposition

MQW   multiple quantum well

NSOM   near-filed scanning optical microscopy

PL   photoluminescence

PLE   photoluminescence excitation

QW   quantum well

RT   room temperature (~300 K)

SCH	separate confinement heterostructures
SE	stimulated emission
SL	superlattice
STL	scanning tunneling microscope-induced luminescence
STM	scanning tunneling microscopy
TE	transverse electric
TEM	transmission electron microscopy
TM	transverse magnetic
TRPL	time resolved photoluminescence
UV	ultraviolet
XRD	x-ray diffraction

CHAPTER I

INTRODUCTION

The Group III-nitride semiconductors, including InN, GaN, AlN, and their alloys,
have received a tremendous amount of attention over the past few years, mostly because
of the recent realization of high brightness blue and green light emitting diodes (LEDs)
and violet laser diodes (LDs), all of which use InGaN alloy active regions.[1] Amazingly,
this is despite a very large defect density. Initially, this was more of an art than a science,
as researchers tried to figure out why these devices worked. Optical studies, such as
those presented in this thesis, identified the emission mechanism of these devices as the
recombination of localized electrons and holes. The charge carriers are localized by
certain rather harmless defects, which prevent the carriers from diffusing to other defects
that are nonradiative recombination centers. Using defects for carrier localization is a
drastic change from the goal of eliminating defects. Ideally, the devices would work
better with no defects, but crystal growers have been unable to achieve very low defect
densities in Group III-nitrides, as they have in GaAs and Si. Many experiments that
pointed to carrier localization as the spontaneous emission mechanism could also be
explained by the presence of an internal electric field caused by piezoelectric and
spontaneous polarizations, although the internal electric field hinders rather than helps the
radiative recombination. Also, many researchers suspected that recombination in an
electron-hole plasma is the stimulated emission mechanism in InGaN-based LDs. This

1

thesis outlines studies that resolved these debates in favor of carrier localization at defects. This thesis also describes the lateral epitaxial overgrowth technique, which has been used to lower the density of harmful defects and improve device performance and longevity.

CHAPTER II

THEORIES FOR OPTICAL EMISSION FROM InGaN-BASED STRUCTURES

In this chapter, we describe the mechanisms proposed to explain the optical processes in InGaN-based structures. We will also present evidence that these mechanisms play a role in the emission processes. First, we will examine carrier localization at potential fluctuations caused by alloy fluctuations and/or phase separation into In-rich regions. Next, we will describe the effects of internal electric fields created by strain-induced piezoelectric polarization and spontaneous polarization. Finally, we will discuss theories for the stimulated emission – recombination of localized carriers and recombination in an electron-hole plasma.

Carrier Localization at In-Rich Regions

Many researchers have claimed that the spontaneous emission in InGaN/GaN quantum wells (QWs) is due to the recombination of carriers localized at band tail states of potential fluctuations.[2-5] Such potential fluctuations may be caused by alloy disorder, impurities, interface irregularities, and/or self formed In-rich quantum dot-like regions in the QW active regions. It is believed that carrier localization greatly improves the radiative quantum efficiency by preventing carriers from laterally diffusing to nonradiative recombination centers.[6-8] Through cross-sectional transmission electron microscopy (TEM) and energy-dispersive x-ray microanalysis, Narukawa *et al.* found

self-formed quantum dot-like structures in the wells of $In_{0.20}Ga_{0.80}N/In_{0.05}Ga_{0.95}N$ purple laser diode structures.[7] They showed that the quantum dot-like structures had a higher In concentration than the surrounding material and had an average diameter of about 3 nm. They said the radiative recombination in these multiple quantum wells (MQWs) is mainly due to excitons highly localized at deep traps probably originating from phase-separated In-rich regions acting as quantum dots.[7,8] It was suggested that the self-formation of quantum dots may be due to the intrinsic nature of InGaN ternary alloys to minimize energy by segregating into phases with higher and lower In composition. Nistor et al. used TEM to see quantum dots spontaneously formed in a 280 nm thick $In_{0.22}Ga_{0.78}N$ layer.[9] These quantum dots had sizes of 1.5 – 3 nm. The potential fluctuation due to the In composition modulation is further enhanced by the large bowing of the InGaN bandgap as a function of In composition. The bandgap (E_g) of $In_xGa_{1-x}N$ is given by

$$E_{g,InGaN}(x) = (1-x)E_{g,GaN} + xE_{g,InN} - bx(1-x), \tag{1}$$

where $E_{g,GaN}$ ($E_{g,InN}$) is E_g of GaN (InN) and b is the bowing parameter. The bowing parameter for $In_xGa_{1-x}N$ is much larger than expected and is strongly dependent on the In composition x, as shown by experimental and theoretical studies of the bandgap of strained $In_xGa_{1-x}N$ epilayers (e.g., $b \approx 3.2$ eV for $0 < x < 0.2$ and $b \approx 3.8$ eV for $x = 0.1$).[10-12] However, disagreements in the value of the bowing parameter have been caused by varying degrees of bandgap inhomogeneity and lattice mismatch induced strain. By taking into account the strain and by measuring the In composition through Rutherford backscattering, Pereira et al. obtained a room temperature bandgap dependence of $E_{g,InGaN}(x) = 3.39 - 3.57x$ in eV, with $b = 0$.[13]

Evidence of InGaN alloy composition fluctuations has also been obtained through submicrometer spatial resolution luminescence techniques, such as cathodoluminescence (CL), near-field scanning optical microscopy (NSOM), and scanning tunneling microscope-induced luminescence (STL). CL, NSOM, and STL complement high resolution topographs simultaneously obtained by scanning electron microscopy, shear-force microscopy, and scanning tunneling microscopy (STM), respectively. These techniques provide spectral and spatial mapping of important chemical and physical quantities.

CL has revealed spatial variations in luminescence from InGaN/GaN QW structures[14,15] and GaN films.[16-18] Chichibu et al. obtained spatially resolved CL map images at 10 K of InGaN/GaN single QWs grown by metalorganic chemical vapor deposition (MOCVD).[14] The 3 nm thick InGaN well layers had In contents of 5, 20, and 50%. Both uncapped samples and samples capped with a 6 nm undoped GaN layer were studied. Chichibu et al. observed an In-rich cluster size of less than 60 nm (the spatial resolution of the CL mapping technique, which is limited by the diffusion length of the material). Zhang et al. measured spatially-resolved and time-resolved CL of a MOCVD-grown InGaN/GaN single QW at 93 K.[15] The InGaN layer had a 15% average In composition, was 4 nm thick, and was capped by a 70 nm thick GaN layer. They observed local In alloy fluctuations on a scale of less than ~100 nm for low excitation conditions, indicating strong carrier localization at In-rich regions. The time-resolved CL revealed that carriers generated near the boundaries of the In-rich regions tend to diffuse toward and recombine at the In-rich centers, with strong lateral excitonic localization before radiatively recombining.

NSOM provides optical spectroscopy and mapping with a spatial resolution much better than the diffraction limit.[19-23] NSOM has three modes: (i) *illumination mode*, in which the near-field probe is a tiny light source, (ii) *collection mode*, in which the near-field probe is a tiny light detector, and (iii) *illumination-collection mode*, in which the near-field probe is both a tiny light source and detector. The illumination mode spectra are more affected by carrier diffusion and relaxation, causing poorer spatial resolution than in the other modes. Crowell *et al.* studied larger defects in an InGaN single QW by NSOM illumination through a tapered silver-coated optical fiber with a ~100 nm diameter aperture.[24] Their spatially-resolved spectra showed no evidence of localized carrier recombination at temperatures above 50 K. Their results differed very much from the above CL studies,[14,15] probably because of longer carrier diffusion lengths in their higher temperature and higher injection NSOM experiments. Vertikov *et al.* performed reflection NSOM for InGaN epilayers and QWs in the illumination mode using an aluminum-coated fiber probe with a 100 nm size aperture[25] and in the collection mode using an aluminum-coated fiber probe with a ~50 nm size aperture.[26] The collection mode measurements showed In alloy fluctuations typically occurring over 100 nm.

STL uses current through a STM tip (that almost touches the surface) for CL with high spatial resolution.[27] STL was measured for GaN grown by HVPE (hydride vapor phase epitaxy),[28] and Evoy *et al.* measured STL fluctuations on a scale of 30 – 100 nm for a MOCVD-grown InGaN/GaN MQW.[29] However, STL images of the InGaN/GaN MQW showed a smooth variation in luminescence intensity, instead of abrupt dark spots, which would be expected for local In composition fluctuation.

The recombination of localized carriers is governed not only by radiative recombination but also by the nonradiative transfer to and trapping in energy tail states.[8] The effective carrier lifetime τ_{eff} is given by

$$\frac{1}{\tau_{eff}} = \frac{1}{\tau_r} + \frac{1}{\tau_{nr}},\qquad(2)$$

where τ_r is the radiative lifetime and τ_{nr} is the nonradiative lifetime. The nonradiative processes include multiphonon emission, capture and recombination at impurities and defects, Auger recombination, and surface recombination, as well as diffusion of carriers away from the region of observation. Assuming a radiative efficiency η of 100% at T = 10 K, the radiative efficiency as a function of temperature is expressed as

$$\eta(T) = \tau_{eff}(T)/\tau_r(T) \approx I_{PL}(T)/I_{PL}(10\ K).\qquad(3)$$

From the above two equations, one can determine the radiative and nonradiative lifetimes as a function of temperature. Although electrons in upper localized states may radiatively decay to hole levels, they usually nonradiatively decay to lower localized states, from which they may then radiatively decay to hole levels. This causes a redshift of the emission peak and a broadening of the absorption tail. Higher excitation densities cause band filling, which blueshifts the emission peak by causing the electrons to have a higher average emission energy. Since electrons in upper states have more decay options (more lower states to nonradiatively decay to) than electrons in lower states, the upper electrons have a smaller nonradiative lifetime. This causes the upper transition energies to have a shorter effective lifetime. Therefore, an effective lifetime that decreases with increasing emission energy (or equivalently, a redshift with increasing time after an

7

excitation pulse) is evidence that the emission is due to radiative recombination of localized carriers. The effective lifetime is given by[30]

$$\tau_{eff} = \frac{\tau_r}{1 + \exp[(E - E_{me})/E_0]}, \tag{4}$$

where E is the emission energy, E_{me} is similar to a mobility edge,[31] and E_0 is the depth of the potential fluctuations.

<center>Piezoelectric and Spontaneous Polarization Fields</center>

Macroscopic polarization, consisting of (i) the piezoelectric polarization due to lattice-mismatch-induced strain and (ii) the spontaneous polarization due to interface charge accumulations between two materials, is very strong in wurtzite Group III-nitrides.[32-42] Electric polarization fields are common in strained-layer superlattices (SLs) of III-V semiconductors.[43] For the most commonly studied case of strained-layer SLs of zinc-blende material grown in the [100] direction, the piezoelectric effect does not occur, because only diagonal strain components are present and diagonal strains do not cause an electric polarization in zinc-blende crystals. Growth in any other direction causes off-diagonal strain components, and therefore, an electric polarization. For example, with a [111] growth axis in zinc-blende structures, the polarization vector points along the growth axis (perpendicular to the layers). Since one of the SL materials is in biaxial tension whereas the other is in biaxial compression, the polarization polarity reverses at the SL interfaces. These large alternating electric fields significantly change the SL electronic structure and optical properties. Similarly, wurtzite Group III-nitride layers grown in the [0001] direction, with biaxial strain from lattice mismatch, have large

<center>8</center>

piezoelectric fields due to their large piezoelectric constants (*e.g.*, e_{31} = –0.35, –0.57, and –0.57 C/m^2 for GaN, InN, and AlN respectively).[32,44] The piezoelectric polarization creates an internal electric field in the [0001] growth direction of wurtzite Group III-nitride layers.

Spontaneous polarization has long been observed in ferroelectric materials. *Ab initio* studies of the wurtzite Group III-nitrides found that due to their low-symmetry crystal structure, they have very large spontaneous polarization constants (*e.g.*, –0.029, –0.032 C/m^2, and –0.081 for GaN, InN, and AlN respectively).[32] The large spontaneous polarization was also experimentally observed as an internal electric field present with zero strain.[45] The spontaneous polarization increases with increasing nonideality of the structure, going from GaN to InN to AlN. The spontaneous polarization of AlN is only about 3–5 times smaller than that of typical ferroelectric perovskites. Spontaneous polarization is much more important for GaN/AlGaN QWs than InGaN/GaN QWs, because the spontaneous polarization constants are very different for GaN and AlGaN, but close for InGaN and GaN.

The polarizations create an electric field in QWs, tilting the conduction and valence band edges, which changes the subband energy levels and bound state wave functions, and hence, the optical transition energies and oscillator strengths. This is called the quantum-confined Stark effect.[46] Quantum confinement prevents the electric field from ionizing excitons, but the electric field spatially separates electrons and holes, which decreases the overlap of their wave functions, and therefore, decreases the radiative recombination rate and increases the radiative lifetime. The tilting of the bands in a QW also redshifts luminescence, since electrons and holes that are spatially separated

to opposite sides of the well can then recombine with an energy difference less than the bandgap, as illustrated in Figure 1. This is called the quantum-confined Franz-Keldysh effect, and its redshift (Stokes shift) increases with increasing well width. To a lesser extent, part of the absorption edge is also redshifted, resulting in a low-energy absorption tail below the fundamental energy gap. This can be thought of as photon assisted tunneling. At small well widths, quantum-confinement causes small blue shift in emission energies, but at larger well widths, the Franz-Keldysh redshift is dominant. These effects of the polarization fields can be partially reversed with high optical excitation densities, resulting in a high density of electrons and holes, because the internal electric field moves the electrons and holes to opposite sides of the well, creating another electric field in opposition to the original electric field. Very high excitation densities also remove the effects of the polarizations, through plasma screening of the electric field. Of course, the effects of the polarizations can also be removed by applying a voltage in opposition to the internal electric field or by electrically shorting both sides of the well. As time proceeds after a high excitation pulse and as the carrier density falls back down, we see a redshift of the emission peak, a broadening of the absorption tail, and an increase in the radiative lifetime. Unfortunately, these are the same evidences of carrier localization.

The emission peak position that is shifted by piezoelectric and spontaneous polarizations in wurtzite structures can be calculated from the following equations. First, the strain ε_{xx} in a layer in the direction parallel to the layer is given by[47]

$$\varepsilon_{xx} = \varepsilon_{yy} = (a_s - a_e)/a_e = -\frac{C_{33}\varepsilon_{zz}}{2C_{31}},$$ (5)

where a_s is the strained in plane lattice constant, a_e is the equilibrium unstrained lattice constant, the ε_{ij} are components of the piezoelectric tensor, and the C_{ij} are stiffness constants. The piezoelectric polarization normal to the layer is[47]

$$P_{pz} = 2\left(e_{31} - \frac{C_{13}}{C_{33}} e_{33}\right)\varepsilon_{xx}, \tag{6}$$

where the e_{ij} are the piezoelectric constants. For bulk material, the built-in internal electric field arising from the polarization (and not including any externally applied electric field) is $\bar{E} = -\bar{P}/\varepsilon_o$, where ε_o is the permittivity of free space. This is the same as the electric field between capacitor plates in a vacuum and with opposite charge densities of $\sigma = \pm P$. One would expect the opposite charges on opposite sides of the unit crystal cells to cancel each other, but instead, there is a macroscopic electric field, as though the charges cancel everywhere but at the surfaces. For a quantum well, we use $\bar{D} = \varepsilon_o \varepsilon \bar{E}$ and $\left(\bar{D}_w - \bar{D}_b\right)\cdot \hat{n}_{bw} = \sigma$, where $\bar{D}$ is the displacement vector, the subscripts w and b are for the well and barrier, respectively, ε is the relative permittivity, and $\hat{n}_{bw}$ is the unit vector normal to the layers and pointing from a barrier to an adjacent well, to obtain[34]

$$\left(\varepsilon_w \bar{E}_w - \varepsilon_b \bar{E}_b\right)\cdot \hat{n}_{bw} = \frac{\bar{P}_b - \bar{P}_w}{\varepsilon_o}, \tag{7}$$

For a periodic structure of many wells and barriers,

$$l_w E_w + l_b E_b = 0, \tag{8}$$

where l_w and l_b are the thicknesses of the wells and barriers, respectively. From Equations 6 and 7, we obtain[34]

$$E_w = \frac{(P_b - P_w)/\varepsilon_o}{\varepsilon_w + \frac{l_w}{l_b}\varepsilon_b} \tag{9}$$

For a single quantum well with very thick barriers ($l_b \to \infty$), we have

$$E_w = \frac{P_b - P_w}{\varepsilon_o \varepsilon_w} . \tag{10}$$

The electric field in the well should also include the photogenerated areal charge density σ at the well interfaces, and the polarizations should include both the piezoelectric and spontaneous components, so E_w in a single quantum well is more thoroughly given by[34,48]

$$E_w = (\sigma + P_b^{pz} + P_b^{sp} - P_w^{pz} - P_w^{sp})/(\varepsilon_0 \varepsilon_w), \tag{11}$$

where the superscripts pz and sp are for piezoelectric and spontaneous polarization, respectively. The photogenerated charge carriers are assumed to concentrate only at the well interfaces, pushed by the internal electric field, and this assumption gives accurate emission energy calculations for well thicknesses greater than about 2 nm and sheet carrier densities less than 4×10^{12} cm^{-2}.[48] Also, the sign of σ in Equation 11 is chosen opposite to that of $P_b^{pz} + P_b^{sp} - P_w^{pz} - P_w^{sp}$. However, for the low excitation densities typical of photoluminescence (PL) experiments, σ is negligible. If $E_w > 0$, electrons in the well are pushed toward the substrate.

Once the electric field in a well is known, the PL peak positions can then be estimated by assuming the wells have a triangular shape. The PL peak energy of a triangular well is[49,50]

$$E = E_g - |E_w| l_w + \frac{\eta_o (\hbar |E_w|)^{2/3}}{(2e)^{1/3}}\left(\frac{1}{m_e^{1/3}} + \frac{1}{m_h^{1/3}}\right) - E_B, \tag{12}$$

where E_g is the bandgap energy, E_w is the electric field in the single quantum well, l_w is the well thickness, η_o is the first positive zero of the Airy function (about 2.32), $\hbar$ is Planck's constant divided by 2π, e is the electronic charge, m_e and m_h are the electron and hole effective masses, respectively, and E_B is the exciton binding energy. However, the wells are not exactly triangular, and the barrier shapes also affect the emission energy. The PL peak energies can be more accurately determined by a one dimensional Poisson and Schrödinger equation solver,[51] in which areal charge densities of $\sigma + P_b^{pz} + P_b^{sp} - P_w^{pz} - P_w^{sp}$ are placed at the well interfaces.[34,48] One must also take into account that the exciton binding energy decreases with increasing well thickness, especially in an electric field which causes electron-hole separation.[48,52-54]

Takeuchi et al. proposed that piezoelectric fields due to lattice-mismatch-induced strain lead to the quantum-confined Stark effect in InGaN/GaN QWs, which causes a blueshift behavior with increasing excitation intensity and a well-width dependence of the luminescence peak energy.[37] They calculated a strain-induced electric field of 1.08 MV/cm, for strained $In_{0.13}Ga_{0.87}N$ grown on GaN, assuming $e_{31} = -0.22$ C/m^2. Since In composition fluctuations in ternary InGaN can also cause the luminescence redshift, Im et al. excluded this possibility by studying binary GaN in GaN/Al$_{0.15}$Ga$_{0.85}$N QWs through time-resolved photoluminescence (TRPL).[39] Their evidence for the piezoelectric effect was a redshift of the photoluminescence (PL) peak position and an increase in decay times with increasing well width from 1.3 to 10 nm. In fact, the PL peak shifted to energies well below the GaN bandgap for well thicknesses greater than 5 nm. They obtained similar results for $In_{0.05}Ga_{0.95}N$/GaN QWs, so they concluded that the piezoelectric field effect is important in both GaN/AlGaN and InGaN/GaN QWs.[40]

Figures 2, 3, and 4 show that there is a polarization-induced internal electric field in GaN/AlGaN separate confinement heterostructures (SCHs). The SCHs of this study are nominally identical except for different well thicknesses of 3, 5, 9, and 15 nm. The GaN wells were surrounded by 80 nm thick $Al_{0.07}Ga_{0.93}N$ waveguide layers and 150 nm $Al_{0.14}Ga_{0.86}N$ cladding layers. Figure 2 shows that the photoluminescence peak redshifts with increasing well thickness, although the recombination rate was reduced too much to see a photoluminescence peak from the 15 nm GaN well. Figure 3 shows the characteristic blueshift with increasing optical excitation density. The TRPL spectra of Figure 4 shows the expected increase in luminescence decay time with increasing well thickness. The TRPL from the 9 and 15 nm GaN wells was too weak to be seen, because of the greater electron-hole separation in thicker wells.

Although, using the binary GaN for the well, prevents the alloy and bandgap inhomogeneities typical of the ternary InGaN, the results obtained from GaN/AlGaN QWs may not necessarily extend to the case of samples with InGaN active regions with about 20% In content, such as the blue-light-emitting InGaN/GaN QWs. In fact, carrier localization from bandgap inhomogeneity can prevent the electron-hole separation that would otherwise be caused by a polarization-induced internal electric field. Also, the wells of commercial InGaN-based LEDs and LDs are typically 3 nm thick, which is less than the exciton Bohr radius of ~3.4 nm,[55] and therefore too thin for significant electron-hole separation in the direction of the internal electric field. (The exciton Bohr radius $a_B = \varepsilon \hbar^2 / \mu e^2$, where μ is the reduced mass of the electron and hole of the exciton.) In fact the existence of a Stokes shift and broadening of the luminescence from such thin InGaN wells is evidence for lateral bandgap inhomogeneity, which gives greater lateral

confinement.[55] Interestingly, Chow *et al.* theoretically calculated that the threshold current density of $In_{0.2}Ga_{0.8}N/GaN$ LDs is minimized with a well thickness of 3.5 nm, because although the slight electron-hole separation at this well thickness would tend to reduce the stimulated emission gain, it also reduces the spontaneous emission, which is a loss to the stimulated emission.[56]

We have reviewed only a small amount of the research showing evidence that strain-induced piezoelectric polarization and/or spontaneous polarization very much influence the carrier recombination in both GaN/AlGaN and InGaN/GaN QWs.[39,40,42] However, to understand the effects of the large the In content (~20%) on InGaN/GaN MQWs used in state-of-the-art commercialized blue-violet laser diodes, a comparison study of structural and optical properties is required, since any growth parameter changes may unexpectedly affect other structural (*e.g.*, quality and interface) properties, and hence, the optical and electrical properties.

Stimulated Emission and Lasing Mechanisms

Optically pumped lasing in GaN was first observed in GaN single crystal needles at 2 K by Dingle *et al.*[57] With the development of the MOCVD growth technique, many more studies of optically pumped stimulated emission (SE) and lasing have been performed for GaN and related heterostructures in recent years. Optical pumping, as illustrated in Figure 5, produces high carrier densities for SE and lasing, without the complicated doping, device processing, and electrical contacts that are required for electrical pumping. It is generally believed that the electron-hole separation caused by spontaneous and piezoelectric polarizations decreases the spontaneous and stimulated emission efficiencies[58-60] and that this reduction in emission efficiency should be greater

15

for larger well thicknesses.[61] However, the regions of interface irregularity are a greater fraction of the well volume for thinner wells and, therefore, cause more scattering loss, more broadening of the gain spectrum, and more nonradiative recombination for very thin wells. This is illustrated in Figure 6, which shows 10 K stimulated emission (SE) spectra of the $GaN/Al_{0.07}Ga_{0.93}N/Al_{0.14}Ga_{0.86}N$ SCHs (described in the previous section) at 1.5 times the SE threshold optical pumping density. The inset of Figure 6 shows the SE thresholds as a function of well thickness. The SE thresholds were 40, 60, and 180 kW/cm^2 for the 5, 9, and 15 nm thick GaN well samples, respectively, which is low compared to the typical value of ~130 kW/cm^2 for bulk GaN layers.[62] The SE thresholds decreased with decreasing well thickness, except that SE was not observed for the 3 nm thick GaN well sample. The SE threshold was lowest for the sample with a 5 nm thick GaN well, but the 3 nm well was too narrow for SE, most likely because of the greater influence of interface irregularity. This suggests that Group III-nitride-based UV LDs fabricated with narrower wells would have better performance, but if the well is too narrow, an elaborate interface control or multiple quantum well structures should be considered.

The SE gain mechanism for bulk GaN was identified by Bidnyk *et al.* as exciton-exciton scattering below 200 K and electron-hole plasma recombination (or band-to-band transition) above 200 K.[62] They found that the better optical and carrier confinement of a GaN/AlGaN separate confinement heterostructure enabled lasing in GaN by exciton-exciton scattering in tests as high as room temperature. For InGaN-based laser diode structures, several SE and lasing mechanisms were recently discussed by several groups.[7,63-67] Optical gain experiments were also performed on InGaN-based

16

structures.[68-74] Although electron-hole plasma recombination is accepted as the gain mechanism in most III-V semiconductors, such as GaAs and InP, there has been controversy over whether the SE in InGaN-based structures is also primarily by electron-hole plasma recombination. One would expect that without sufficient carrier localization to prevent electron-hole separation in InGaN layers, the SE pumping threshold is increased by the fact that it must first overcome the piezoelectric field.[75] Without sufficient carrier localization, the SE threshold could be so high that it would cause an electron-hole plasma. Of course this is a moot point for commercial InGaN-based MQW devices with longitudinal localization already provided by the narrowness of the 3 nm InGaN wells.[76] In this case, additional lateral localization is helpful in preventing carriers from migrating to nonradiative recombination channels, in making it easier to obtain a greater carrier density necessary for population inversion, and in restricting the electrons and holes so that they have nearly zero momentum (since the produced photons have nearly zero momentum, momentum conservation makes the electron-hole recombination much more efficient when the electron and hole have nearly equal, but opposite, momenta). In Chapters IV, V, and VI, we will resolve these issues and show that localized carrier recombination is the mechanism for both spontaneous and stimulated emission in state-of-the-art InGaN-based structures.
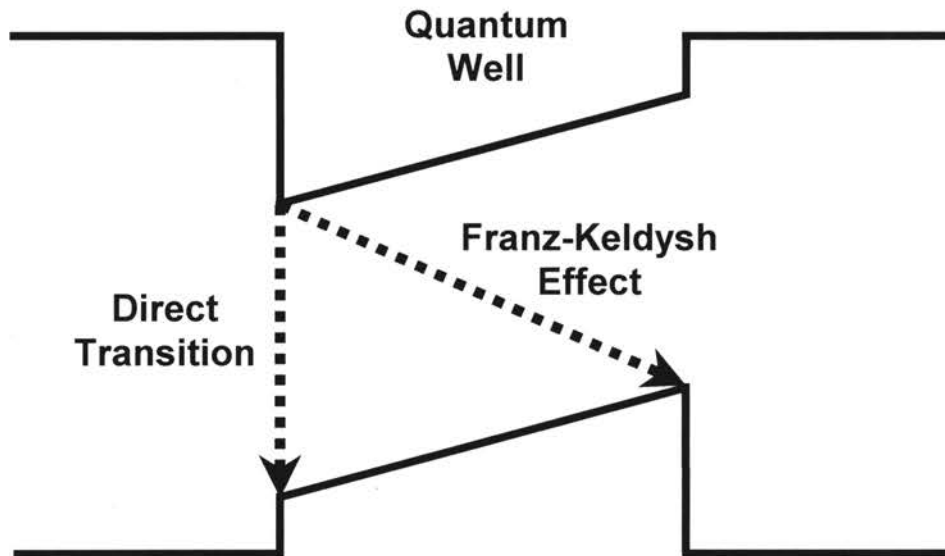
Figure 1. The quantum confined Franz-Keldysh effect enables electrons to recombine with holes with a smaller energy difference than for a direct transition.
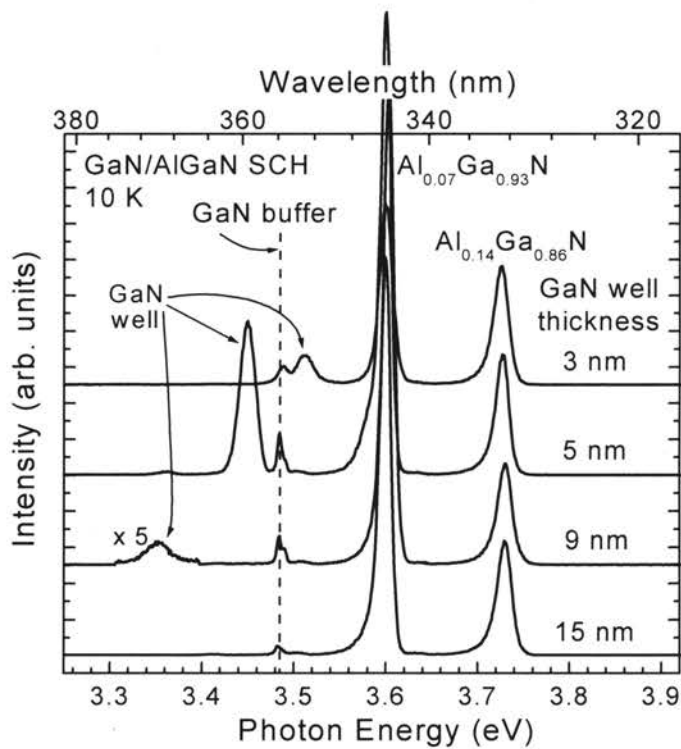
Figure 2. 10 K PL spectra of GaN/AlGaN SCHs with well thicknesses of 3, 5, 9, and 15 nm. The GaN well PL peak position is strongly dependent on the well thickness, because of an internal electric field. The spectra are displaced vertically for clarity.

18
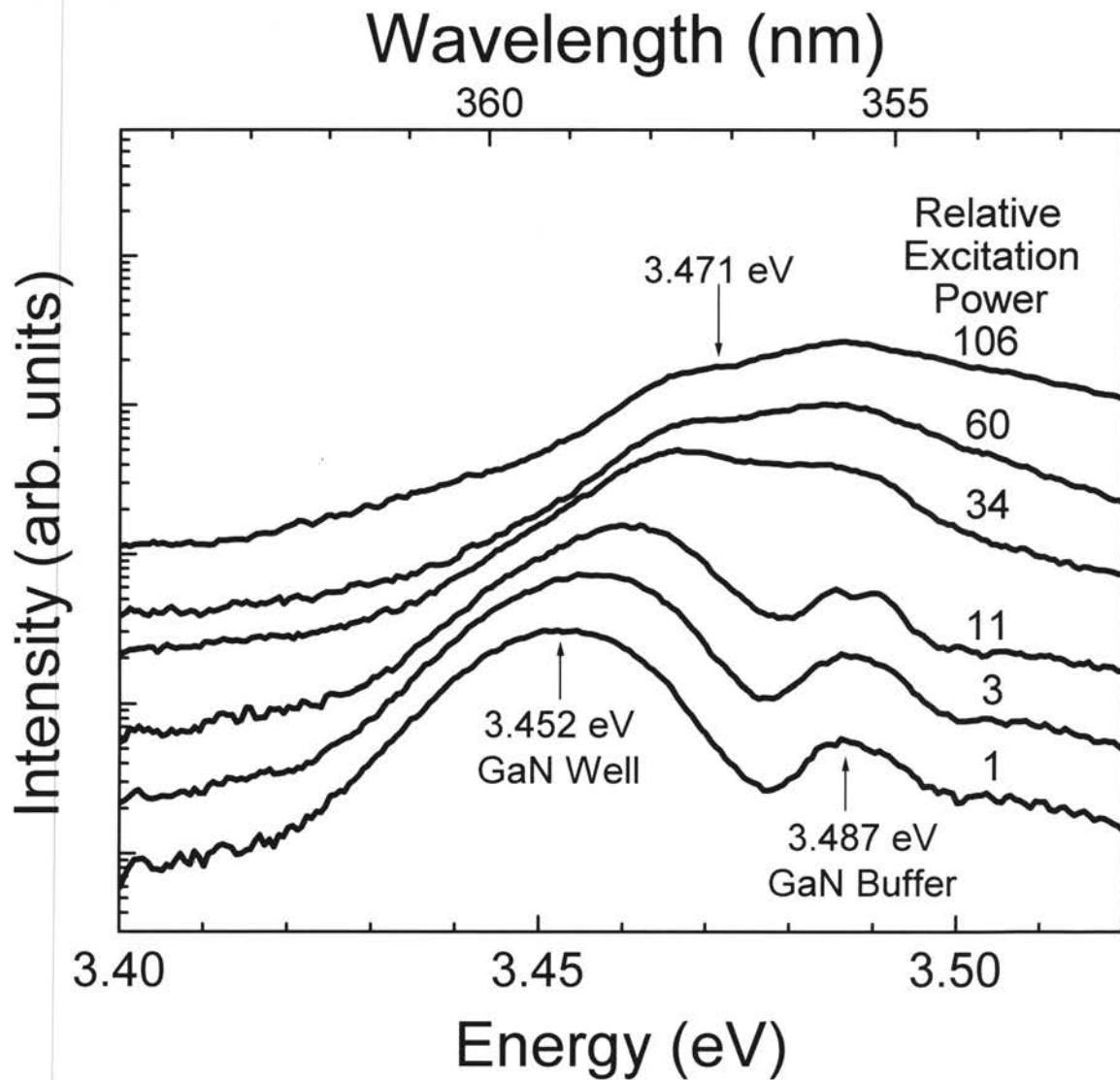
Figure 3. Power dependent PL spectra of a GaN/AlGaN SCH with a 5 nm well. Higher excitation powers shift the well PL peak closer to the position it would have in the absence of an internal electric field.
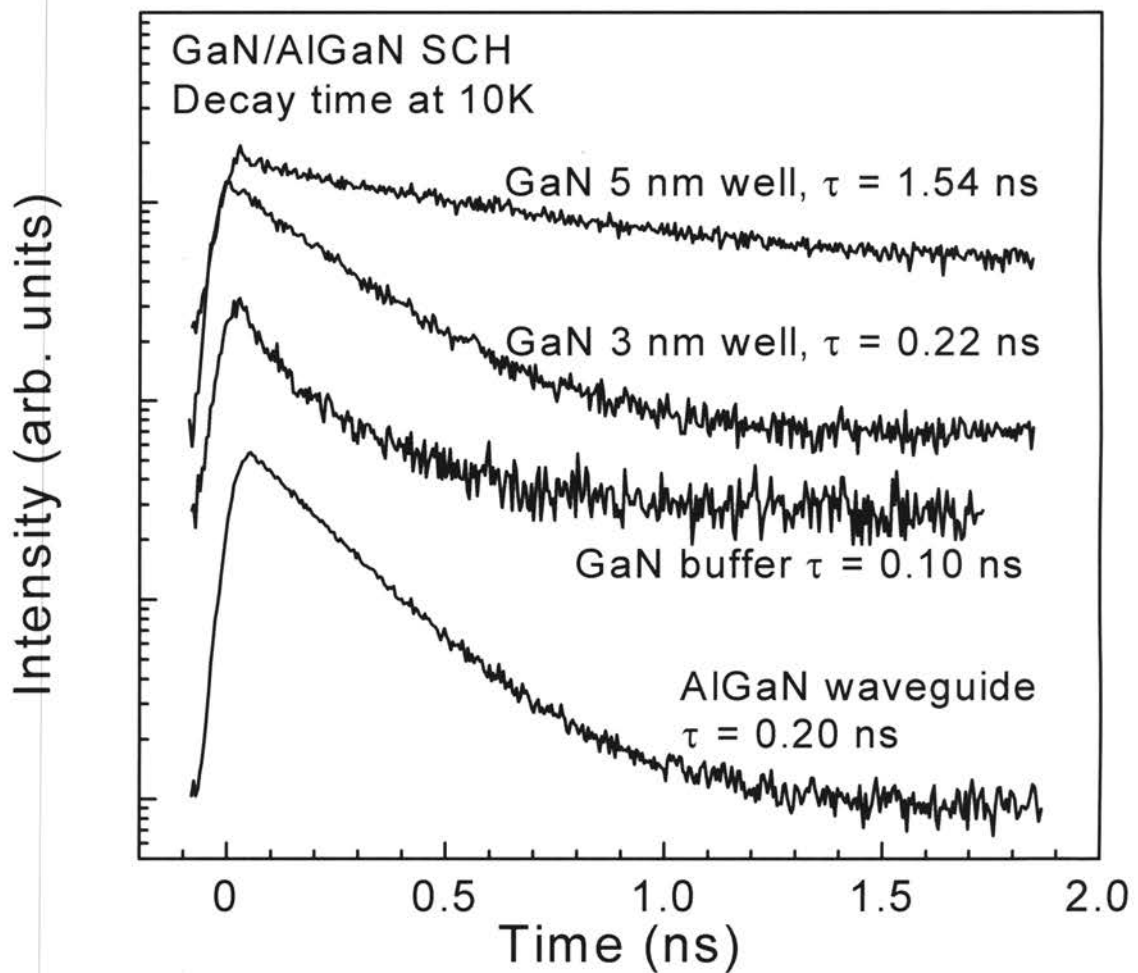
Figure 4. 10 K time-resolved photoluminescence decay for GaN well, GaN buffer, and Al$_{0.07}$GaN$_{0.93}$N waveguide layers. Greater electron-hole separation due to an internal electric field causes a longer lifetime τ in thicker wells.
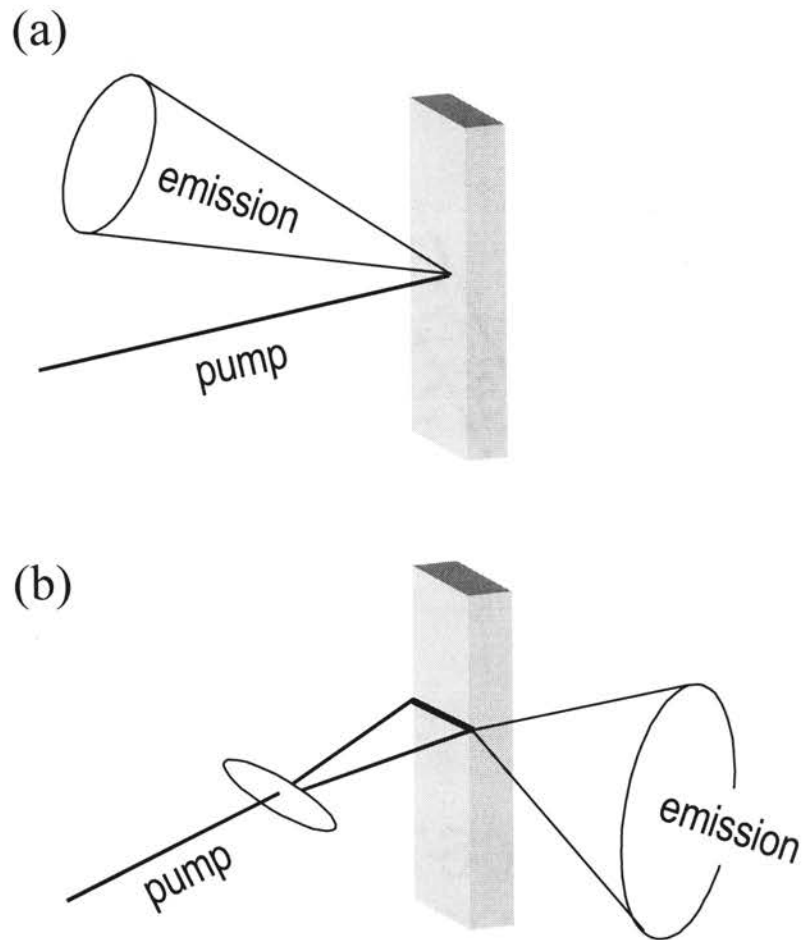
Figure 5. Optical pumping in (a) surface and (b) edge emission geometries.
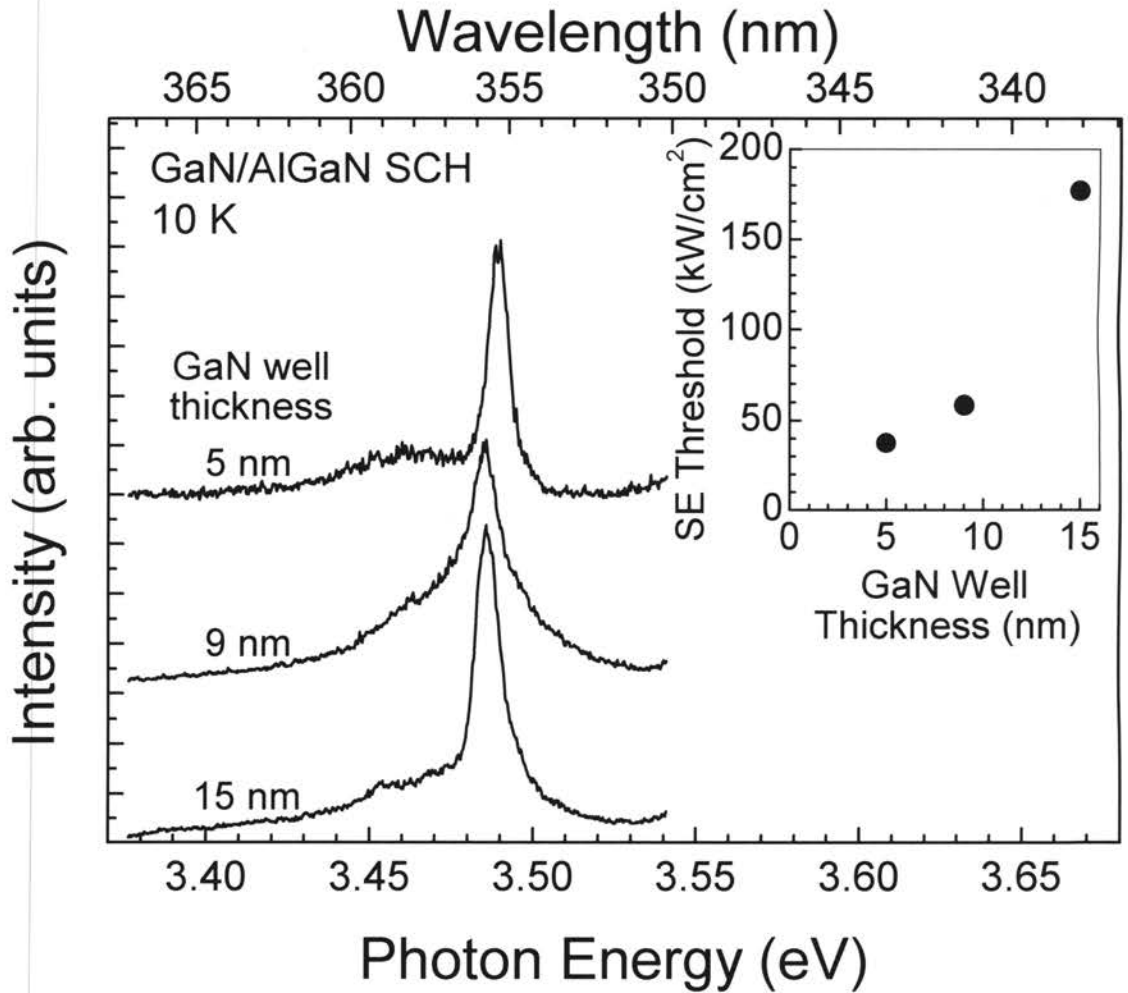
Figure 6. 10 K SE spectra for GaN/AlGaN SCHs with different well thicknesses. The SE peak is blue-shifted from the spontaneous PL peak due to screening of the internal electric field by photogenerated charge carriers. The spectra are displaced vertically for clarity. The inset shows that the SE threshold decreases with decreasing well thickness.

CHAPTER III

FUNDAMENTAL OPTICAL PROPERTIES OF InGaN-BASED STRUCTURES

In this chapter, we will discuss the general optical properties of InGaN epilayers and InGaN/GaN QWs, as well as explanations for these properties. Measurements were taken by a wide range of techniques to better understand both the spontaneous and stimulated emission. The optical emission, absorption, excitation power emission dependence, and emission temporal dynamics were investigated by PL, PL excitation (PLE), optically pumped emission, and TRPL, respectively.

The data presented in this chapter is for an $In_{0.18}Ga_{0.82}N$/GaN MQW and an $In_{0.18}Ga_{0.82}N$ epilayer. Both the MQW and the epilayer were grown on c-plane sapphire substrates by MOCVD, following the deposition of a 1.8 μm thick GaN buffer layer. The MQW consists of a 12-period superlattice with 3 nm thick $In_{0.18}Ga_{0.82}N$ wells and 4.5 nm thick GaN barriers, and a 100 nm thick $Al_{0.07}Ga_{0.93}N$ capping layer. The InGaN epilayer is 100 nm thick and capped by a 50 nm thick GaN layer. The 18% In composition in the wells was determined by x-ray diffraction analysis, assuming Vegard's law. X-ray symmetric and asymmetric reciprocal space mapping showed that the MQW is fully pseudomorphic (strained so that the MQW layers' lattice constants conform to that of the GaN buffer layer).[77]

In this chapter, we will see that the MQW and the epilayer have: (i) a large Stokes shift between the emission peak and the absorption band edge, (ii) a broadening of the

absorption tail, (iii) a blueshift of the emission peak with increasing excitation density, and (iv) a redshift of the emission peak with time (a rise in lifetime with decreasing emission energy). As explained in the previous chapter, for the epilayer, these characteristics can be qualitatively explained by both carrier localization and the piezoelectric field. However, for the MQW, only the carrier localization explanation applies. This is because the piezoelectric field would cause these characteristics through electron-hole separation, but the 3 nm thickness of the MQW $In_{0.18}Ga_{0.82}N$ wells is less than the exciton Bohr radius, and therefore too thin for enough electron-hole separation in the direction of the internal electric field, but the carrier localization gives greater lateral confinement. Nevertheless, in Chapters IV, V, and VI, we will see that carrier localization is the predominant explanation for both the MQW and the epilayer.

Optical Emission and Absorption Properties

Figure 7 shows typical 10 K PL and PLE spectra of InGaN emission from (a) an $In_{0.18}Ga_{0.82}N$/GaN MQW and (b) an $In_{0.18}Ga_{0.82}N$ epilayer, respectively. Both were grown by metalorganic chemical vapor deposition (MOCVD) on c-plane sapphire. The PL spectra (solid lines) were measured using the 325 nm line of a continuous wave (cw) He-Cd laser. The PLE spectra (dashed lines) were measured using quasimonochromatic light dispersed by a 1/2-m monochromator from a xenon lamp. In Figure 7, the InGaN emission has a peak energy of ~2.8 and ~2.99 eV at 10 K for (a) the $In_{0.18}Ga_{0.82}N$/GaN MQW and (b) the $In_{0.18}Ga_{0.82}N$ epilayer, respectively. The near-band-edge emission from the $Al_{0.07}Ga_{0.93}N$ cladding layer [in (a)] and the GaN layers [in (a) and (b)] are also clearly seen at 3.60 and 3.48 eV, respectively. With the PLE detection energy set at the InGaN emission peak, the contributions from the GaN layers [in (a) and (b)] and from the

$Al_{0.07}Ga_{0.93}N$ capping layer [in (a)] are clearly seen, and the absorption edges are well matched to the PL peak energy positions. The absorption of the InGaN wells in the MQW increases monotonically, reaching a maximum at ~3.1 eV, and remains almost constant until absorption by the GaN barriers begins at 3.48 eV. A large Stokes shift of the InGaN spontaneous emission peak with respect to the absorption edge measured by low power PLE spectroscopy is clearly observed for both samples. This Stokes shift is ~0.3 eV for the MQW and ~0.05 eV for the epilayer. The large Stokes shift between the emission and absorption edge is typical of InGaN epilayers and QWs. The Stokes shift and the broadening of the absorption edge of InGaN epilayers and diodes measured by many groups were plotted as a function of emission energy.[78,79] Both the Stokes shift and the absorption broadening were found to increase as the In composition increases, which causes the emission energy to decrease. The Stokes shift can be explained by carriers relaxing to deeply localized states before radiatively recombining. It can also be explained by an internal electric field caused by strain-induced piezoelectric polarization. The internal electric field would spatially separate electrons and holes, but an overlap of their wave functions would allow their radiative recombination at a lower energy than if there was no internal electric field. However, the narrowness of the MQW 3 nm wells prevents electron-hole separation.

<div align="center">

Excitation Density Dependence and Optically

Pumped Stimulated Emission

</div>

Figure 8 shows 10 K emission spectra as a function of excitation pump density (I_{exc}) for (a) the $In_{0.18}Ga_{0.82}N$/GaN MQW and (b) the $In_{0.18}Ga_{0.82}N$ epilayer. The spectra

of Figure 8 were measured with an excitation energy of 3.49 eV and in the surface emission geometry to minimize reabsorption. The SE peaks indicated by arrows in the figure are due to in-plane SE coming out the sample edges. No SE was observed from the middle of the samples in this geometry, indicating the high quality of the sample structures.[80] The pump spot size was ~1 mm^2 and the excitation wavelength was the 355 nm third harmonic of a Nd:YAG (yttrium aluminum garnet) laser. As I_{exc} increases, the spontaneous emission peak of the MQW blueshifts until it reaches ~2.9 eV, and then, it only increases in intensity until the SE threshold is reached. The SE peak develops on the low energy side of the spontaneous emission peak. As explained earlier, the blueshift of the epilayer spontaneous emission with increasing I_{exc} can be explained by both the band filling of localized states and the screening of the piezoelectric field. However, for the narrow wells of the MQW, the blueshift can only be due to the band filling of localized states. With increasing I_{exc}, the filling level increases and the PL maximum shifts to higher energies until sufficient population inversion is achieved and net optical gain results in SE. The excitation density induced blueshift is much larger for the MQW than the epilayer (~80 meV for the MQW compared to ~14 meV for the epilayer). Details of the SE features and optical nonlinearities of InGaN-based structures will be given in Sections III and IV, respectively.

Temporal Evolution and Dynamics of Optical Emission

The recombination decay times for the InGaN emission of InGaN epilayers and QWs are generally in the range of several hundreds of picoseconds to a few tens of nanoseconds, depending on the In composition of the InGaN layer, the number of QWs,

26

and other growth conditions.[3,81,82] Figure 9 shows the effective recombination lifetime as a function of detection energy across the 10 K PL spectrum of (a) the $In_{0.18}Ga_{0.82}N/GaN$ MQW and (b) the $In_{0.18}Ga_{0.82}N$ epilayer. TRPL was measured using a streak camera for detection and with sample excitation by the second harmonic of a cavity-dumped dye laser synchronously pumped by a frequency-doubled modelocked Nd:YAG laser. The excitation pulses had a duration of less than 5 ps. The overall time resolution of the system was better than 15 ps. Figure 9 shows a rise in the effective lifetime τ_{eff} with decreasing emission energy across the PL peak, resulting in a redshift of the emission peak energy with increasing time. The average lifetime for the MQW is about 12 ns, which is much larger than the 0.6 ns lifetime of the epilayer. The longer lifetime for the MQWs in this study compared to those reported by other groups may be due to a larger degree of carrier localization caused by a larger number of QWs and/or different growth conditions used in this study.[3,81-84]

Figure 10 shows τ_{eff} as a function of temperature for (a) the $In_{0.18}Ga_{0.82}N/GaN$ MQW and (b) the $In_{0.18}Ga_{0.82}N$ epilayer. The rise in τ_{eff} with increasing temperature from 10 to ~70 (30) K for the MQW (epilayer) indicates recombination dominated by radiative recombination over this temperature range, but the decrease in τ_{eff} with increasing temperature for $T > 70$ (30) K indicates the increasing dominance of nonradiative recombination at higher temperatures.[85,86] The MQW has a much larger τ_{eff} than the epilayer throughout the $10 - 300$ K temperature range, and the lifetimes of both are significantly larger than that of GaN epilayers and heterostructures.[81,87] This can be explained by potential fluctuations caused by nonrandom In composition fluctuations localizing carriers and preventing them from diffusing to nonradiative recombination

centers. The potential fluctuations can be caused by nonrandom alloy composition fluctuation, well size irregularity, and other crystal imperfections, such as point defects and dislocations. Lefebvre *et al.* found that well width and depth variations cause carrier localization in GaN/$Al_{0.07}Ga_{0.93}N$ QWs and cause the PL lifetime to decrease with increasing photon energy.[88] For the epilayer, the longer lifetimes can also be caused by electron-hole separation due to a strain-induced piezoelectric field, but the narrow 3 nm wells of the MQW prevent the electron-hole separation.

Effect of Quantum Wells and Interfaces on the Optical Properties

We saw that the $In_{0.18}Ga_{0.82}N$/GaN MQW and the $In_{0.18}Ga_{0.82}N$ epilayer have: (i) a large Stokes shift between the emission peak and the absorption band edge, (ii) a broadening of the absorption tail, (iii) a blueshift of the emission peak with increasing excitation density, and (iv) a redshift of the emission peak with time (a rise in lifetime with decreasing emission energy). Although, these characteristics can be explained by both carrier localization and the piezoelectric field, one would expect these characteristics to be weaker in the MQW. This is because the MQW's 3 nm thick wells are to thin to allow the piezoelectric effect to have much influence, and the MQW wells are too thin for much bandgap inhomogeneity in the longitudinal direction. However, these characteristics are much stronger in the MQW than the epilayer. The PL peak energy of the MQW is ~2.8 eV, which is ~190 meV below that of the epilayer (~2.99 eV). The MQW Stokes shift is ~0.3 eV, and the epilayer Stokes shift is only ~0.05 eV. The blueshift with increasing excitation density is ~80 meV for the MQW compared to ~14 meV for the epilayer. The 10 K emission lifetime of the MQW is 12 ns, which is much larger than the epilayer's 0.6 ns. The MQW had a much longer lifetime throughout

the 10 – 300 K temperature range studied. Since these characteristics are much stronger in the MQW, the MQW must have deeper and more extensive potential fluctuations in the lateral direction than the epilayer has in three dimensions. The fact that the emission lifetime increased with temperature up to 70 K for the MQW, compared to 30 K for the epilayer, indicates that the MQW lateral carrier localization is more effective in preventing carriers from diffusing to nonradiative recombination centers. Since the quality of lower layers and interfaces affects that of upper layers, the presence of interfaces may change the properties of the InGaN active region. In addition, the different growth conditions between the MQW and the epilayer may also affect the degree of potential fluctuations. We will see in Chapters IV, V, and VI, that carrier localization is the predominant explanation for the optical properties of the epilayer, as well as the MQW.
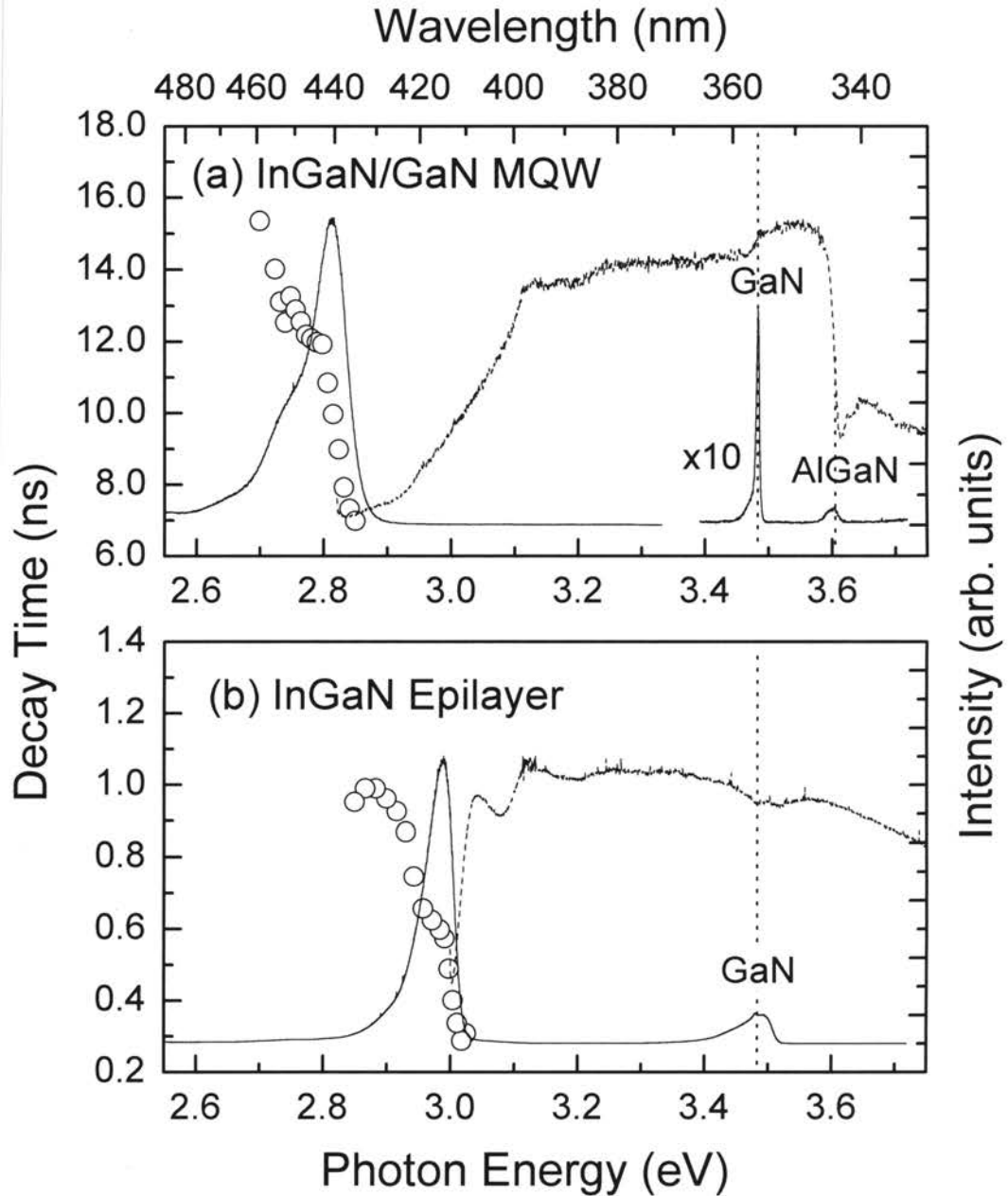
Figure 7. 10 K PL (solid lines), PLE (dashed lines), and decay time (circles) for (a) an
$In_{0.18}Ga_{0.82}N/GaN$ MQW and (b) an $In_{0.18}Ga_{0.82}N$ epilayer. Both were grown by
MOCVD on c-plane sapphire. A large Stokes shift of the PL emission from the InGaN
layers with respect to the band edge measured by PLE spectra is observed. The near-
band-edge emission from the GaN and $Al_{0.07}Ga_{0.93}N$ layers was observed at 3.48 and
3.6 eV, respectively. The PLE contributions from the GaN layers [in (a) and (b)] and the
$Al_{0.07}Ga_{0.93}N$ layer [in (a)] are clearly seen.
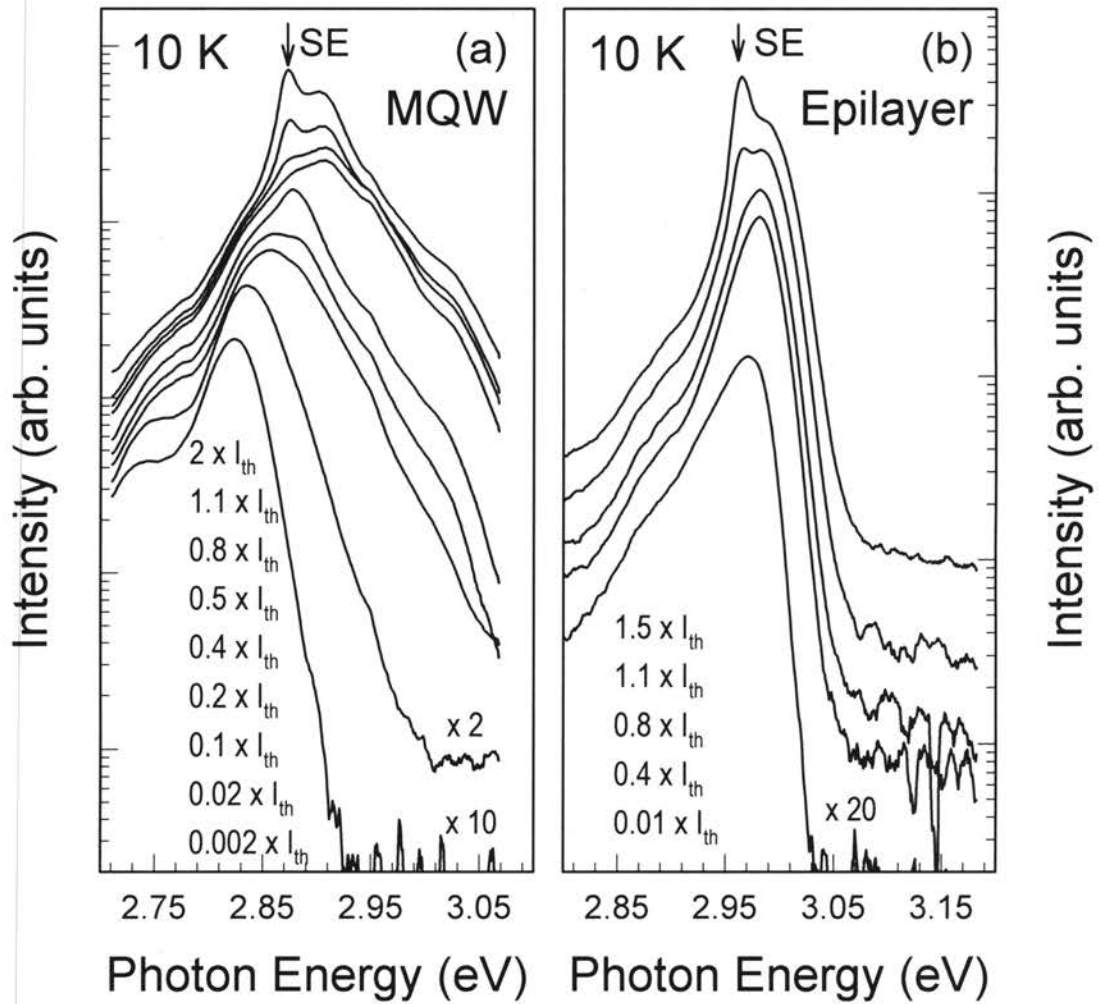
Figure 8. Evolution of InGaN emission spectra from below to above the SE threshold, I_{th}, at 10 K for (a) an $In_{0.18}Ga_{0.82}N/GaN$ MQW and (b) an $In_{0.18}Ga_{0.82}N$ epilayer. The emission was collected in a surface emission geometry. I_{th} for the MQW and epilayer was ~170 and 130 kW/cm^2, respectively, for the experimental conditions. A large blueshift of the emission is clearly seen with increasing excitation density for the MQW sample, showing band filling of localized states.
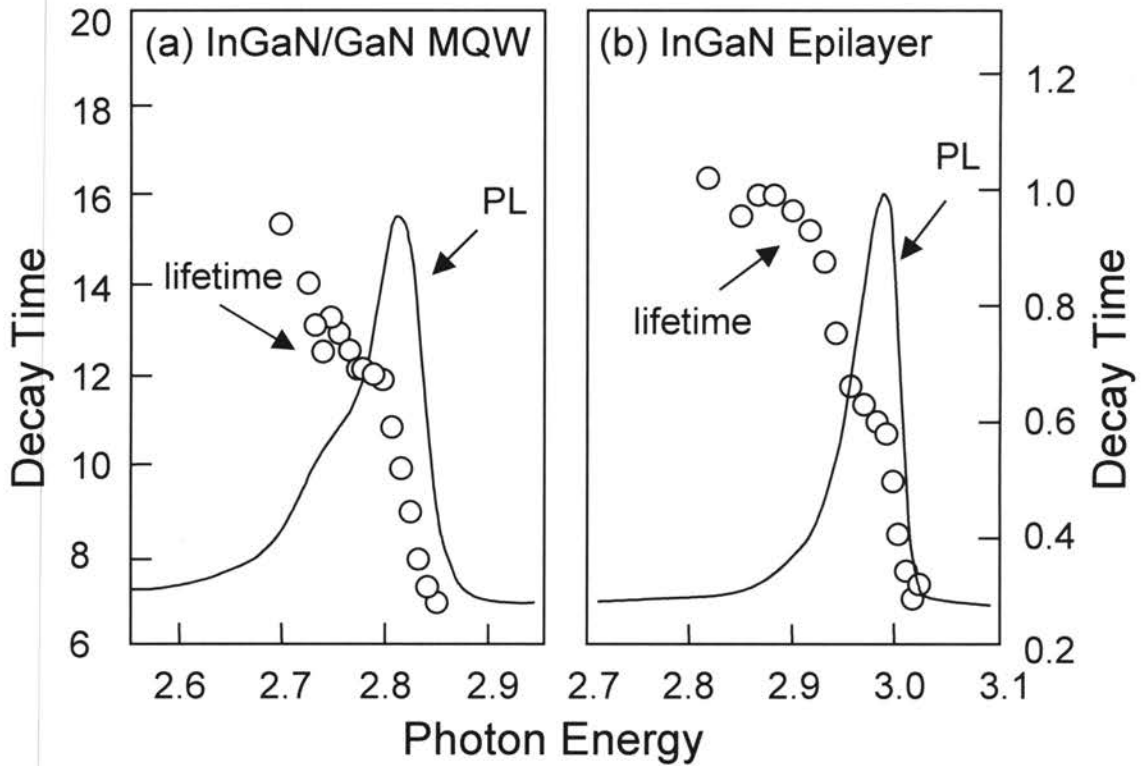
Figure 9. 10 K decay time (open circles) as a function of detection energy across the PL spectrum for (a) an $In_{0.18}Ga_{0.82}N$/GaN MQW and (b) an $In_{0.18}Ga_{0.82}N$ epilayer. A rise in lifetime with decreasing emission energy, resulting in a redshift behavior of the emission with time, reflects that the InGaN-related emission is due to radiative recombination of carriers localized at potential fluctuations.
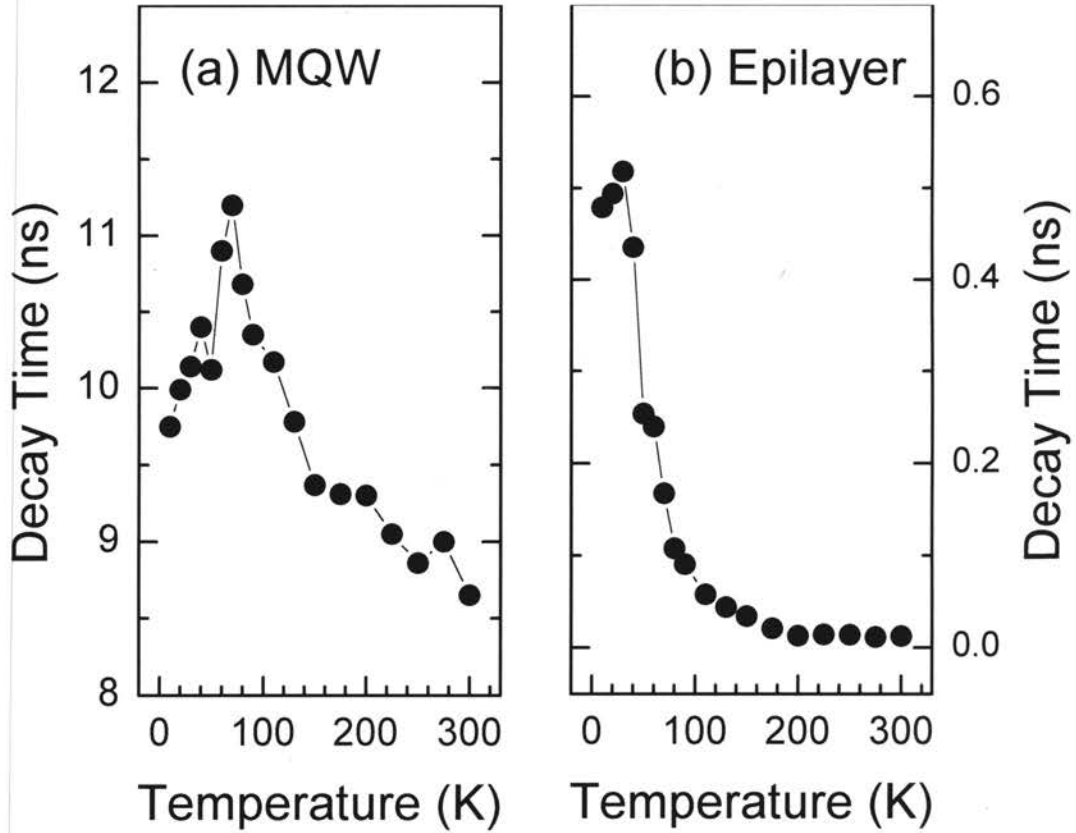
Figure 10. Temperature dependence of the lifetimes for (a) an $In_{0.18}Ga_{0.82}N$/GaN MQW and (b) an $In_{0.18}Ga_{0.82}N$ epilayer. The rise in effective recombination lifetime with increasing temperature observed from 10 to ~ 70 (30) K for the MQW (epilayer) is indicative of recombination dominated by radiative recombination channels, whereas the decrease in lifetime with increasing temperature for $T > 70$ (30) K indicates the increasing dominance of non-radiative recombination. We observed that the MQW has a significantly larger lifetime than the epilayer for all temperatures studied, and the lifetimes of both are significantly larger than that of GaN epilayers and heterostructures.

CHAPTER IV

In COMPOSITION AND Si DOPING EFFECTS ON OPTICAL TRANSITIONS

The emission characteristics of Group III-nitrides are influenced more than expected by the material combination (*e.g.*, GaN/Al$_x$Ga$_{1-x}$N or In$_x$Ga$_{1-x}$N/GaN), the active region alloy composition (*e.g.*, x < 0.1 or x > 0.15 in In$_x$Ga$_{1-x}$N /GaN QWs), and other structural properties (*e.g.*, well thickness, doping concentration, number of QWs, etc.). The growth conditions for the InGaAlN material system also affect the structural, electrical, and optical properties. The In composition dependence of optical and structural characteristics of In$_x$Ga$_{1-x}$N-based structures is very important for the design of optical devices and extending their wavelength range from UV to green-yellow. Although Si doping is typically used for *n*-doping in Group III-nitrides, Si doping also changes the growth mode, and thus, the optical performance. This chapter discusses the effects of In composition and Si doping on the optical and structural properties of InGaN/GaN heterostructures.

Influence of In Composition in InGaN Layers

An increase in the In composition of InGaN/GaN wells increases both the lattice mismatch induced strain (which leads to a stronger piezoelectric field) and In phase segregation (which causes more carrier localization). Martin *et al.* summarized the emission and absorption spectra of a range of commercial InGaN light-emitting diodes

and high-quality epilayers.[78] They showed that the Stokes shift depends linearly on the emission peak energy, using spectra of diode and epilayer samples, as well as data from research literature. The absorption edge broadening increases as the emission peak energy decreases. They explained these effects by the localization of excitons in In-rich quantum dots created by phase segregation. Narukawa *et al.* studied the temperature dependence of radiative and nonradiative recombination lifetimes in undoped $In_{0.02}Ga_{0.98}N$ UV-LEDs and determined that a small amount of In added to a GaN layer improves the external quantum efficiency by suppressing nonradiative recombination processes.[89] A recent study of the structural and optical properties of $In_xGa_{1-x}N/GaN$ MQWs with different In compositions is presented here.[90] The room temperature (RT) SE wavelengths of the samples studied are between 395 nm and 405 nm, which is near the operational wavelength of state-of-the-art violet current injection laser diodes.[91]

Figure 11 (a) shows 10 K PL and PLE spectra of MOCVD-grown $In_xGa_{1-x}N/GaN$ MQWs with different In compositions of 8.8, 12.0, and 13.3%. These samples consist of (i) a 2.5 μm thick GaN buffer layer doped with Si at 3×10^{18} cm^{-3}, (ii) a five-period superlattice of 3 nm thick undoped $In_xGa_{1-x}N$ wells and 7 nm thick GaN barriers doped with Si at $\sim 5 \times 10^{18}$ cm^{-3}, and (iii) a 100 nm thick GaN capping layer. Trimethylindium fluxes of 13, 26, and 39 μmol/min were used to grow samples with the different In compositions in the $In_xGa_{1-x}N$ wells, but the $In_xGa_{1-x}N$ well growth time was kept constant. The PLE detection energy was set at the main $In_xGa_{1-x}N$ PL peak. With increasing In composition, the $In_xGa_{1-x}N$ PLE band edge redshifts and broadens. These PLE band edges are similar to absorption spectra and can be fit to the sigmoidal

formula:[78]

$$\alpha = \frac{\alpha_0}{1 + \exp\left(\dfrac{E_{eff} - E}{\Delta E}\right)}, \tag{13}$$

to yield effective bandgaps (E_{eff}) of 3.256, 3.207, and 3.165 eV and broadening

parameters (ΔE) of 23, 36, and 40 meV for the samples with In compositions of 8.8,

12.0, and 13.3%, respectively. This broadening of the PLE spectra with increasing In

shows that the absorption states are distributed over a wider energy range due increased

fluctuations in dot size, shape, and/or depth[78] or due to increased interface imperfection,

as observed in x-ray diffraction (XRD) patterns.[88] The Stokes shift increased from about

135 to 180 meV as the In composition increased from 8.8 to 13.3%. The large Stokes

shifts and their increase with In composition can be explained by carrier localization[5,8] or

the piezoelectric effect,[41] or a combined effect of both mechanisms.[6,78] Clearly, both

mechanisms are in these samples, but the narrowness of the 3 nm wells prevents the

piezoelectric field from having much influence.

To check device applicability, SE was measured from the $In_xGa_{1-x}N/GaN$ MQWs

at RT, which is important as the normal device operating temperature. The SE spectra

shown in Figure 11 (b) were obtained at a pump density of $1.5I_{th}$, where I_{th} is the SE

threshold for each sample. When below I_{th}, as the excitation power density is raised, the

spontaneous emission peak blueshifts due to band filling of localized states, as shown

earlier. Raising the excitation power density above I_{th} causes much spectral

narrowing.[65] The emission spectra contain many narrow peaks of less than 0.1 nm full

width at half maximum (FWHM), which is on the order of the instrument resolution. The

SE threshold was 150, 89, and 78 kW/cm^2, for the samples with In contents of 8.8, 12.0, and 13.3%, respectively. These thresholds are approximately an order of magnitude lower than that of a high-quality nominally undoped single-crystal GaN film measured under the same experimental conditions.[92]

With increasing In composition from 8.8 to 13.3%, the SE threshold decreases while the FWHM of the high-resolution XRD SL-1 satellite peaks and the PLE band edge broadening increase. The increase in the SL-1 peaks FWHM with increasing In composition, indicates a decrease in interface quality due to nonuniform In incorporation into the GaN layers. The interface imperfection and composition inhomogeneity are also seen in the broadened band edge of the PLE spectra. Although the interface fluctuation is a source of scattering loss, and the broadening of the absorption states broadens the gain spectrum, the SE threshold density decreased with increasing In composition. This is contrary to traditional III-V semiconductors, such as GaAs and InP, for which the FWHM of the SL diffraction peaks is closely related to the optical quality and performance of MQW devices.[93,94]

Figure 12 (a) shows that as the temperature increases from 10 to 300 K, the integrated PL intensities decrease by a factor of 25, 6, and 5 for the In$_x$Ga$_{1-x}$N/GaN MQWs with In compositions of 8.8, 12.0, and 13.3%, respectively. The fact that the integrated PL intensity is greater for higher In composition throughout the 10 to 300 K temperature range is further evidence that the piezoelectric effect is not the main cause of the emission characteristics, because the piezoelectric effect would decrease the emission intensity more for higher In composition. The higher In content MQWs have higher intensity and are less sensitive to temperature change, because the higher In content

suppresses nonradiative recombination, as seen in the temperature-dependent carrier lifetimes measured by TRPL, as illustrated in Figure 12 (b). The effective lifetimes increase with temperature up to 50 K, indicating that radiative recombination dominates in these samples at low temperatures. Above 50 K, the effective lifetime decreases, since nonradiative processes predominantly influence the emission at higher temperatures. The lifetime drops steeply above 50 K for the 8.8% In sample. The lifetime for the 12.0% In sample starts out higher than that of the 13.3% In sample, but is below the lifetime of the 13.3% In sample above ~150 K. This indicates that although the higher In content creates defects with disadvantages, many of these defects also decrease thermally activated nonradiative recombination. By using Equations 2 and 3 from page 7, the 300 K nonradiative recombination lifetimes were determined to be 0.6, 2.7, and 3.6 ns for 8.8, 12.0, and 13.3% In, respectively, which shows that the higher In content suppresses nonradiative recombination.

The emission characteristics are improved with higher In content, because the higher In content causes more In composition fluctuation, and therefore, more carrier localization, which keeps carriers away from nonradiative pathways. The broadening of the PLE spectra and the increase in the Stokes shift, seen in Figure 11 (a), shows that there is carrier localization that is enhanced with increasing In.[6,7] Also, the incorporation of more In into the $In_xGa_{1-x}N$ well layer can reduce the density of nonradiative recombination centers.[89] Suppressing nonradiative recombination lowers the RT SE threshold, because only the radiative recombination contributes to gain. A lower RT SE threshold for samples with higher In composition shows that the suppression of nonradiative recombination overcomes the drawbacks of defects that increase with In

content, such as interface imperfections. This beneficial effect of higher In content

saturates with higher In composition, since there is not much difference in carrier

lifetimes, and therefore, SE threshold densities for the 12.0 and 13.3% In samples. This

makes developing laser diodes with longer emission wavelengths difficult.

As the In composition increases, the FWHM of SL diffraction peaks broadens due

to the spatial fluctuation of interfaces. However, higher In content suppresses

nonradiative recombination, thereby decreasing the RT SE threshold densities. Regions

of higher In content localize carriers and keep them away from nonradiative pathways,

and indium atoms may also reduce the density of nonradiative recombination centers.

Influence of Si doping in GaN barriers

Si doping is very important in the design of Group III-nitride MQW devices. The

influence of Si doping on the optical properties of GaN epilayers,[95,96] $In_xGa_{1-x}N/GaN$

QWs,[5,65,97-100] and $GaN/Al_xGa_{1-x}N$ QWs [101,102] has been widely studied. Not only does Si

doping screen or partially screen the internal electric field created by piezoelectric and

spontaneous polarizations, but Si doping dramatically changes the structural, and hence,

optical properties.

The effects of Si doping on the structural and optical properties (spontaneous and

stimulated emission) of InGaN/GaN MQW structures has been intensively

studied.[5,65,77,98] A series of InGaN/GaN MQW samples were grown on c-plane sapphire

substrates by MOCVD, to study the effects of Si doping in the GaN barriers. The

samples consisted of a 1.8 μm thick GaN buffer layer and a 12-period MQW with 3 nm

thick $In_{0.18}Ga_{0.82}N$ wells and 4.5 nm thick GaN barriers, followed by a 100 nm thick

$Al_{0.07}Ga_{0.93}N$ capping layer. The disilane doping precursor flux was systematically varied

from 0 to 4 nmol/min during GaN barrier growth to obtain Si doping in the GaN barriers ranging from $n < 1 \times 10^{17}$ (nominally undoped) to $n = 3 \times 10^{19}$ cm^{-3} for the different samples, as determined by secondary ion mass spectroscopy and Hall measurements.

Figure 13 shows 10 K PL (solid lines), PLE (dashed lines), and decay times plotted as a function of emission energy (open circles) for the main InGaN PL peak. The near-band-edge emission from the GaN barriers and the AlGaN cladding layer are also clearly seen at 3.48 and 3.60 eV, respectively. A large Stokes shift of the InGaN PL emission with respect to the band edge measured by PLE is clearly seen. As the Si doping concentration increases, the Stokes shift decreases. The Stokes shift for the sample with $n = 3 \times 10^{19}$ cm^{-3} is ~120 meV smaller than that of the nominally undoped sample. The 10 K decay time measured by TRPL increases with decreasing emission energy, so the emission peak energy redshifts as time proceeds after an excitation pulse. This behavior is characteristic of localized states, which in this case, are most likely due to alloy fluctuations and/or interface irregularities. The decrease seen in decay time with increasing Si doping, from ~30 ns (for $n < 1 \times 10^{17}$ cm^{-3}) to ~4 ns (for $n = 3 \times 10^{19}$ cm^{-3}), can be explained by a decrease in the potential fluctuations, which would cause carrier localization. With less carrier localization, the charge carriers are more likely to diffuse to nonradiative recombination centers.

However, the decrease in the 10 K decay time with increasing Si doping can also be explained by a decrease in sample quality, which would also cause more nonradiative recombination. To resolve this issue, the temperature dependence of the decay time was measured, as shown in Figure 14. This figure shows the decay time at the emission peak energy and at the low and high energy sides of the emission peak, but we will focus on

the decay time of the higher energy side, for reasons that will become apparent. For the nominally undoped sample with $n < 1 \times 10^{17}$ cm^{-3} (open symbols), the higher energy decay time at first increases with temperature, up to about 40 ns at 70 K, in qualitative agreement with the temperature dependence of radiative recombination. As the temperature is further increased, the lifetime decreases because nonradiative processes become predominant. Further evidence of this is given by the fact that the lifetimes become independent of emission energy at higher temperatures. The crossover temperature, T_c, at the peak decay time is determined by the radiative and nonradiative recombination rates. A decrease in the radiative lifetime would increase T_c, and a decrease in the nonradiative lifetime would decrease T_c. Note that T_c gradually increases as n increases: $T_c \sim 70$ K for $n < 1 \times 10^{17}$ cm^{-3}, $T_c \sim 100$ K for $n = 2 \times 10^{18}$ cm^{-3} (not shown here), and $T_c \sim 120$ K for $n = 3 \times 10^{19}$ cm^{-3}. This indicates that the decrease in lifetime with increasing n is due to a decrease in the radiative recombination lifetime rather than a decrease in the nonradiative recombination lifetime. Of course, one might suspect that T_c increasing with n may be due to an increase in the nonradiative lifetime with n. However, this cannot be true since an increase in the nonradiative lifetime would increase the effective decay time, but the effective decay time decreased with increasing n. Most radiative recombination tends to occur at the lowest energy levels, where the carriers are most restricted. With shallower potential minima, the carriers would be restricted more at higher energies, and this would cause a smaller radiative lifetime at higher emission energies. Therefore, the decrease in lifetime with increasing n is mainly due to a decrease in potential localization.

The degree of potential localization can be affected by the interface quality. To investigate the effect of Si doping on the GaN surface morphology, three reference 7 nm thick GaN epilayers were also grown at 800 °C with different disilane flux rates of 0, 0.2, and 2 nmol/min during growth.[97,98] The surface morphology of these reference samples was examined by atomic force microscopy (AFM) in the tapping mode. Figure 15 shows 2 μm × 2 μm AFM images of the three reference GaN epilayers. The root-mean-square surface roughness estimated from the AFM images was 0.49, 0.42, and 0.22 nm for GaN epilayers with disilane flow rates of (a) 0, (b) 0.2, and (c) 2 nmol/min during growth, respectively. Thus, smoother GaN surfaces with a more homogeneous terrace length were achieved at higher Si doping levels.

High-resolution XRD measurements also showed that Si doping of the GaN barriers improved the interface properties of the InGaN/GaN MQWs,[77] in good correlation with the optical properties. Figure 16 shows (0002) reflection high-resolution XRD $\omega - 2\theta$ scans measured from the 12-period InGaN/GaN MQW structures with different Si doping concentrations ranging from $n < 1 \times 10^{17}$ to $n = 3 \times 10^{19}$ cm^{-3} in the GaN barriers. The strongest peak is due to the GaN buffer layer, and the high-angle shoulder of the GaN peak is due to the AlGaN capping layer. All the spectra clearly show higher-order SL diffraction peaks indicating good layer periodicity. The SL period was determined from the positions of the SL satellite peaks. The SL peaks of the nominally undoped sample ($n < 1 \times 10^{17}$ cm^{-3}) have an asymmetrically broadened lineshape, but the SL peaks of the Si doped MQWs have a more symmetric lineshape. The broadening is partially due to spatial variation of the SL period, which can be caused by intermixing and/or interface roughness. The inset of Figure 16 shows the FWHM of

42

the higher-order SL satellite peaks as a function of Si doping level. As n increases, the FWHM of the higher-order SL satellite peaks narrows: the FWHM of the second order SL peaks was observed to be 589, 335, and 234 arcsec for $n < 1 \times 10^{17}$, $n = 2 \times 10^{18}$, and $n = 3 \times 10^{19}$ cm^{-3}, respectively. The ratio of integrated intensity between SL peaks is almost the same for all three samples, as expected for nominally identical SL structures, which differ only in their degree of structural perfection. In addition, symmetric and asymmetric reciprocal space mapping scans were similar for the different samples, regardless of the Si doping concentration. Therefore, Si doping in the GaN barriers significantly improved the structural and interface quality of the InGaN/GaN MQWs. Since Si atoms can change the quality and/or surface free energy of the GaN barriers, it may affect the growth condition (or mode) of the subsequent InGaN wells and interfaces.[95,103,104] The decrease in the Stokes shift and the decrease in radiative recombination lifetime with increasing Si doping in the GaN barriers were due to a decrease in potential fluctuations and an improvement in the interfacial structural qualities. Although Si doping of the GaN barriers did not change the overall strain state (reciprocal space mapping of high-resolution XRD revealed there was no relaxation of the lattice-mismatch strain with the 1.8 μm thick GaN base layer), it significantly affected the structural and interface quality of the InGaN/GaN MQWs.

Moreover, Bidnyk *et al.* reported the effect of Si doping on the emission efficiency and SE threshold pump density of the InGaN/GaN MQWs with different levels of Si doping in the GaN barriers.[65] All the samples showed a strong blueshift of the spontaneous emission with increasing excitation density, mainly due to band filling of the energy tail states. The blueshift stopped just before the start of SE. The SE spectrum of

the MQW with $n = 2 \times 10^{18}$ cm^{-3} consisted of many narrow peaks of ~1 Å FWHM, and there was no noticeable broadening of the SE peaks as the temperature was increased from 175 to 575 K. It is important to note that only moderately Si doped MQWs had enhanced luminescence efficiency and a reduction of the SE threshold. The maximum emission intensity and the lowest SE threshold (55 kW/cm^2) were achieved for the sample with $n = 2 \times 10^{18}$ cm^{-3}, while a SE threshold of 165 kW/cm^2 was obtained for the sample with $n = 3 \times 10^{19}$ cm^{-3}. This fact, together with results presented above, shows that although Si doping improves the interface properties, it does not necessarily enhance the SE properties. Therefore, carrier localization at potential fluctuations caused by interface irregularities is very important for improving the emission properties. Similar effects were found for Si doping in InGaN barriers of In$_x$Ga$_{1-x}$N/In$_y$Ga$_{1-y}$N QW structures.[100,105] In subsequent chapters, we will see more evidence that recombination of localized carriers is the predominant emission mechanism in InGaN/GaN MQW structures of state-of-art laser diodes.
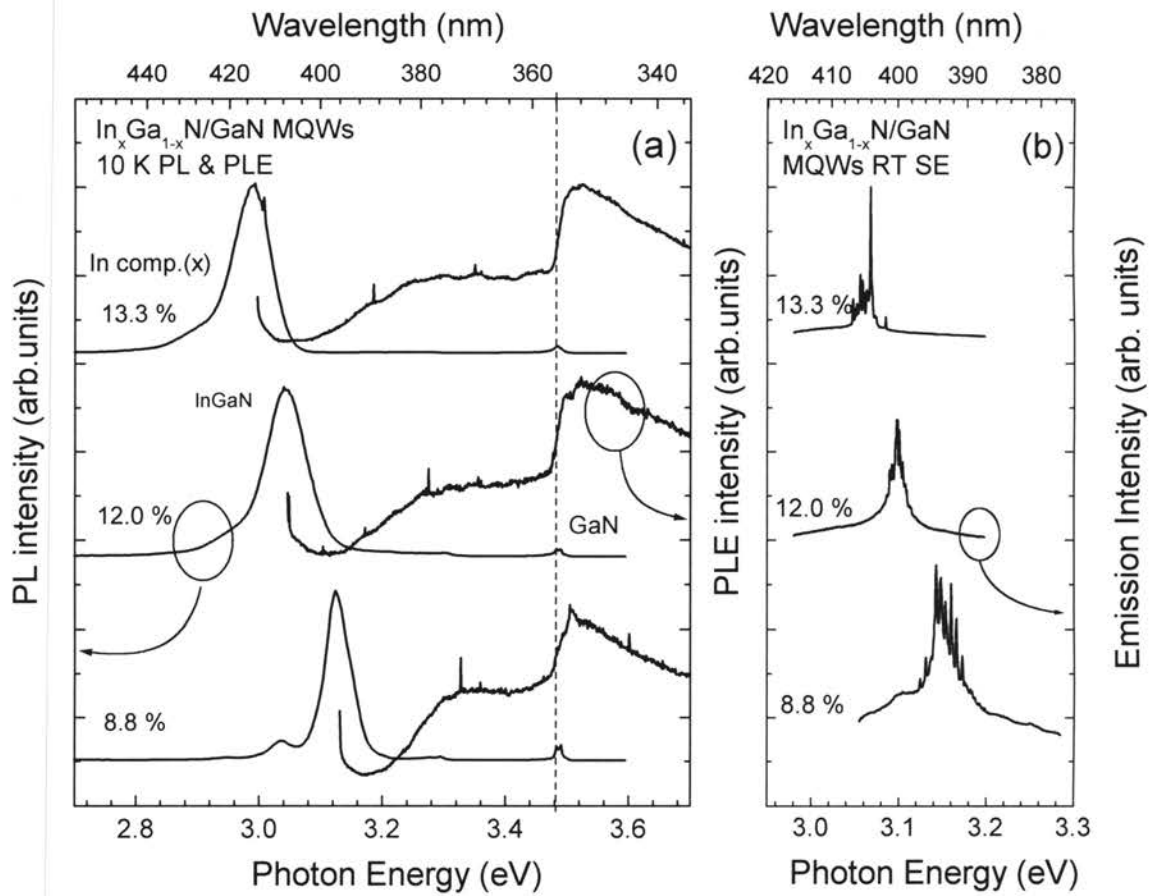
Figure 11. (a) 10 K PL and PLE, and (b) RT SE spectra of 5-period $In_xGa_{1-x}N$/GaN MQWs with different In compositions of 8.8, 12.0, and 13.3 %.
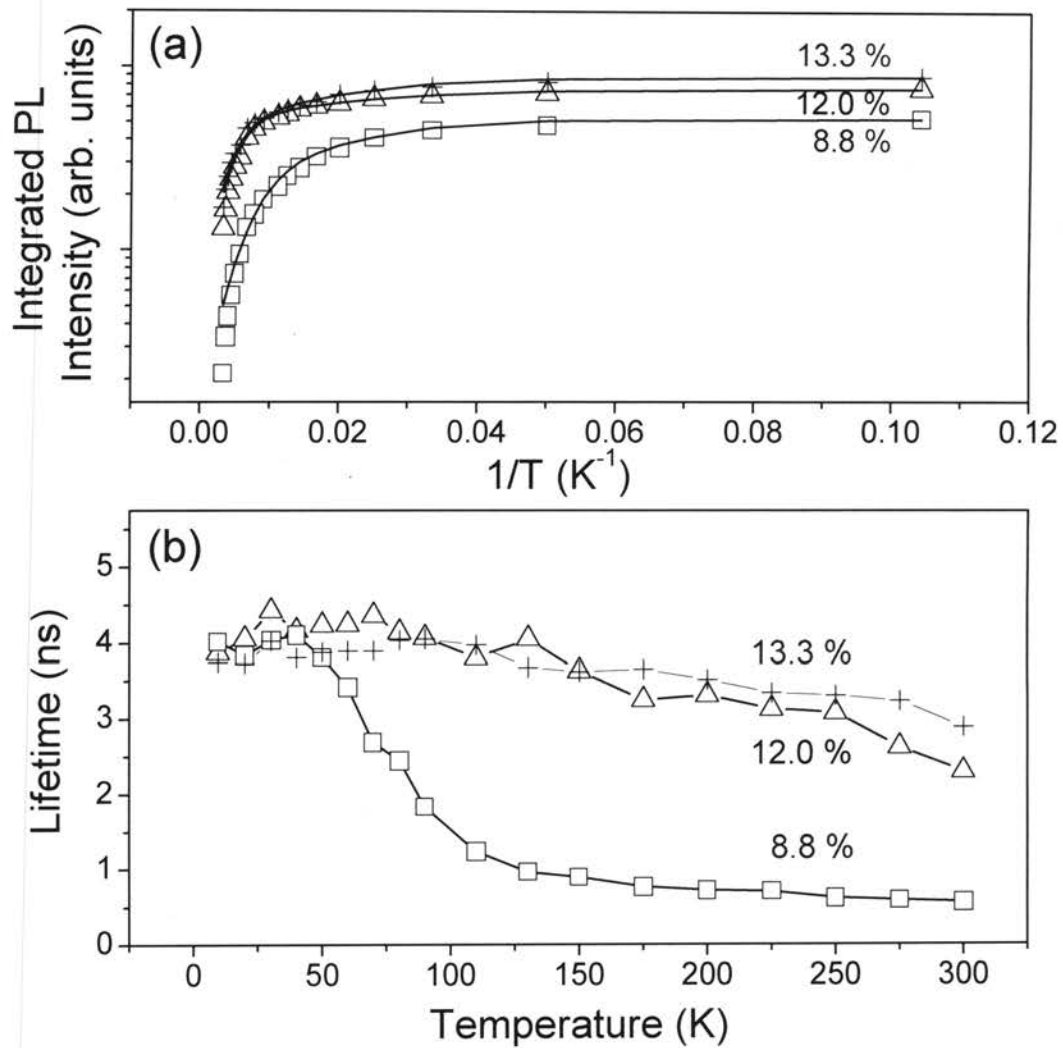
Figure 12. (a) Integrated PL intensity as a function of $1/T$ and (b) carrier lifetime as a function of T for InGaN emission of $In_xGa_{1-x}N$/GaN MQWs with x = 8.8, 12.0, and 13.3%.
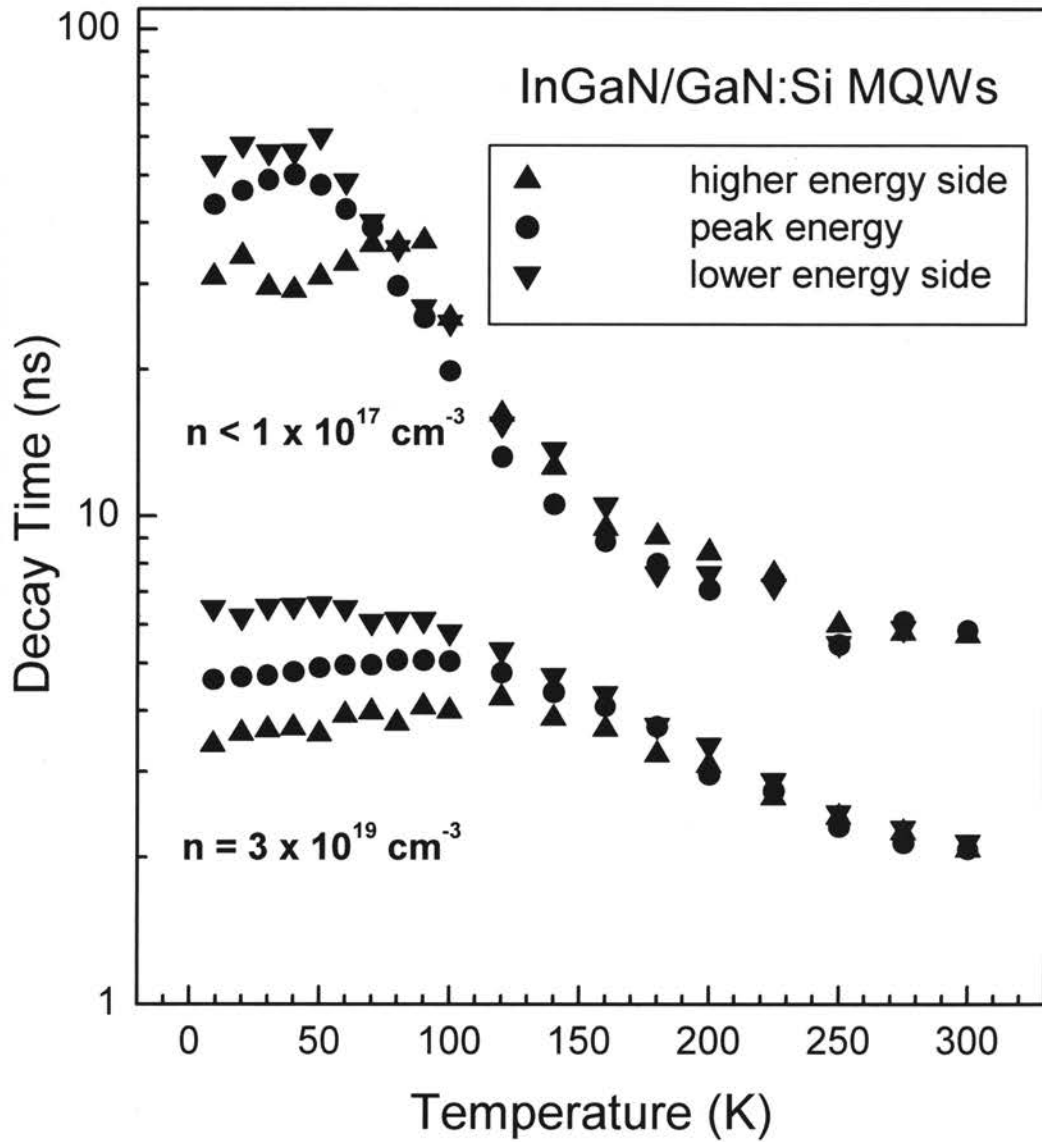
Figure 14. Temperature dependence of decay times monitored above (up triangles), below (down triangles), and at (circles) the emission peak energy for $In_{0.18}Ga_{0.82}N/GaN$ MQWs with $n < 1 \times 10^{17}$ cm^{-3} and $n = 3 \times 10^{19}$ cm^{-3} in the GaN barriers. The characteristic crossover temperature, T_c, (which is determined by the radiative and nonradiative recombination rates) gradually increases as n increases: $T_c \sim 70$ K for $n < 1 \times 10^{17}$ cm^{-3}, $T_c \sim 100$ K for $n = 2 \times 10^{18}$ cm^{-3} (not shown), and $T_c \sim 140$ K for $n = 3 \times 10^{19}$ cm^{-3}.
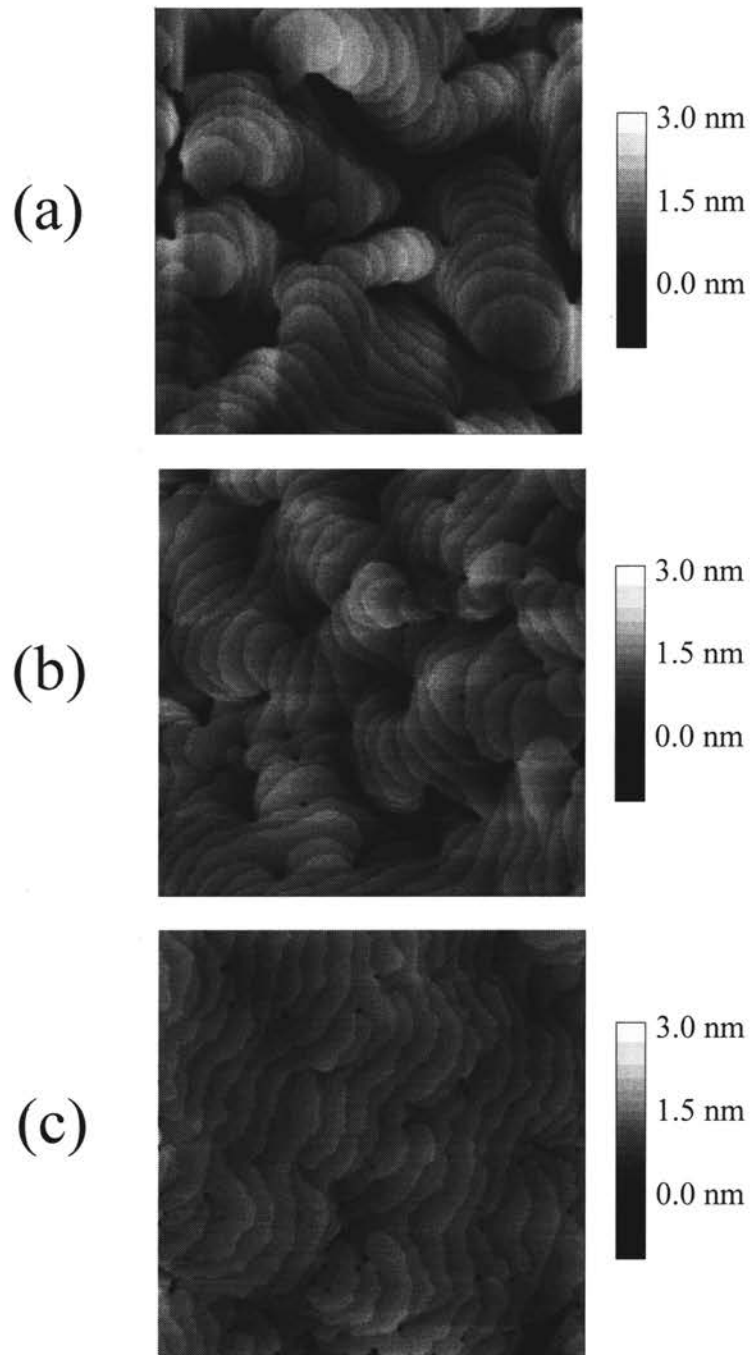
Figure 15. 2 μm × 2 μm AFM images of three 7-nm-thick GaN films with different disilane flow rates during growth. The root-mean-square surface roughness estimated from the AFM images is 0.49, 0.42, and 0.22 nm for the GaN epilayers with the disilane flow rates of (a) 0, (b) 0.2, and (c) 2 nmol/min, respectively. A higher quality GaN surface morphology and a larger average terrace length were achieved by increasing Si incorporation.
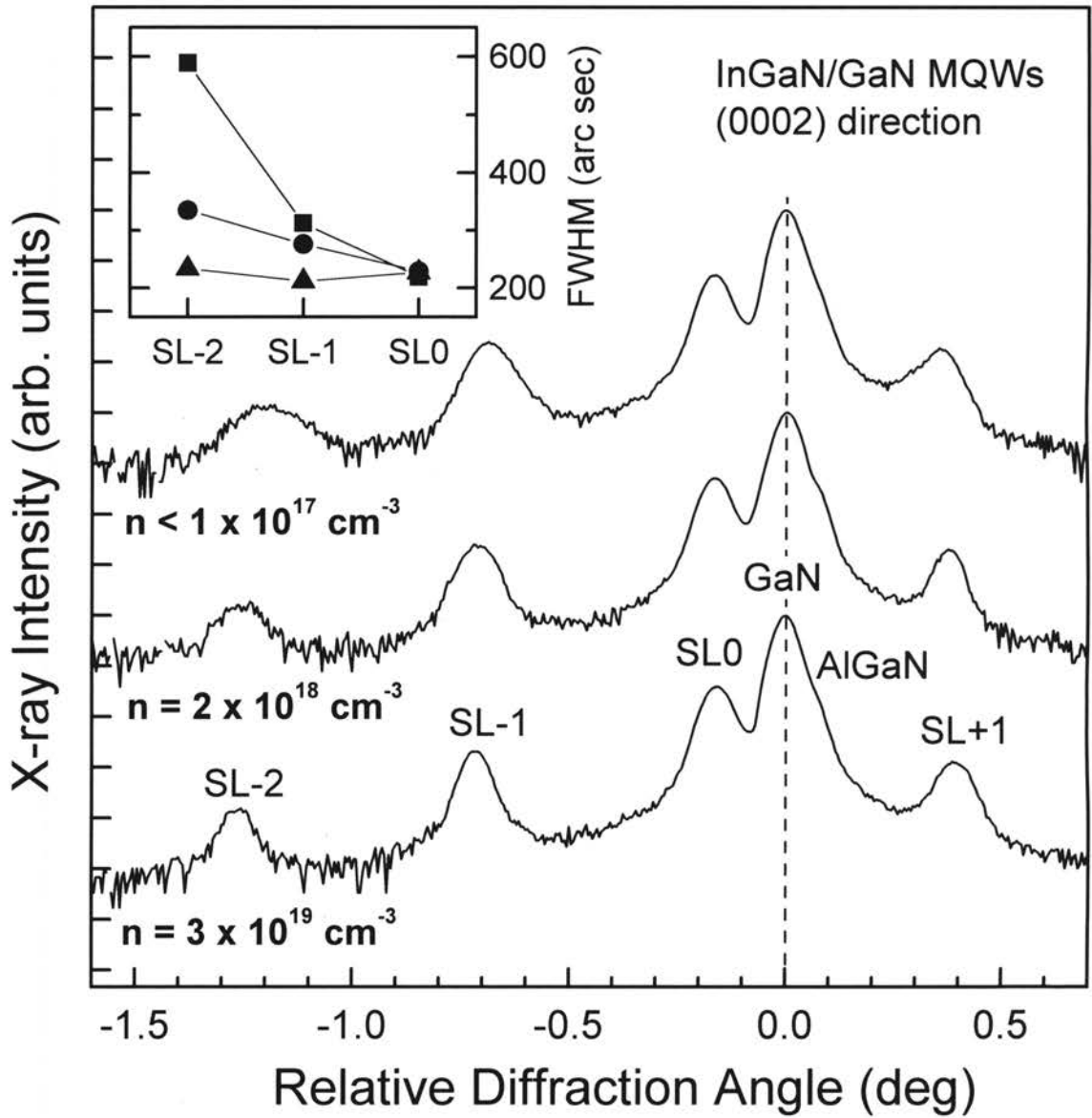
Figure 16. (0002) reflection high-resolution XRD curves of 12-period In$_{0.18}$Ga$_{0.82}$N/GaN MQWs having different Si doping levels in the GaN barrier layers. The variation in the FWHM of the higher-order SL satellite peaks is shown in the inset as a function of the Si doping level (squares: $< 1 \times 10^{17}$ cm^{-3}; circles: 2×10^{18} cm^{-3}; triangles: 3×10^{19} cm^{-3}).

CHAPTER V

OPTICAL TRANSITIONS AT VARIOUS TEMEPRATURES AND EXCITATION CONDITIONS

This chapter discusses optical phenomena associated with strong carrier localization in InGaN-based heterostructures. The localized band tail states are proven through their emission spectra dependence on temperature, excitation energy, and excitation density. These studies give insight into the recombination mechanisms responsible for the spontaneous and stimulated emission, which is important for both physical and practical aspects. This chapter is divided into two sections. The first section examines the temperature dependence of PL spectra, integrated PL intensity, PL temporal evolution, and optically pumped SE spectra of InGaN structures. The second section discusses energy selective spontaneous and stimulated emission studies of the InGaN-based structures. The spontaneous and stimulated emission spectra were observed with excitation photon energies over a wide spectral range above the emission peak position to provide evidence of localized band tail states for both spontaneous and stimulated emission. The excitation density and length dependences of the stimulated emission are also investigated.

Anomalous Temperature Dependence of InGaN Emission

The temperature dependence of the fundamental energy gap is mainly caused by band structure changes induced by lattice thermal expansion and electron-phonon interactions. The temperature-induced change of the energy bandgap E_g is generally given by the empirical Varshni equation:[106]

$$E_g(T) = E_g(0) - \frac{aT^2}{(b+T)},$$ (14)

where $E_g(T)$ is the bandgap energy at temperature T, and a and b are the Varshni thermal coefficients. Previously, the parameters $a = 8.32 \times 10^{-4}$ eV/K (1×10^{-5} eV/K) and $b = 835.6$ K (1196 K) for the GaN $\Gamma_9^v - \Gamma_7^c$ (In$_{0.14}$Ga$_{0.86}$N) transition were determined from photoreflectance studies.[107,108] Figure 17 shows the typical temperature dependence of the free exciton (FX) and the bound exciton (BX) emissions from a MOCVD-grown GaN epilayer. The temperature-dependent PL peak shift of the GaN epilayer was consistent with the estimated energy decrease of about 70 meV between 10 and 300 K. The energy difference between the BX and the FX energies is about 6 meV, which corresponds to the BX-to-FX transition temperature of ~70 K.

However, the PL emission from InGaN-based structures does not follow the typical temperature dependence seen in GaN. Several groups observed an anomalous temperature-induced blueshift in InGaN QW structures and attributed this to band tail states caused by potential fluctuations.[109-111] We will prove this through the correlation between the temperature-induced anomalous emission behavior and its carrier dynamics

for both InGaN epilayers and InGaN/GaN MQWs.[111,112] A similar deviation from the typical temperature-induced energy gap shrinkage was seen in ordered (Al)GaInP [113,114] and disordered (Ga)AlAs/GaAs superlattices.[115,116]

Figure 18 shows the temperature dependence of the InGaN PL spectra for (a) an $In_{0.18}Ga_{0.82}N/GaN$ MQW and (b) an $In_{0.18}Ga_{0.82}N$ epilayer over a temperature range of 10 to 300 K. As the temperature increases from 10 K to T_I, where T_I is 70 (50) K for the MQW (epilayer), the peak energy position E_{PL} redshifts 19 (10) meV. This value is about five times as large as the expected bandgap shrinkage of ~4 (2) meV for the MQW (epilayer) over this temperature range.[108] As the temperature is further increased, E_{PL} blueshifts 14 (22.5) meV from T_I to T_{II}, where T_{II} is 150 (110) K for the MQW (epilayer). By considering the estimated temperature-induced bandgap shrinkage of ~13 (7) meV for the MQW (epilayer), the actual blueshift of the PL peak with respect to the band edge is about 27 (29.5) meV over this temperature range. When the temperature is further increased above T_{II}, the peak positions redshift again. From the observed PL peak redshift of 16 (45) meV and the expected bandgap shrinkage of ~43 (51) meV from T_{II} to 300 K for the MQW (epilayer), an actual blueshift of about 27 (6) meV occurs relative to the band edge over this temperature range.

Figure 19 shows an Arrhenius plot of the normalized integrated PL intensity of the InGaN emission of the $In_{0.18}Ga_{0.82}N/GaN$ MQW. The total luminescence intensity from this sample is reduced by only one order of magnitude from 10 to 300 K, indicating a high PL efficiency even at room temperature. (For the MOCVD-grown GaN epilayer seen in Figure 17, the change in integrated PL intensity from 10 to 300 K is 2 – 3 orders of magnitude.) For $T > 70$ K, the integrated PL intensity of the InGaN luminescence has

a thermal activation energy of about 35 meV. In general, the quenching of the luminescence with temperature can be explained by thermal emission of carriers out of confining potentials with a depth about equal to the activation energy. Since the observed activation energy is much less than the conduction and valence band offsets, as well as the bandgap difference between the wells and barriers, the thermal quenching of the InGaN emission is *not* due to thermal activation of electrons and/or holes from the InGaN wells into the GaN barriers. Instead, the dominant mechanism for the quenching of the InGaN PL is thermally activated emission of photogenerated carriers out of the potential minima caused by potential variations, such as alloy and interface fluctuations.

We also studied the carrier dynamics of the InGaN luminescence by TRPL over the 10 to 300 K temperature range. Figure 20 shows the PL peak energy E_{PL}, the relative energy difference (ΔE) between E_{PL} and E_g, and the effective decay time (τ_{eff}) at the emission peak energy, at the lower energy side of the peak, and higher energy side of the peak, as a function of temperature for the $In_{0.18}Ga_{0.82}N$/GaN MQW and the $In_{0.18}Ga_{0.82}N$ epilayer. The temperature dependence of ΔE and E_{PL} are seen to be strongly correlated with the change in τ_{eff}. For both the MQW and the epilayer, an overall increase of τ_{eff} is observed with increasing temperature for $T < T_l$, in qualitative agreement with the temperature dependence of radiative recombination.[85,86] As seen in the previous chapter, in this temperature range, τ_{eff} becomes longer with decreasing emission energy, and hence, the peak energy of the emission shifts to the low energy side as time proceeds. This behavior is characteristic of carrier localization, most likely due to alloy fluctuations (and/or interface roughness in MQWs). As the temperature is further

increased beyond T_I, the lifetime of the MQW (epilayer) quickly decreases to less than

10 (0.1) ns and remains almost constant between T_{II} and 300 K, indicating the

predominance of nonradiative processes predominantly at higher temperatures. This is

further evidenced by the fact that the difference between the lifetimes monitored above,

below, and at the peak energy disappears for $T > T_I$. This characteristic temperature T_I

also marks the change from redshift to blueshift for ΔE and E_{PL} with increasing

temperature. Moreover, in the temperature range from T_I to T_{II}, where a blueshift of

E_{PL} is occurs, τ_{eff} dramatically decreases from 35 to 8 (0.4 to 0.05) ns for the MQW

(epilayer). Above T_{II}, where a redshift of E_{PL} occurs, τ_{eff} changes little for both the

MQW and the epilayer.

The InGaN recombination mechanism for different temperature ranges can be

explained in terms of the carrier dynamics, as follows: (i) For $T < T_I$, radiative

recombination is dominant, so the carrier lifetime increases with temperature, giving the

carriers more time to nonradiatively relax to lower energy tail states of the

inhomogeneous potential fluctuations before radiatively recombining. This reduces the

average emission photon energy, especially reduces the intensity of the higher energy

side of the emission peak, and produces a redshift in the peak energy position with

increasing temperature. (ii) For $T_I < T < T_{II}$, the dissociation rate increases with

temperature and other nonradiative processes become dominant, so the carrier lifetimes

decrease greatly and also become independent of emission energy. Due to the decreasing

lifetime, the carriers recombine before reaching the lower energy tail states. This

broadens the higher energy side of the emission peak and causes a blueshift of the peak

55

energy. (iii) For $T > T_{II}$, since nonradiative recombination processes are dominant and the lifetimes decrease slowly and almost remain constant with increasing temperature, the photogenerated carriers are less affected by the change in carrier lifetime, so the blueshift behavior becomes smaller. Note that the slope of ΔE is very sensitive to changes in τ_{eff} with temperature for both the InGaN/GaN MQW and the InGaN epilayer. Since the blueshift is smaller than the temperature-induced bandgap shrinkage for $T > T_{II}$, the peak has an overall redshift. Therefore, the change in carrier recombination mechanism with increasing temperature causes the S-shaped redshift-blueshift-redshift behavior of the peak energy of the InGaN luminescence, and this anomalous temperature dependence of the emission is due to nonradiative transitions between localized to extended energy tail states in the InGaN-based structures.

An interesting difference between the InGaN/GaN MQW and the InGaN epilayer is the greater effective blueshifting of the MQW, even near RT, probably due to a greater degree of carrier localization in the MQW. Except for this, a similar temperature-induced S-shaped emission behavior was observed for both the InGaN/GaN MQW and the InGaN epilayer, even though τ_{eff} of the MQW is about two orders of magnitudes longer than that of the epilayer. This indicates that the anomalous temperature-induced emission shift depends mainly on the change in carrier recombination dynamics rather than the absolute value of τ_{eff}.
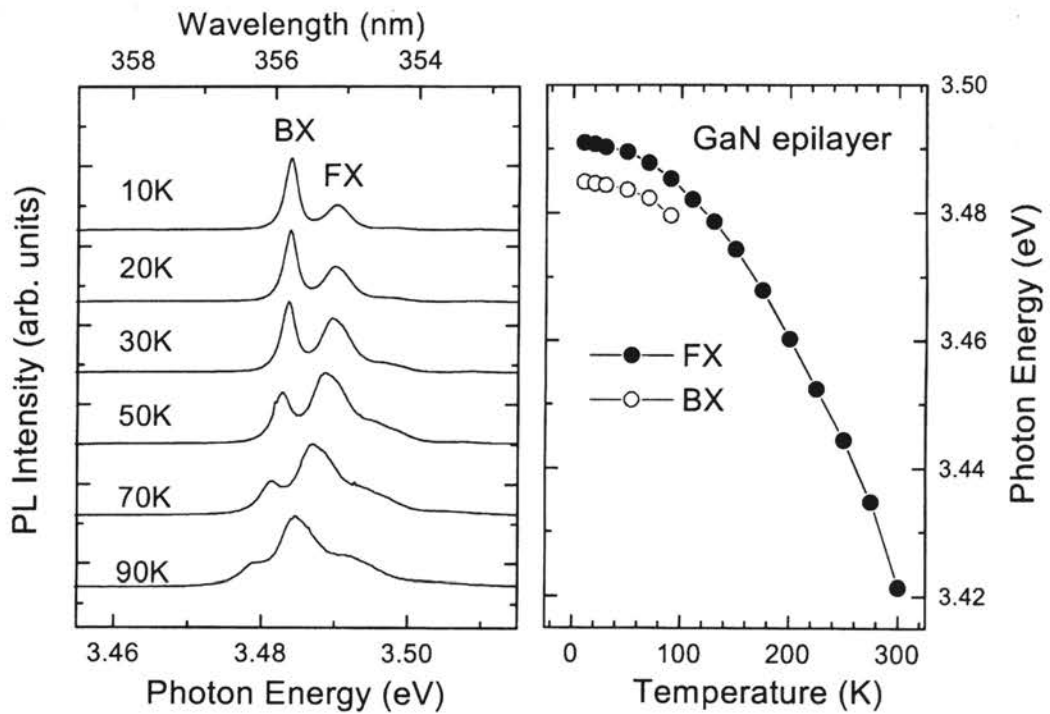
Figure 17. Typical temperature dependence of near-band-edge free exciton (FX) and bound exciton (BX) luminescence spectra and peak positions taken from a MOCVD-grown GaN epilayer. The energy difference between the BX and the FX energies is about 6 meV, which corresponds to the BX-to-FX transition temperature of ~70 K.
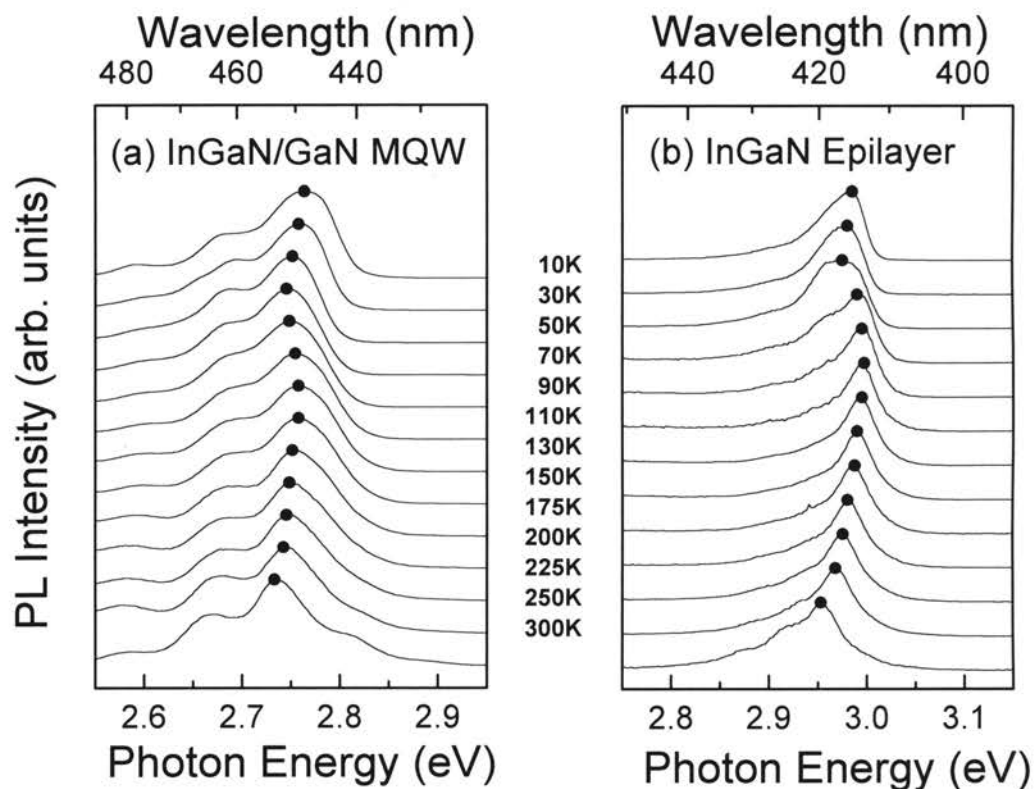
Figure 18. Typical InGaN-related PL spectra for (a) an $In_{0.18}Ga_{0.82}N$/GaN MQW and (b) an $In_{0.18}Ga_{0.82}N$ epilayer in the temperature range from 10 to 300 K. The main emission peak of both samples shows an S-shaped shift with increasing temperature (solid circles). All spectra are normalized and shifted in the vertical direction for clarity. Note that the turning temperature from redshift to blueshift is about 70 and 50 K for the $In_{0.18}Ga_{0.82}N$/GaN MQW and the $In_{0.18}Ga_{0.82}N$ epilayer, respectively.
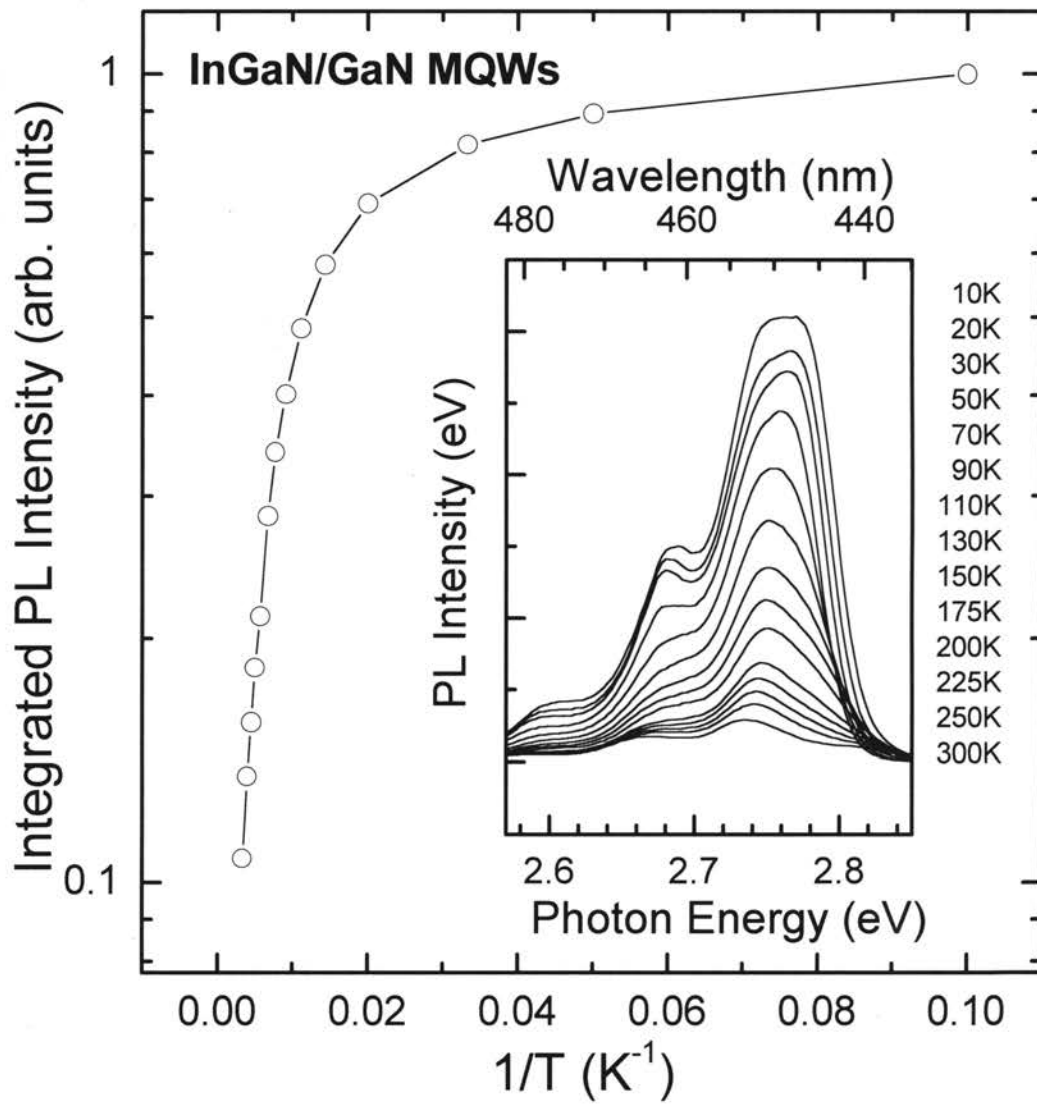
Figure 19. Normalized integrated PL intensity as a function of $1/T$ for the InGaN emission in the In$_{0.18}$Ga$_{0.82}$N/GaN MQWs (open circles). The inset shows InGaN PL spectra for the temperature range of 10 to 300 K. An activation energy of ~35 meV is obtained from the Arrhenius plot.

59
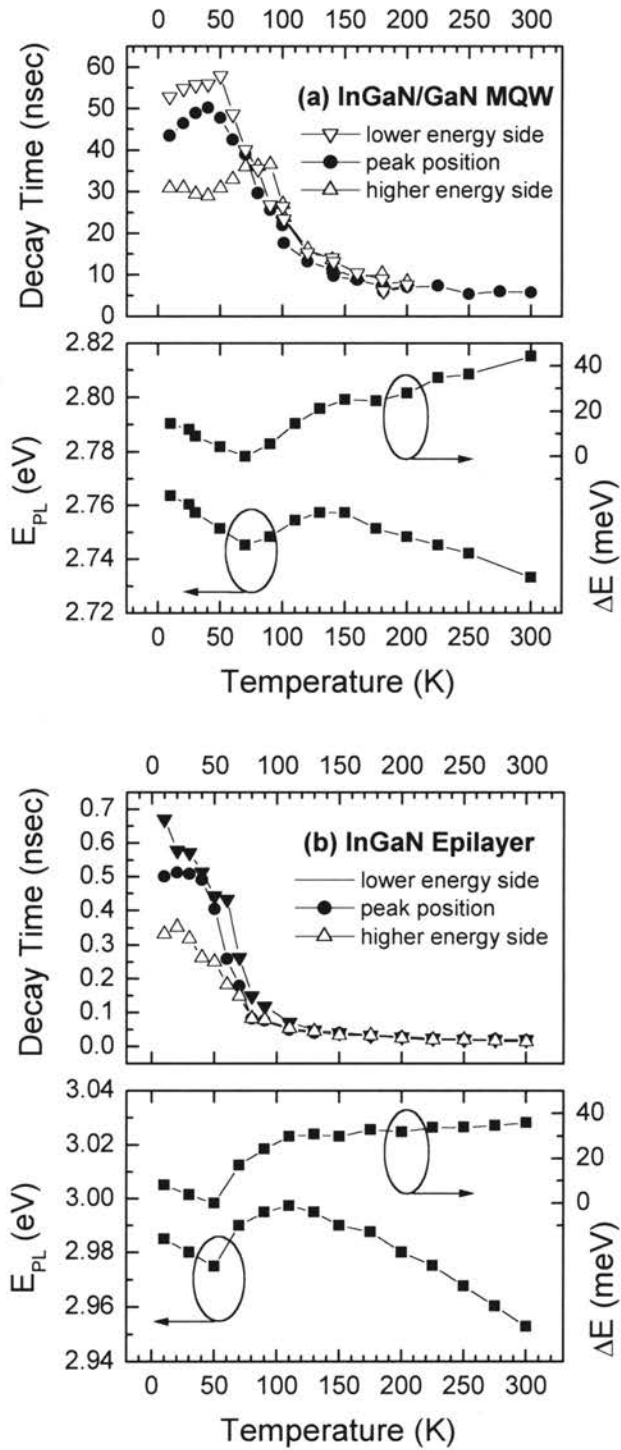
Figure 20. InGaN PL peak position E_{PL} and decay time as a function of temperature for (a) an $In_{0.18}Ga_{0.82}N$/GaN MQW and (b) an $In_{0.18}Ga_{0.82}N$ epilayer. ΔE is the relative energy difference between E_{PL} and E_g. The minimum value of ΔE is set at zero for simplicity.

Temperature Dependence of Optically Pumped Stimulated Emission

Optical pumping is widely used for studying stimulated emission and lasing in semiconductors, since it can generate the high carrier densities necessary for stimulated emission without electrical contacts so that complicated doping and device processing procedures are not required. We investigated the stimulated recombination process in the InGaN/GaN quantum wells by measuring the temperature dependence of the SE spectral shape, the integrated SE intensity, and the SE threshold density I_{th}.[65] We obtained optically pumped SE from InGaN/GaN MQWs in the side-pumping geometry with edge emission collected into a 1-m spectrometer and recorded by an optical multichannel analyzer or a UV-enhanced gated charge-coupled device (CCD). The pumping source was the third harmonic (355 nm) of an injection-seeded Nd:YAG laser with a pulse width of 6 ns and a repetition rate of 30 Hz. A cylindrical lens focused the pump laser onto the samples with the excitation spot in the form of a line.[92] The laser light intensity could be attenuated continuously using a variable neutral density filter.

Figure 21 shows the SE spectra at 200 K, 300 K, and 450 K for an $In_{0.18}Ga_{0.82}N$/GaN MQW with barrier Si doping of $n = 2 \times 10^{18}$ cm^{-3}. The SE peak is a statistical distribution of many narrow (< 1 Å FWHM) emission lines. These narrow emission lines had no noticeable broadening as the temperature was tuned from 10 K to 575 K. The dotted lines are the broad spontaneous emission spectra measured at pump densities about half that of the SE threshold for each temperature. As the excitation power density is raised above the SE threshold, a considerable spectral narrowing occurs (solid lines in Figure 21). The main effect of the temperature change from 200 K to 450 K was a shift of the spontaneous and stimulated emission peaks toward lower energy.

Increasing the temperature of the MQWs decreases their PL intensity because of optical losses that decrease the quantum efficiency. At high temperatures, only a small fraction of the photogenerated charge carriers reach conduction-band minima, and most of them recombine nonradiatively. Therefore, increasing the temperature causes a reduction of the modal gain and an increase in the SE threshold. To evaluate the relative number of carriers that recombine radiatively, the integrated emission intensity was measured as a function of excitation density for different temperatures, as shown in Figure 22. For the 200 – 550 K temperature range studied, under low excitation densities, the integrated intensity from the InGaN/GaN MQW increases almost linearly with pump density I_p (i.e., $\propto I_p^\alpha$, where $\alpha = 0.8 - 1.3$ on a log-log plot), but at high excitation densities, this dependence becomes superlinear (i.e., $\propto I_p^\beta$, where β is between 2.2 and 3.0). The excitation pump density at which the slope of the integrated intensity changes is the SE threshold density I_{th}. The slopes of the integrated intensity below and above the SE threshold do not significantly change from 200 to 550 K, and this indicates that the InGaN/GaN MQW SE mechanism is the same at RT and hundreds of degrees above RT.

The temperature dependence of the InGaN/GaN MQW SE threshold is shown in Figure 23 (solid dots). SE was observed throughout the entire temperature range studied, from 175 to 575 K. The SE threshold was ~25 kW/cm^2 at 175 K, ~55 kW/cm^2 at 300 K, and ~300 kW/cm^2 at 575 K, and roughly followed an exponential dependence. Such a low SE threshold indicates that the SE is due to the localization of carriers. The solid line in Figure 23 is a least-squares fit to the empirical form, $I_{th}(T) = I_o \exp(T/T_o)$, for the temperature dependence of I_{th}. The characteristic temperature, T_o, is about 162 K in the

62

temperature range of 175 – 575 K for this MQW. This characteristic temperature is much larger than the near RT values of laser structures based on other III-V [117,118] and II-VI [119,120] materials, where small values of T_o are a strong limiting factor for high-temperature laser operation. Such a low sensitivity of I_{th} to temperature change in InGaN/GaN MQWs opens up enormous opportunities for their high-temperature applications. Laser diodes with InGaN/GaN lasing mediums can potentially operate at a few hundred degrees Kelvin above RT.
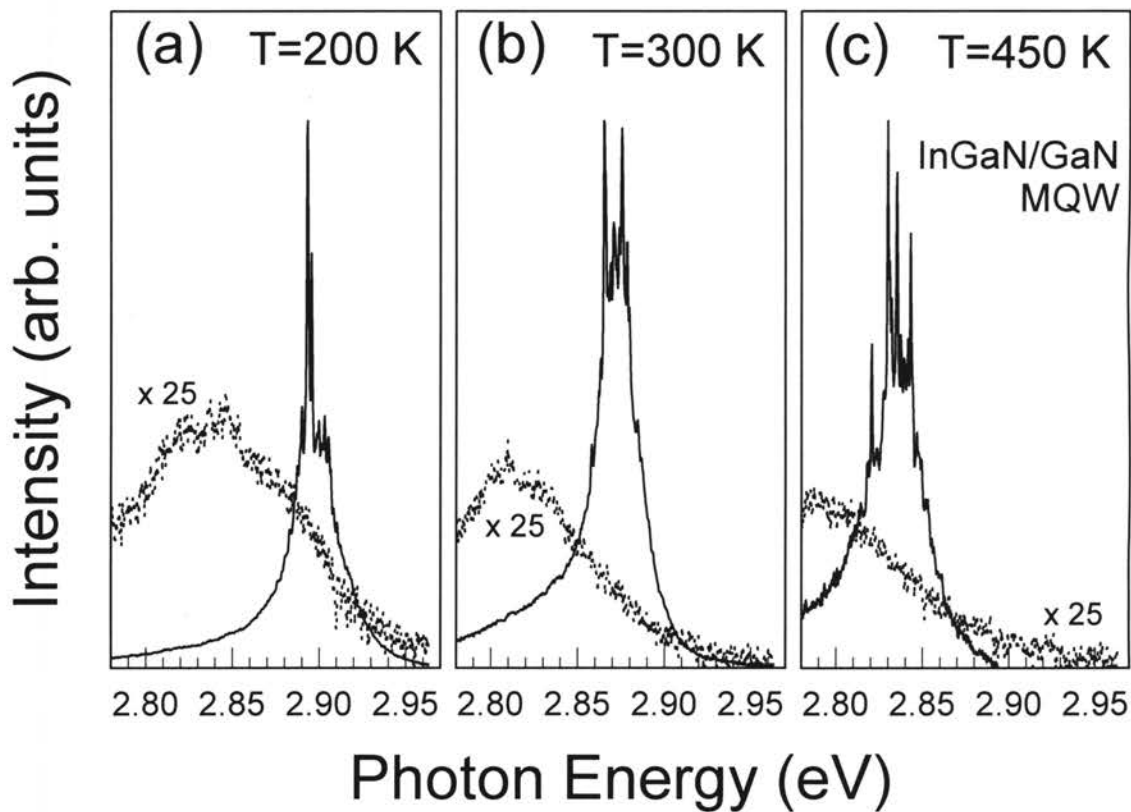
Figure 21. SE spectra (solid lines) of an $In_{0.18}Ga_{0.82}N$/GaN MQW with barrier Si doping of $n = 2 \times 10^{18}$ cm^{-3} at (a) 200 K, (b) 300 K, and (c) 450 K, illustrating that the SE peak is composed of a multitude of narrow (< 0.1 nm) peaks that do not noticeably broaden with increasing temperature. These SE spectra were collected for excitation densities of twice the SE threshold for the respective temperatures. The spontaneous emission spectra (dotted lines) are also shown for excitation densities half that of the SE threshold at each temperature. The SE spectra are normalized for clarity.
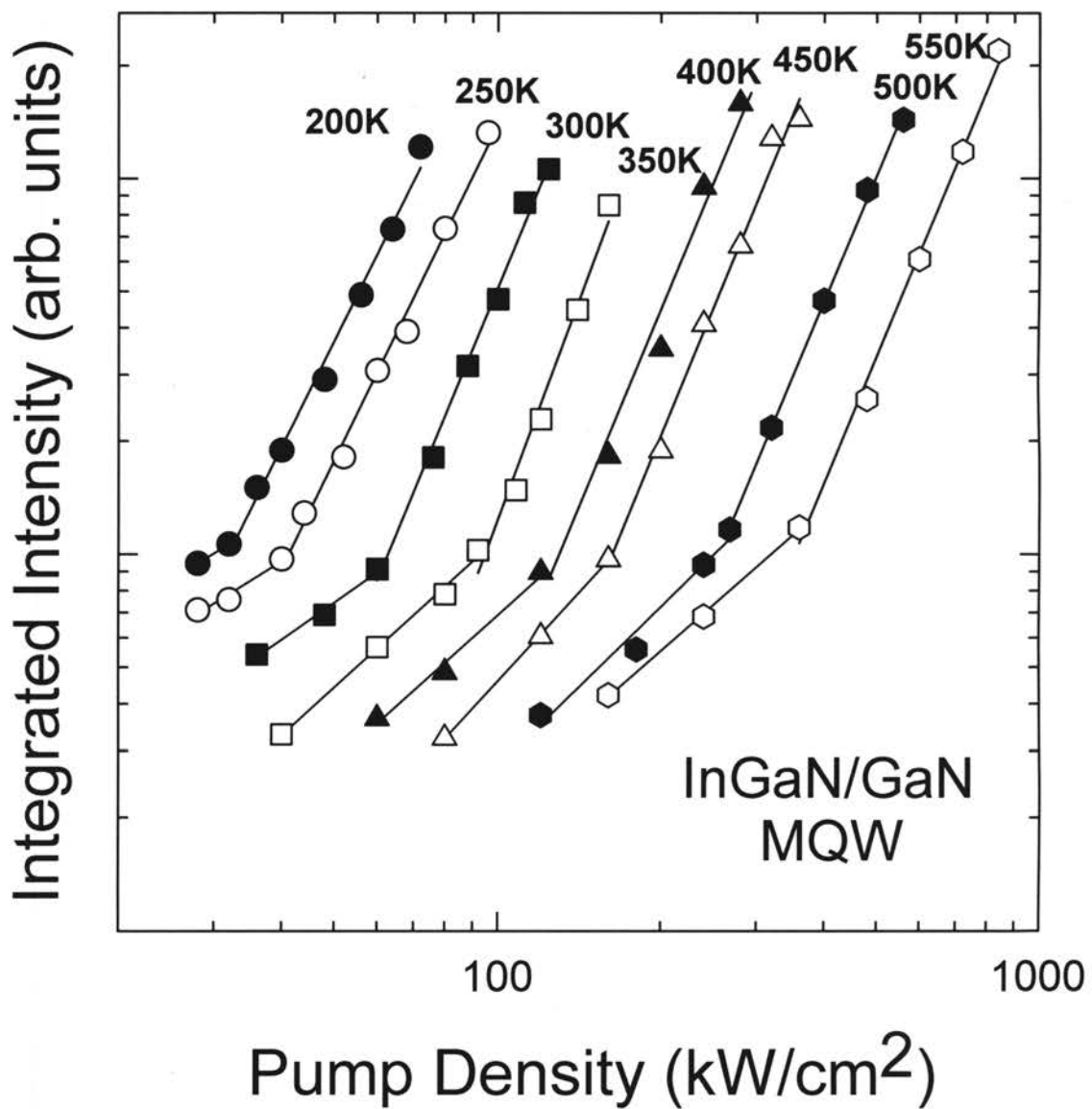
Figure 22. Integrated intensity of $In_{0.18}Ga_{0.82}N$ /GaN MQW emission as a function of optical excitation density for different temperatures. The slope change from $0.8 - 1.3$ to $2.2 - 3.0$ indicates the transition from spontaneous to stimulated emission.
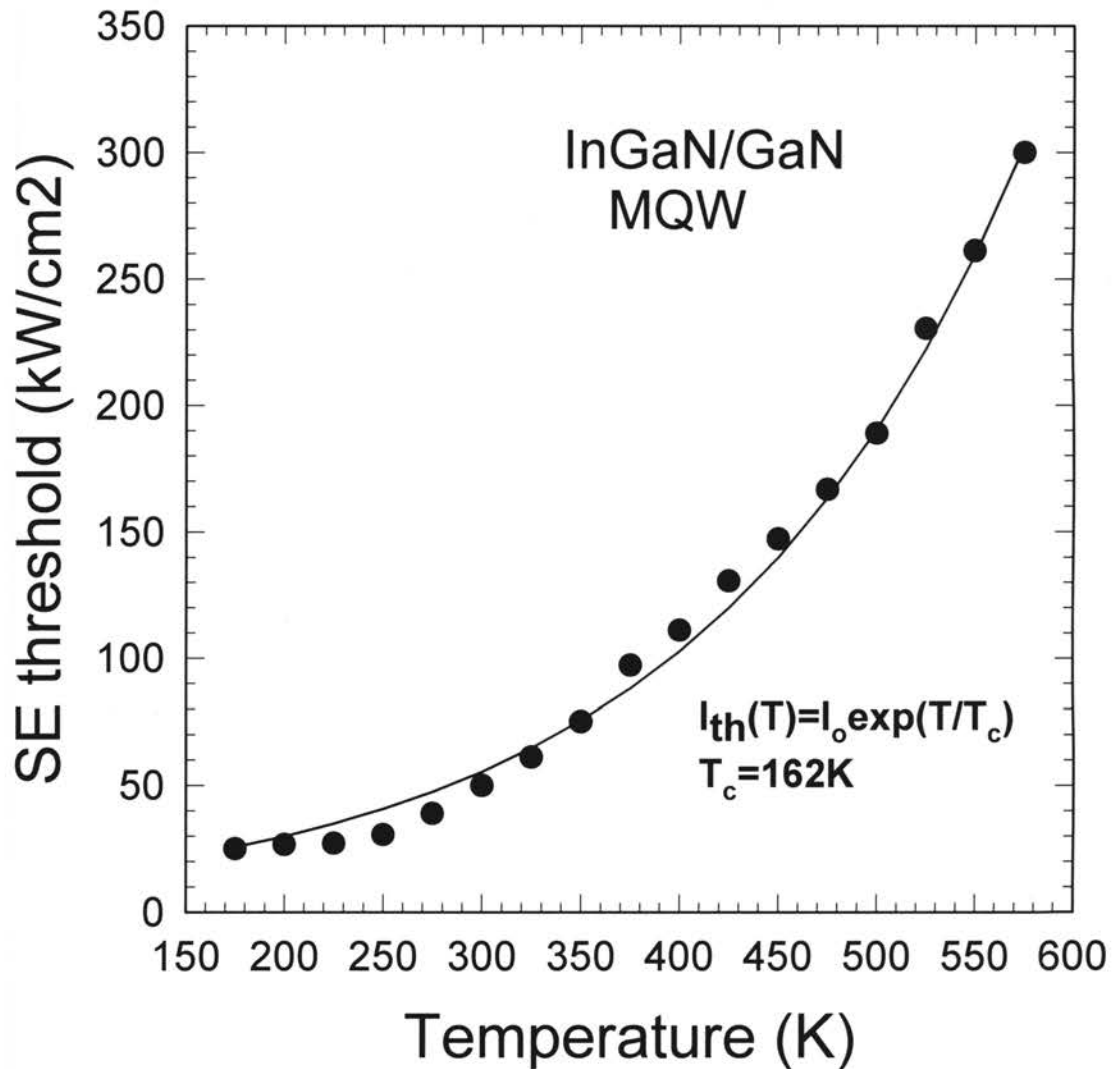
Figure 23. Temperature dependence of the SE threshold in the temperature range of 175 - 575 K for an $In_{0.18}Ga_{0.82}N$/GaN MQW. The solid line represents the best least-squares fit to the data (solid dots). A characteristic temperature of this best fit is 162 K.

Excitation Condition Dependence of Optical Transition

Excitation Energy Dependence of Luminescence

The excitation photon energy dependence of the spontaneous and stimulated emission from InGaN-based structures provides important information about the energy boundary between localized and extended (or delocalized) band tail states, as well as the dynamics of carrier generation and transfer. We will review recent studies of the excitation energy dependence of the InGaN PL and PLE spectra of InGaN/GaN MQWs.[121,122]

Figure 24 shows 10 K $In_{0.18}Ga_{0.82}N$ luminescence spectra measured with four different excitation photon energies E_{exc} of (A) 3.81, (B) 3.54, (C) 3.26, and (D) 2.99 eV. Each E_{exc} is indicated over the PLE spectrum for reference. The InGaN *main* and *secondary peaks* are shown at energies of 2.80 and ~2.25 eV, respectively. The oscillations in the main PL peak are due to Fabry-Perot interference fringes. When E_{exc} varies from above (curve A) to below (curve B) the near-band-edge emission energy E_g of the AlGaN capping layer ($E_{g,AlGaN}$), the relative intensity ratio of the main peak to the secondary peak noticeably changes. For $E_{exc} < E_{g,GaN}$, the secondary peak has nearly disappeared, while the main peak remains (curve C). When the excitation energy is further decreased to just above the InGaN main emission peak (curve D), no noticeable change is observed for the PL shape except for a decrease in the overall intensity of the emission. The inset in Figure 24 shows the normalized spectra for the main peak on a linear scale. As the excitation energy is decreased (from curve A to curve D), the intensity of the lower energy side of the main peak is reduced, whereas that of the higher

energy side is enhanced. This results in a ~7 meV blueshift of the peak energy and a narrower spectral width for the main peak with decreasing excitation energy. These facts strongly indicate that the recombination mechanism of the InGaN emission is very much affected by the excitation (or carrier generation) conditions, as we will see later.

The upper part of Figure 25 shows the 10 K PLE spectra for the $In_{0.18}Ga_{0.82}N$ main PL emission for detection at (a) 2.87, (b) 2.81, (c) 2.75, and (d) 2.68 eV. The PL spectrum for $E_{exc} = 3.81$ eV is shown in the middle part of this figure for reference. The absorption edge of the InGaN wells is seen at about 3.1 eV. When the PLE detection energy is set below the peak energy $E_{p,InGaN}$ of the main InGaN emission (curves c and d), the contributions from the InGaN wells, the GaN barriers, and the AlGaN capping layer are clearly distinguishable, but when the detection energy is above and at $E_{p,InGaN}$ (curves a and b), the PLE signal below $E_{g,AlGaN}$ shows almost a constant intensity across the $E_{g,GaN}$ region, indicating that carrier generation in the InGaN rather than in the GaN plays an important role. In both cases, the PLE signal above $E_{g,AlGaN}$ abruptly decreases because of absorption in the $Al_{0.07}Ga_{0.93}N$ capping layer. When the detection energy is below $E_{p,InGaN}$ (curves c and d), the contributions of both the GaN and AlGaN regions are enhanced compared to the curves a and b: as the detection energy decreases, the PLE signal above $E_{g,GaN}$ increases with respect to the almost flat region of the PLE signal between $3.15 - 3.4$ eV. Therefore, with $E_{exc} > E_{g,GaN}$, the lower energy side of the InGaN main emission peak is mainly due to carrier generation in the GaN barriers and subsequent carrier transfer to the InGaN wells. Based on the different PLE contributions

to the higher and lower energy sides of $E_{p,InGaN}$, one can expect different recombination mechanisms for various excitation energies, as will be described later.

The lower part of Figure 25 shows the 10 K PLE spectra for the secondary peak with detection at (e) 2.57, (f) 2.41, (g) 2.24, and (h) 2.01 eV. When the detection energy is higher than 2.24 eV (as for curves e and f), the InGaN wells still partly contribute to the secondary peak emission, but with the detection energy at or below 2.24 eV (curves g and h), the contribution of the InGaN wells almost disappears. Note that as the detection energy decreases, the relative contributions of the GaN and the AlGaN cap layer significantly increase. These facts indicate that the main source of the secondary peak is not the InGaN wells, but predominantly the AlGaN capping layer and partly the GaN layers (consistent with the so-called *yellow luminescence band*). This observation was also confirmed by PL measurements using the 325 nm line of a He-Cd laser with varying excitation intensities. As the He-Cd laser excitation intensity increases, the relative emission intensity ratio of the InGaN main peak to the secondary peak increases. The intensity of the main peak increases linearly, but that of the secondary peak saturates with increasing excitation intensity. This also indicates that the secondary peak is defect-related emission. Therefore, the main peak is due to the InGaN wells, and the secondary peak is mainly from the AlGaN capping layer and the GaN barriers. For $E_{exc} > E_{g,AlGaN}$, most carriers are generated in the AlGaN capping layer and these photogenerated carriers partly migrate into the MQW region (where they cause the main peak) and partly recombine via defect-related luminescence in the AlGaN layer itself and the GaN barriers (where they cause the secondary peak).

69

The PLE observations of the InGaN/GaN MQWs are closely related to the carrier dynamics in the time domain. TRPL was measured at 10 K for different E_{exc}. Time integrated PL spectra showed the same behavior observed in the above cw PL measurements for the InGaN main emission, as shown Figure 24: a blueshift of the peak energy and a spectral narrowing of the lower energy side as E_{exc} decreases from above $E_{g,AlGaN}$ to below $E_{g,GaN}$. The carrier recombination lifetime becomes longer with decreasing emission energy, and therefore, the peak energy of the emission redshifts as time progresses, as shown in Figure 9. No significant change in lifetime at and above the peak energy position ($\tau_{eff} \sim 12$ ns at the peak position) was observed when E_{exc} was varied. However, the peak position redshifted faster for the $E_{exc} > E_{g,GaN}$ case than for the $E_{exc} < E_{g,GaN}$ case, and after ~20 ns, the peak position is almost the same for both cases. The starting peak position is lower for the $E_{exc} > E_{g,GaN}$ case than for the $E_{exc} < E_{g,GaN}$ case, so for the $E_{exc} > E_{g,GaN}$ case, the redshifting behavior with time is smaller and most carriers recombine at relatively lower energies. The carriers generated from the GaN barriers (or AlGaN capping layer) migrate toward the InGaN wells, and the carrier transfer allows the photogenerated carriers to have a larger probability of reaching the lower energy states at the MQW interfaces. This may be due to more binding and scattering of carriers by interface defects and roughness, enhancing trapping and recombination rates at the interface related states. Therefore, the lower emission peak energy position and the spectral broadening to lower energies for $E_{exc} > E_{g,GaN}$ indicate that the lower energy tail states are caused mainly by defects and roughness at the interfaces and not necessarily related to alloy fluctuations and impurities within the

70

InGaN wells, but for $E_{exc} < E_{g,GaN}$, the carriers responsible for the emission are directly generated within the InGaN wells, and thus, recombine at relatively higher emission energies.

Another interesting feature in the PLE spectra of Figure 25 is different slopes for $E_{exc} < 3.0$ eV in curves b, c, and d. To explain this, the PL was investigated as a function of excitation energy for $E_{exc} < E_{g,GaN}$. The second harmonic of a modelocked Ti:sapphire laser was used as a tunable excitation source. The excitation was normal to the sample surface. The emission was also collected normal to the sample surface, coupled into a 1-m spectrometer, and spectrally analyzed using a CCD. The excitation photon energy from the frequency doubled Ti:sapphire laser was tuned across the states responsible for the "soft" absorption edge of the InGaN layers. Spontaneous emission was observed for excitation photon energies over a wide spectral range above the spontaneous emission peak position (2.8 eV at 10 K). As the excitation photon energy was tuned from just below the bandgap of the GaN barrier layers to the high energy side of the InGaN absorption edge, no significant changes in the spontaneous emission spectra were observed. The only change was a decrease in the emission intensity as the excitation photon energy was tuned to the low energy side of the "soft" InGaN absorption edge, consistent with the reduction in the absorption coefficient with decreasing photon energy. However, as the excitation photon energy was tuned below ~2.98 eV, significant changes in the spontaneous emission spectra were observed, as illustrated in Figures 26 and 27. For excitation photon energies below ~2.98 eV, emission from the low energy side of the main InGaN PL peak became more and more pronounced (relative to the peak) with decreasing excitation photon energy. The spectra in Figure 26 are normalized

71

at 2.79 eV for clarity. Figure 27 clearly shows that the transition from localized to extended band tail states is at ~2.98 eV. This energy is the "mobility edge" of the band tail states, so that carriers with higher energy are free to migrate and those of lesser energy are spatially localized by deep potential fluctuations in the InGaN layers.

The redshift of the spontaneous emission as E_{exc} decreases across the InGaN absorption edge is explained as follows. When E_{exc} is higher than the mobility edge, the photogenerated carriers can easily populate the tail states by their migration, but their lifetimes are relatively short due to the presence nonradiative recombination channels. As E_{exc} is tuned below the mobility edge, the nonradiative recombination rate is significantly reduced, because the carriers are captured in small volumes and kept from nonradiative recombination sites. This increase in lifetime with decreasing E_{exc} results in increased radiative recombination from lower energy states. The mobility edge is ~180 meV above the spontaneous emission peak and ~130 meV below the start of the InGaN absorption edge. This confirms that extremely large potential fluctuations are present in the MQW InGaN active layers, leading to carrier confinement and efficient radiative recombination.
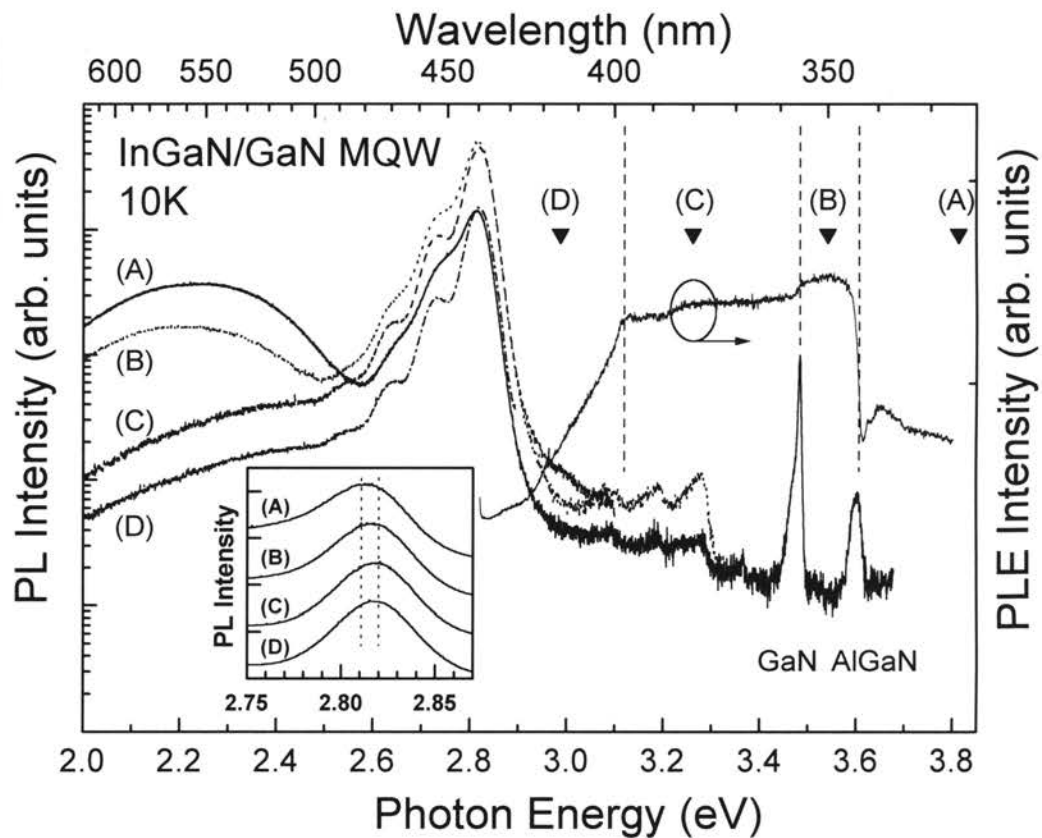
Figure 24. Evolution of PL of an $In_{0.18}Ga_{0.82}N/GaN$ MQW for excitation energies of (A) 3.81, (B) 3.54, (C) 3.26, and (D) 2.99 eV indicated over the PLE spectrum. Note the change in the intensity ratio of the main peak to the secondary peak. The inset shows a linear-scale plot of the normalized main emission spectra, which are shifted vertically for clarity.
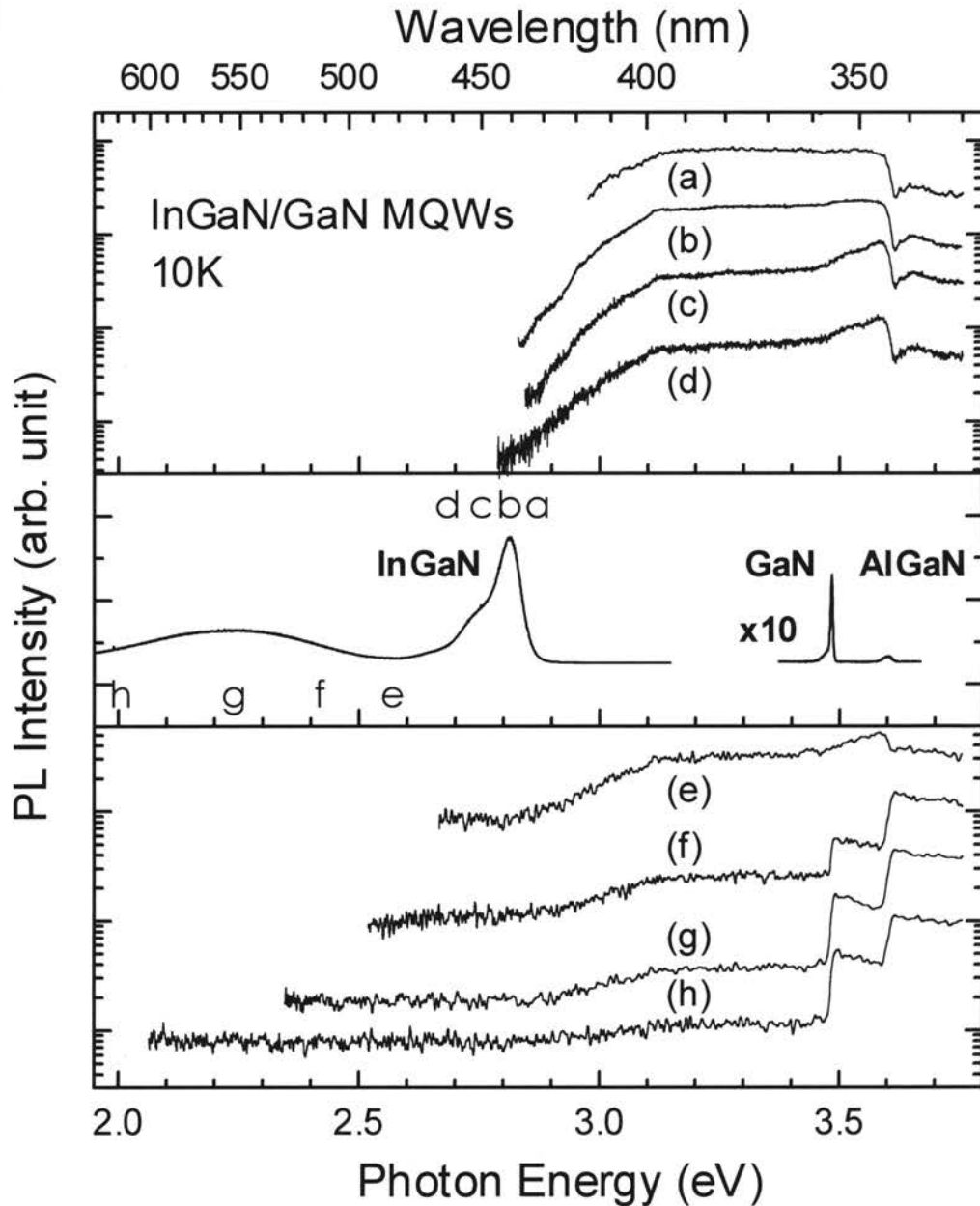
Figure 25. 10 K PLE spectra (upper and lower graphs) of an $In_{0.18}Ga_{0.82}N/GaN$ MQW at detection energies of (a) 2.87, (b) 2.81, (c) 2.75, (d) 2.68, (e) 2.57, (f) 2.41, (g) 2.24, and (h) 2.01 eV. The PL spectrum (middle graph) for an excitation energy of 3.81 eV is also shown for reference. The spectra are shifted vertically for clarity and the respective detection energies are indicated on the PL plot. As the detection energy decreases, the contribution of the $Al_{0.07}Ga_{0.93}N$ capping layer noticeably increases. When the detection energy is lower than 2.24 eV, the contribution of the $In_{0.18}Ga_{0.82}N$ wells is almost negligible.
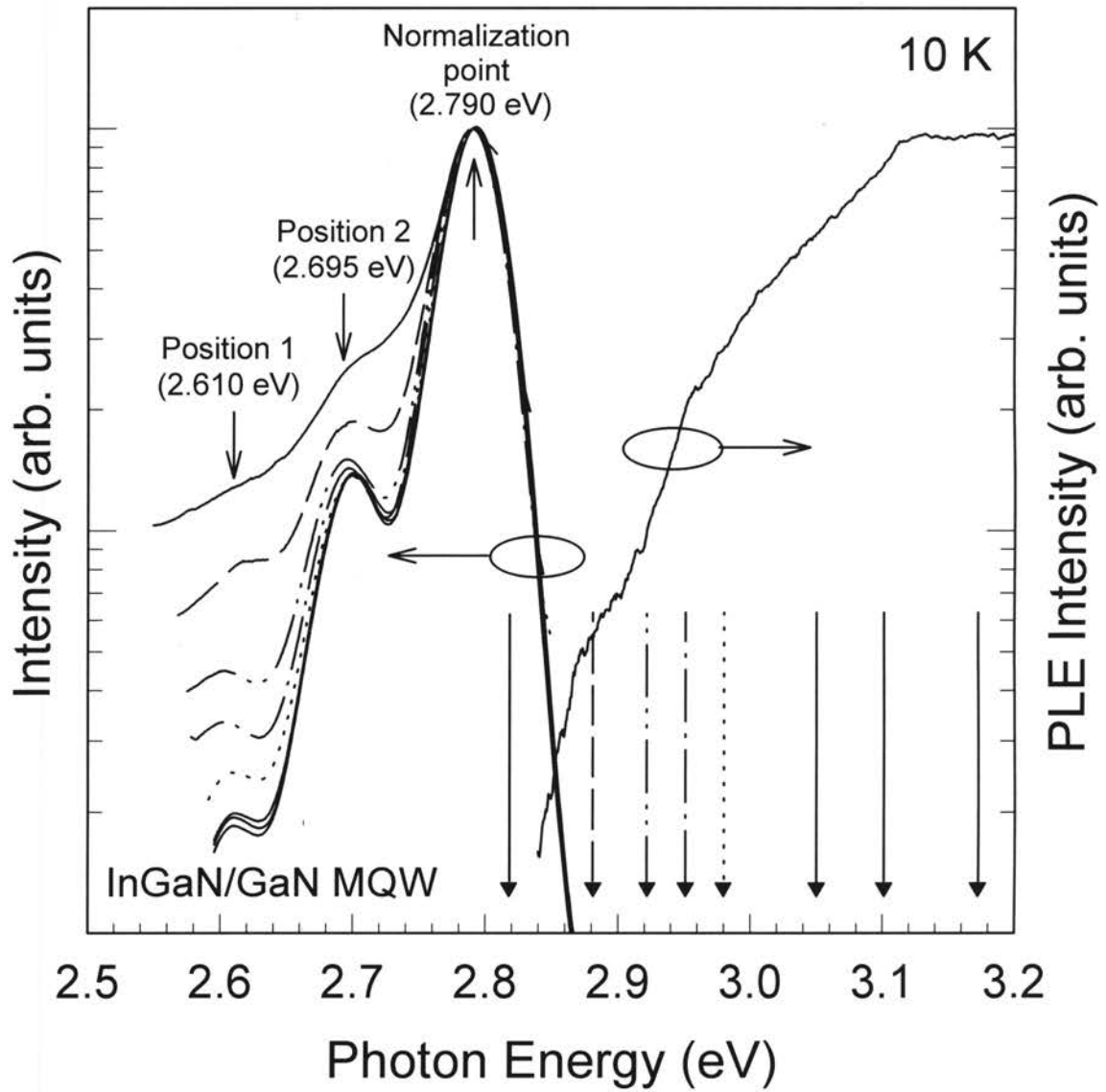
Figure 26. Spontaneous emission spectra of an $In_{0.18}Ga_{0.82}N$/GaN MQW with 2×10^{18} cm^{-3} Si doping in the GaN barriers as a function of excitation photon energy. The excitation photon energies for the spectra are indicated by the corresponding arrows. The spectra are normalized at 2.79 eV for clarity. The PLE absorption edge is also shown.
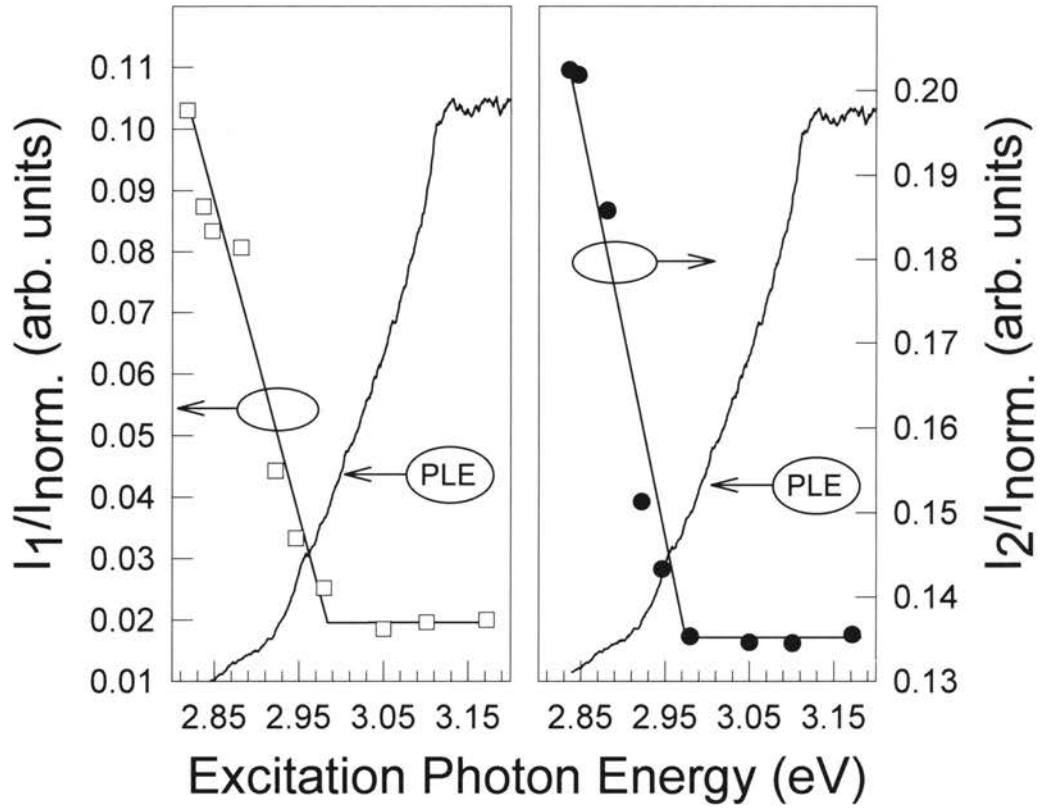
Figure 27. 10 K spontaneous emission intensity from an $In_{0.18}Ga_{0.82}N/GaN$ MQW at 2.61 eV (I_1) and 2.695 eV (I_2) relative to the peak emission intensity (at 2.79 eV) as a function of excitation photon energy. The solid lines are only guides for the eye. A clear shift in the emission lineshape is seen for excitation photon energies below ~2.98 eV. The absorption edge measured by PLE is also given (solid line) for comparison.

76

<u>Excitation Energy Dependence of Optically Pumped Stimulated Emission</u>

The SE dependence on excitation photon energy was investigated for InGaN/GaN MQWs, similarly to the excitation dependence of the spontaneous emission, to determine whether the carrier localization is also responsible for the SE.[66] The second harmonic of an injection seeded, Q-switched Nd:YAG laser (532 nm) pumped an amplified dye laser, and the red light from the dye laser was frequency doubled in a nonlinear crystal to obtain near UV to violet laser radiation for optically exciting the InGaN/GaN MQWs. This laser had a ~4 ns pulse width and a 10 Hz repetition rate, and was focused to a line on the sample surface. The excitation spot size was about 100×5000 μm. The emission from the sample was collected from one edge of the sample, coupled into a 1-m spectrometer, and spectrally analyzed with a UV enhanced CCD. These SE experiments were performed on $In_{0.18}Ga_{0.82}N$/GaN MQWs with undoped ($n < 1 \times 10^{17}$ cm^{-3}) and Si doped ($n \sim 2 \times 10^{18}$ cm^{-3}) GaN barriers.

Figure 28 illustrates the change in the SE spectra with decreasing E_{exc} for the InGaN/GaN MQW with undoped GaN barriers, and Figures 29 and 30 show the behavior of the SE peak for the Si doped MQW. As E_{exc} is tuned to lower energies, no noticeable change is observed in the SE spectra until E_{exc} crosses a mobility edge (~3.0 eV and ~2.95 eV for the undoped and Si doped MQWs, respectively), and then, the SE peak rapidly redshifts with decreasing E_{exc}. The redshift of the SE peak as E_{exc} is tuned below ~2.95 eV (for the Si doped MQW) is consistent with the mobility edge behavior of the spontaneous emission, as described above, and is due to enhanced population inversion at lower energies as the carriers are confined more efficiently with decreasing E_{exc}. The

mobility edge observed for SE is ~110 meV above the spontaneous emission peak, ~62 meV above the SE peak, and ~185 meV below the absorption edge of the InGaN well regions. This further indicates that large potential fluctuations are present in the InGaN active regions, resulting in strong carrier localization. This explains the efficient radiative recombination (stimulated and spontaneous) observed in these structures, as well as the small temperature sensitivity of the SE.

As a measure of the coupling efficiency of the exciting photons to the gain mechanism responsible for the SE peak, Figure 30 shows $1/I_{th}$ plotted as a function of E_{exc} for the InGaN/GaN MQW with Si doped GaN barrier layers. Changes in $1/I_{th}$ correspond to changes in the PLE spectrum, which is also plotted in Figure 29. Four distinct slope changes are seen in the PLE spectrum. The first, at ~3.12 eV, marks the beginning of the "soft" absorption edge of the InGaN active region, whereas the other three, located at ~2.96 eV, 2.92 eV, and 2.87 eV suggest varying degrees of localization. The change in $1/I_{th}$ at ~3.1 eV is due to a significant decrease in the absorption coefficient as E_{exc} is decreased below the absorption edge and the mobility edge. The inset of Figure 30 shows a strong correlation between $1/I_{th}$ and the PLE spectrum over a wide energy range for both the Si doped and undoped MQWs. The correlation between the high carrier density behavior and the cw PLE indicates that carrier localization plays a significant role in both the spontaneous and stimulated emission.

Excitation Length Dependence of Stimulated Emission

Separate research groups have recently observed two different SE peaks from $In_xGa_{1-x}N$/GaN MQWs grown under different growth conditions and with slightly

78

different experimental conditions.[123-125] These experiments indicate that the two SE

peaks are characteristic of present state-of-the-art $In_xGa_{1-x}N$ based blue laser diodes and

that disagreements in the literature may be due to slightly different experimental

conditions. We will discuss the excitation length and the excitation density dependence

of SE in $In_xGa_{1-x}N/GaN$ MQWs. These experiments provide a better understanding of

the SE and lasing in these structures, which is important for the development and

optimization of laser diodes.

Typical power dependent emission spectra at 10 K for an $In_{0.18}Ga_{0.82}N/GaN$

MQW with barrier Si doping of $n = 2 \times 10^{18}$ cm^{-3} are shown in Figure 31 for an

excitation length L_{exc} of 1300 μm. At low I_{exc}, we see a broad spontaneous emission

peak at ~2.81 eV, similar to the low power cw PL. As I_{exc} increases, two SE peaks

appear, designated as SE peak (1) and SE peak (2). SE peak (1) first arises at ~2.90 eV

and grows superlinearly with increasing I_{exc}. As I_{exc} is further increased, SE peak (2)

emerges at ~2.86 eV and also grows superlinearly with increasing I_{exc}. SE peak (1) is

the statistical distribution of many narrow (~0.1 nm) emission lines, and no noticeable

broadening of these narrow emission lines occurs as the temperature increases from 10 K

to 575 K, as illustrated in Figure 21. Both SE peaks (1) and (2) originate on the high

energy side of the low power spontaneous emission peak (the dashed line in Figure 31)

and are more than 0.2 eV below the "soft" absorption edge. Both peaks are below the

mobility edge of ~2.98 eV determined from the energy-dependent PL and SE studies.

Both SE peaks are also highly TE polarized, with a TE to TM ratio of ~200. SE peak (2)

was studied in previous chapters and attributed to carrier localization because of

"mobility edge" behavior observed in the optically pumped SE spectra as the excitation

photon energy was varied. SE peak (1) must be due to a lower degree of carrier localization than SE peak (2), because SE peak (1) is also well below the mobility edge and the absorption edge, and because it occurs at too low an excitation power density I_{exc} for an electron-hole plasma. When I_{exc} becomes so high that the carrier density exceeds the Mott density,[126] the photogenerated carriers become an electron-hole plasma. Since SE peak (1) occurs at lower I_{exc} than SE peak (2), SE peak (1) cannot be caused by recombination in an electron-hole plasma.

Figure 32 shows the SE threshold pumping density I_{th} of SE peaks (1) and (2) as a function of L_{exc} at 10 K and RT. I_{th} for peak (2) is larger than that of peak (1) for all excitation lengths employed, but approaches that of peak (1) with increasing L_{exc}. The high I_{th} of peak (2) with respect to peak (1) indicates that it results from a lower gain process than that of peak (1). Figure 33 shows the peak positions of SE peaks (1) and (2) as a function of L_{exc} at 10 K and RT. For $L_{exc} < 500$ μm, SE peak (2) is absent, but SE peak (1) occurs at ~2.92 (2.88) eV at 10 (300) K with an I_{th} of ~100 (475) kW/cm^2. As I_{exc} increases and/or L_{exc} increases, SE peak (2) emerges at 2.86 (2.83) eV at 10 (300) K. The peak positions were measured at $I_{exc} = 2I_{th}$. At both 10 K and 300 K, as L_{exc} increases, SE peak (1) redshifts due to reabsorption, but SE peak (2) slightly blueshifts. The apparent blueshift of SE peak (2) with increasing L_{exc} is a result of the experimental conditions. Since I_{th} of SE peak (2) decreases rapidly with increasing L_{exc}, and $I_{exc} = 2I_{th}$, the peak positions for small L_{exc} are for I_{exc} much higher than for large L_{exc}. A slight redshift of SE peak (2) with increasing I_{exc}, due to lattice heating and many-

body effects, then causes the apparent blueshift with increasing L_{exc}. The redshift of SE

peak (1) with increasing L_{exc} can be explained by the higher intensity of longer

amplification saturating lower absorption levels. With fewer states at lower localized

levels than higher ones, the absorption saturates first at the lower levels, causing a

redshift. With mirrors added to the MQW to convert from SE to lasing, this redshift

would be reduced, because the carriers elevated by the absorbed light could be stimulated

by multiple passes of photons to reemit in the same direction determined by the mirrors.

SE peak (2) does not have this reabsorption-induced redshift with increasing L_{exc},

because the absorption is greatly reduced at its lower energy (see the PLE curve of Figure

31). One would also expect the gain to saturate more at lower energies, but we will see

that the gain curve is lower than the absorption edge.

This saturation behavior is consistent with the observation of Kuball et al.[70] of a

high-gain mechanism in the band tail region of MQWs with similar active regions. The

wide spectral range with gain is explained by compositional fluctuations. The redshift of

SE peak (1) with increasing L_{exc} agrees with the redshift of the optical gain curve with

increasing L_{exc} described by Mohs et al.[127] It is also agrees with the fact that the external

quantum efficiency of Nakamura's cw blue laser diodes *decreases* with increasing cavity

length.[71] State-of-the-art cw blue laser diodes have a structure similar to our MQWs, and

the gain mechanism of these laser diodes apparently corresponds to SE peak (1), because

I_{th} of SE peak (1) is lower than that of SE peak (2), because the wavelength of SE

peak (1) is close to that of the laser diodes,[128] and also because of the other above

mentioned similarities. However, we will see in Chapter VII that the epitaxial lateral

overgrowth technique has significantly improved InGaN-based device performance by

greatly reducing the defect density, but it also decreases the degree of potential fluctuation, so one would expect this technique to eliminate SE peak (2).

Figure 34 shows the emission intensity of SE peaks (1) and (2) as a function of I_{exc} for L_{exc} = 1300 μm at 10 K. The peak (1) intensity increases superlinearly ($\propto I_{exc}^{3.8}$) until I_{exc} reaches the I_{th} of peak (2), and then, the peak (1) intensity turns linear. Peak (2) takes gain from peak (1), most likely by competition for carriers and reabsorption of emitted photons. The same process is observed at RT and for various excitation lengths. This gain competition may hinder InGaN applications for high power laser diodes, in which increased excitation current and/or longer cavity lengths could change the emission behavior.
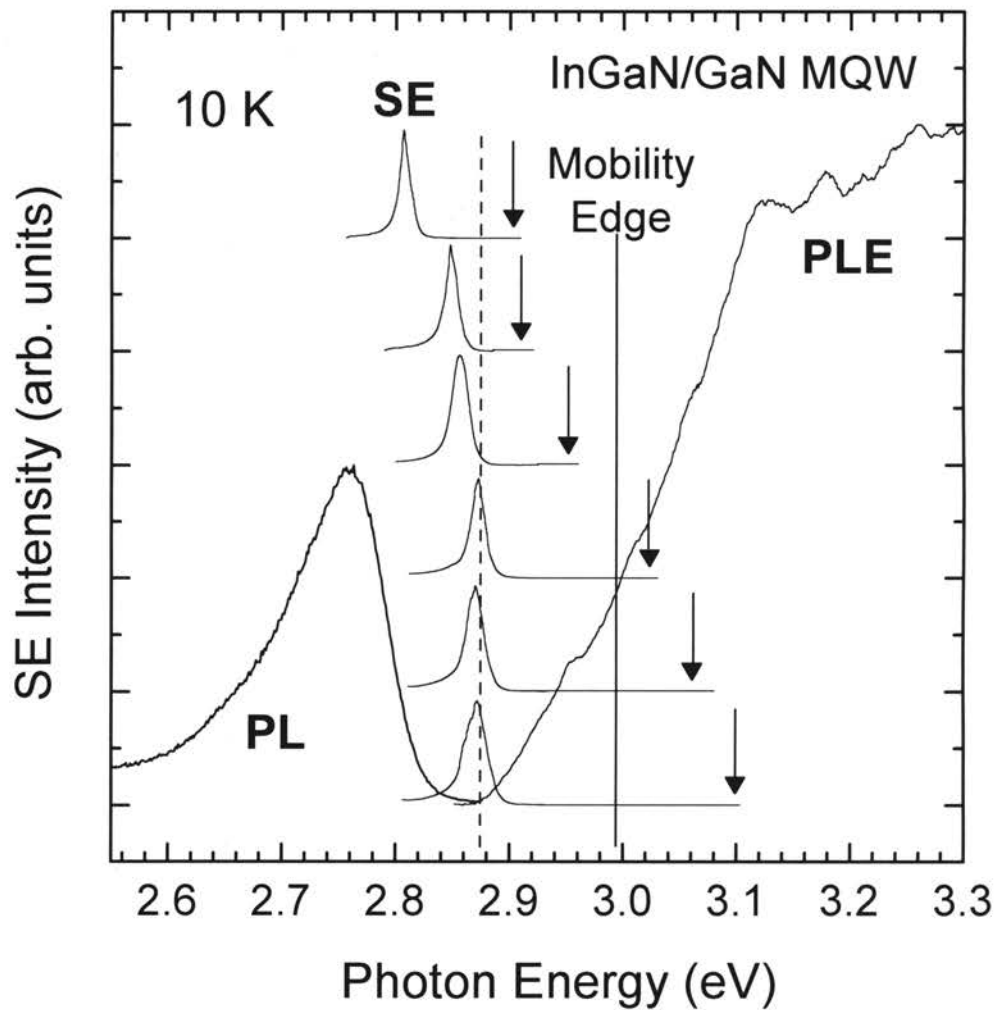
Figure 28. SE spectra as a function of excitation photon energy, E_{exc}, for an $In_{0.18}Ga_{0.82}N$/GaN MQW with undoped ($n < 1 \times 10^{17}$ cm^{-3}) GaN barriers. Mobility edge behavior is clearly seen in the SE spectra with decreasing E_{exc}. The SE peak redshifts with decreasing E_{exc}, as E_{exc} is tuned below the mobility edge. The excitation photon energies for the SE spectra are designated by arrows. The dashed line is at the unshifted SE peak position. The SE spectra are normalized and displaced vertically for clarity. PL and PLE spectra are also given for comparison.
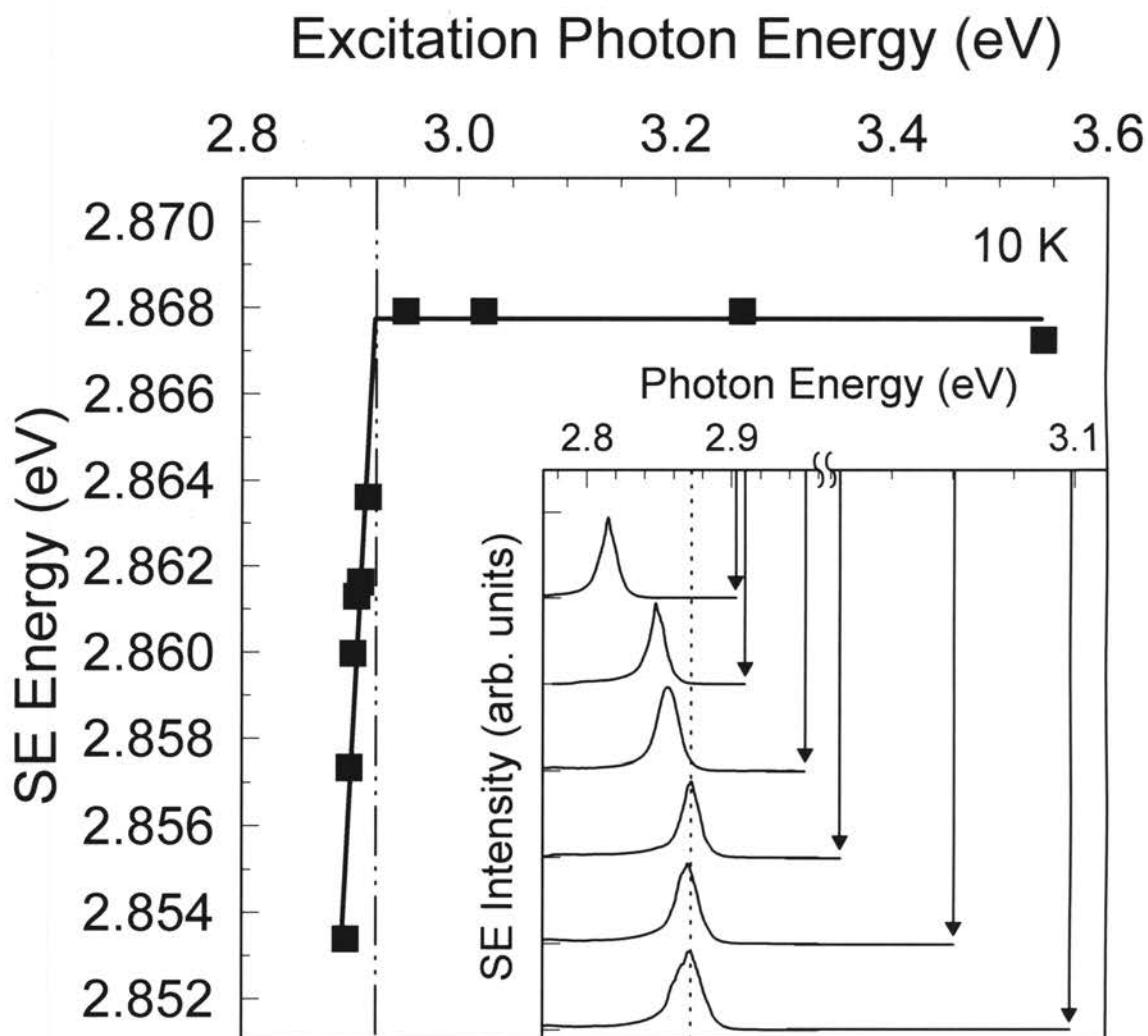
Figure 29. SE peak position as a function of excitation photon energy E_{exc} for an In$_{0.18}$Ga$_{0.82}$N/GaN MQW with 2×10^{18} cm^{-3} Si doping in the GaN barriers. Mobility edge behavior is clearly seen in the SE spectra with decreasing E_{exc}. The solid lines are given only as a guide for the eye.
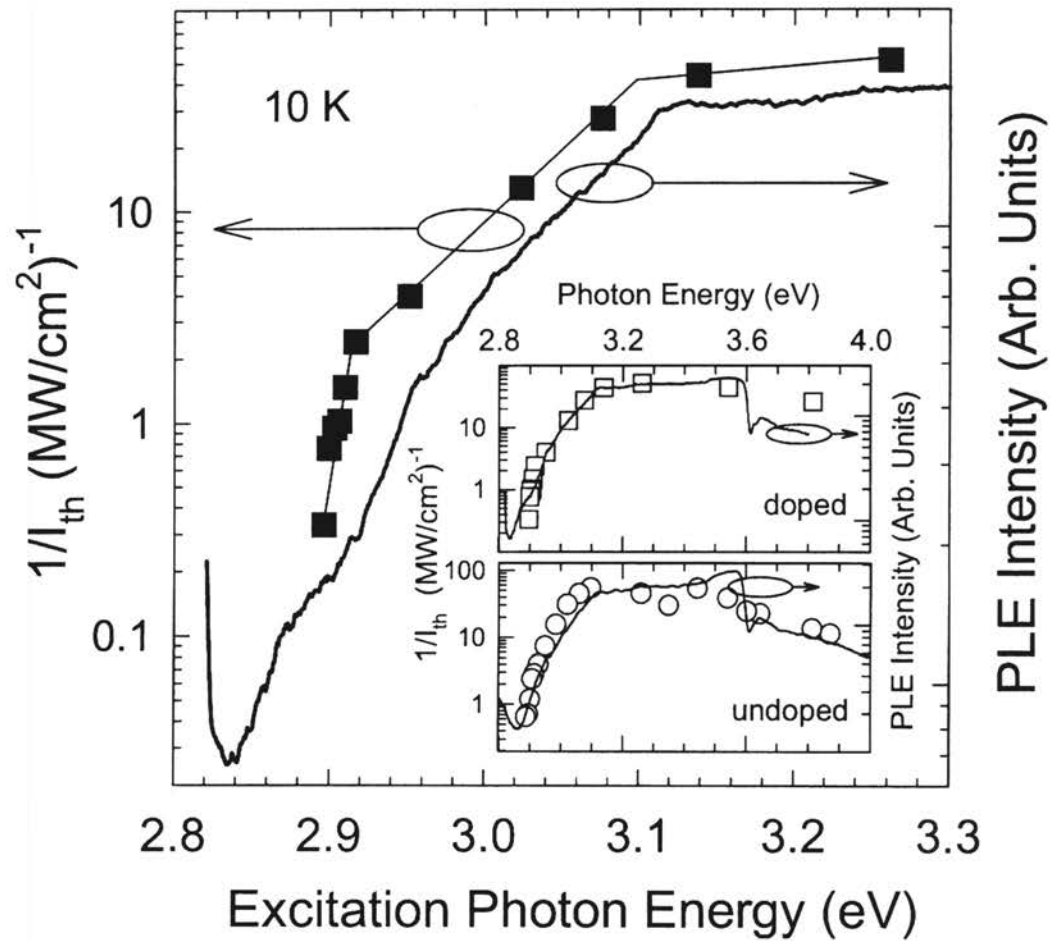
Figure 30. Inverse SE threshold as a function of excitation photon energy E_{exc} (solid squares) shown in comparison with the results of low-power PLE experiments (solid line) for a Si doped $In_{0.18}Ga_{0.82}N$/GaN MQW. The inset shows the same comparison over a wider energy range for both the undoped and Si doped InGaN/GaN MQWs, illustrating the similarities over the entire energy range.
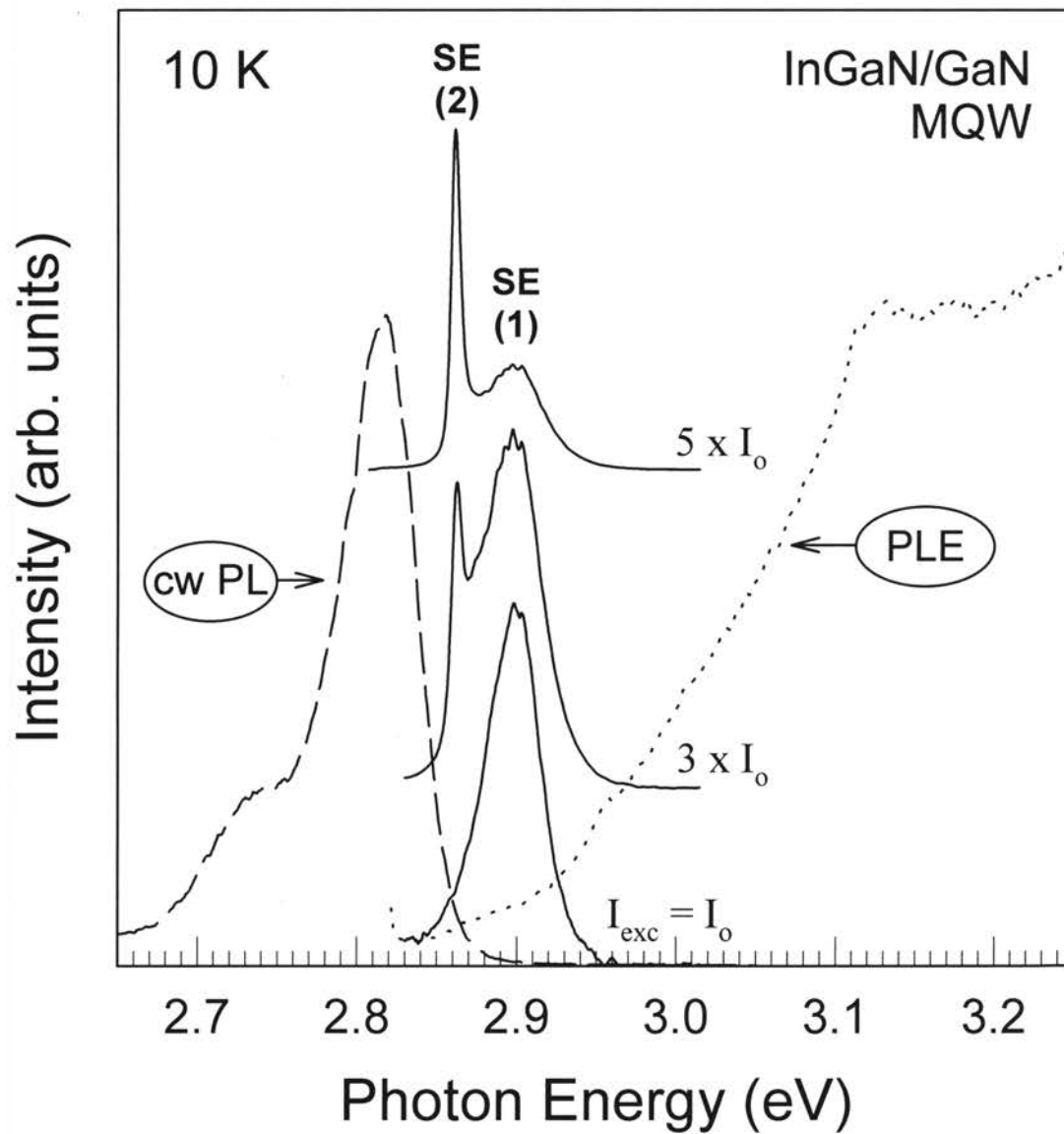
Figure 31. 10 K SE spectra (solid lines) from an $In_{0.18}Ga_{0.82}N$/GaN MQW at several excitation densities, where $I_0 = 100$ kW/cm^2. The low power PL (dashed line) and PLE (dotted line) spectra are also shown for comparison. The SE spectra are normalized and displaced vertically for clarity.
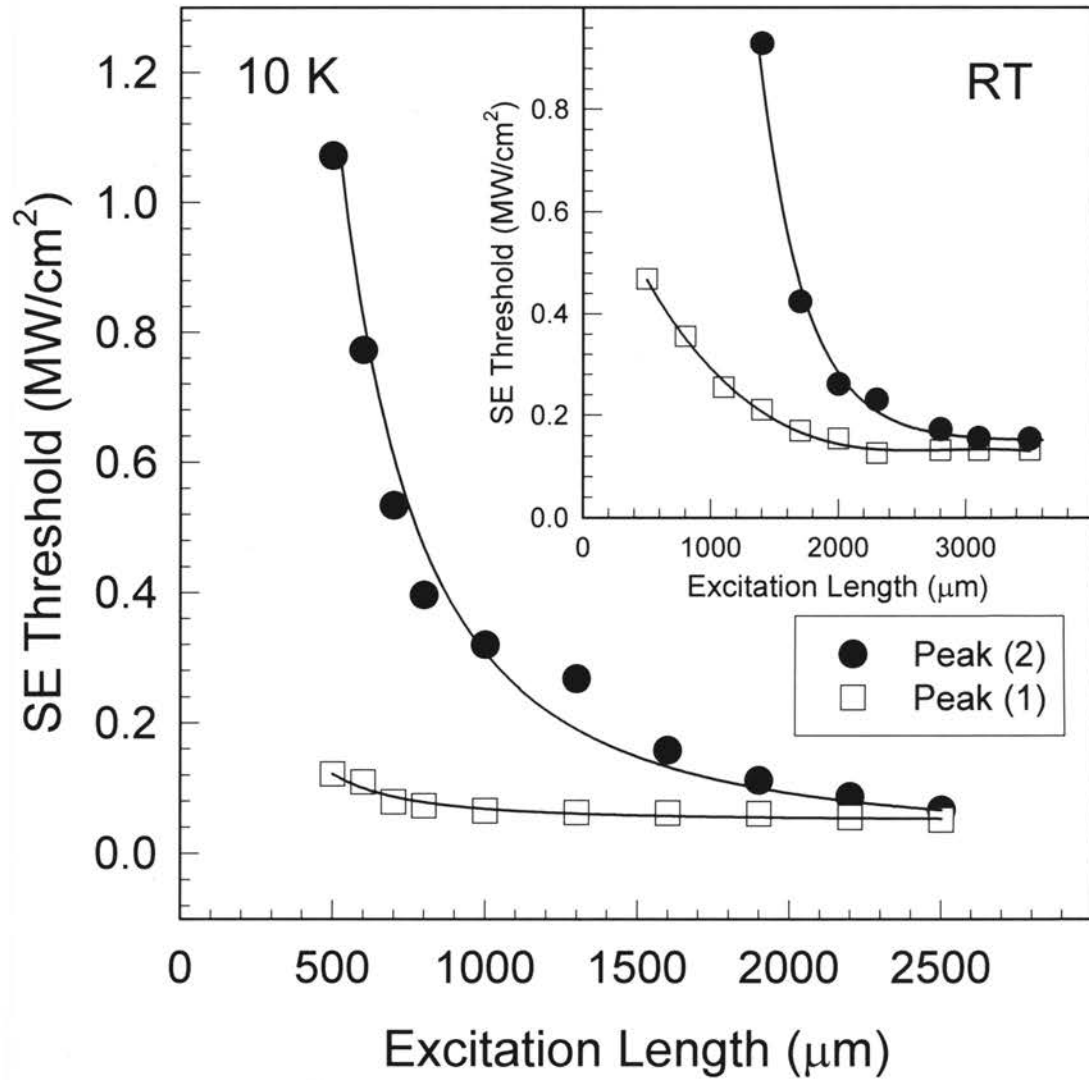
Figure 32. SE threshold as a function of excitation length for SE peaks (1) and (2) at 10 K and RT for an $In_{0.18}Ga_{0.82}N$/GaN MQW. The solid lines are guides for the eye.
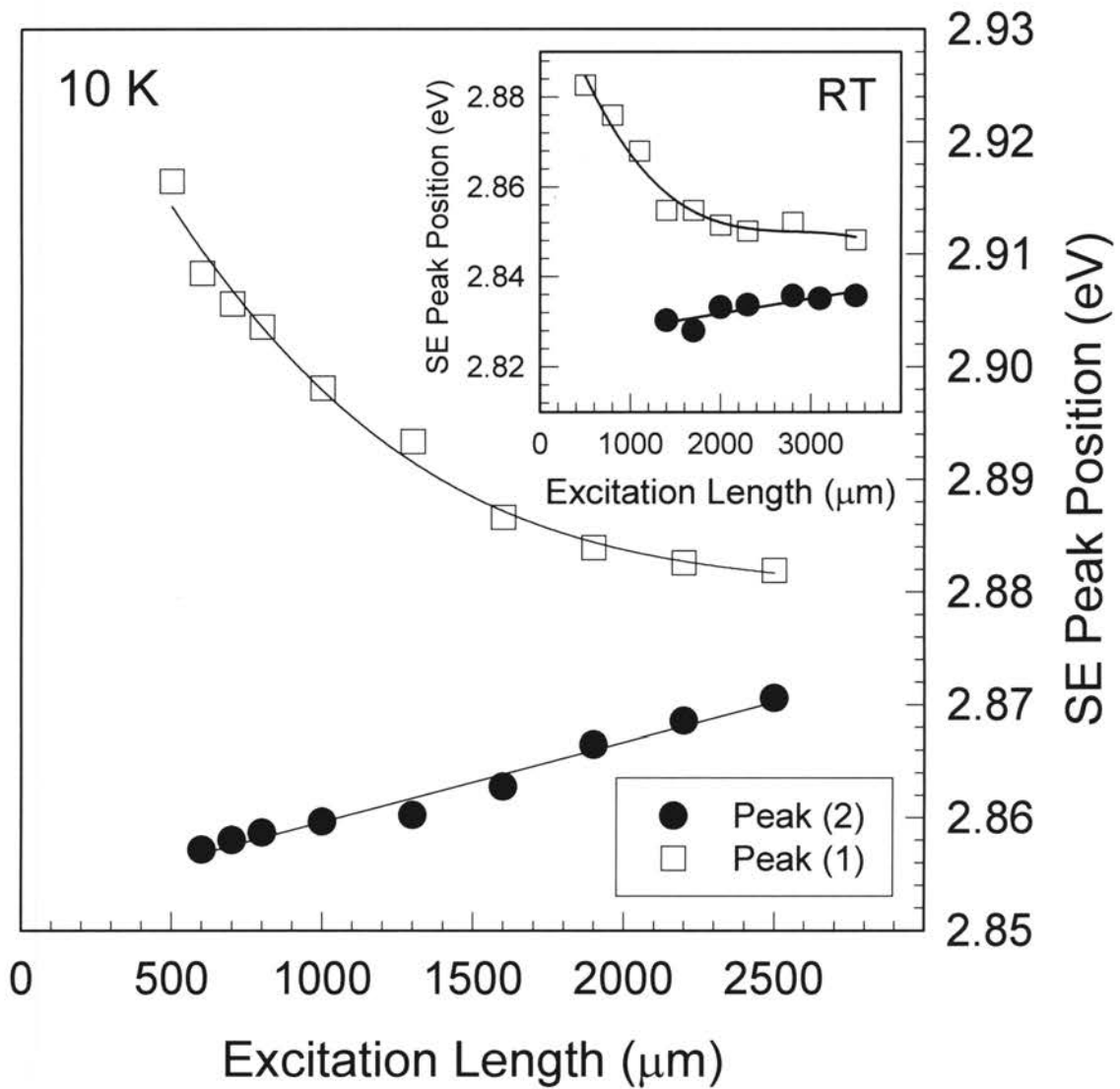
Figure 33. Peak position of SE peaks (1) and (2) as a function of excitation length at 10 K and RT for an $In_{0.18}Ga_{0.82}N$/GaN MQW. The solid lines are guides for the eye.
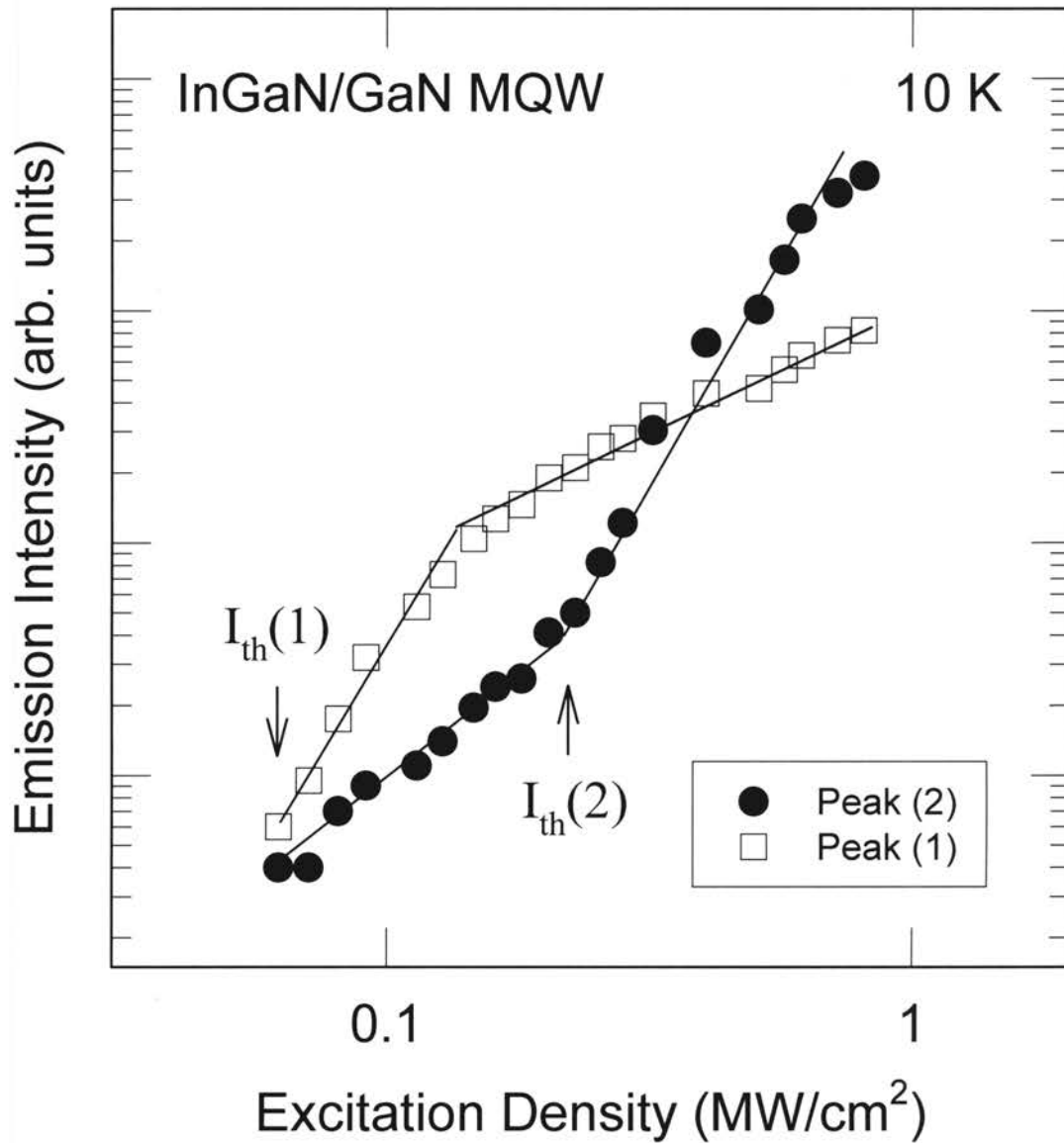
Figure 34. Intensity of $In_{0.18}Ga_{0.82}N$/GaN MQW SE peaks (1) and (2) as a function of optical excitation density at 10 K, illustrating gain competition between SE peaks (1) and (2). The excitation length is 1300 μm. The respective SE thresholds I_{th} of SE peaks (1) and (2) are indicated for completeness. The solid lines are only guides for the eye.

Summary

This chapter proved the importance of localized band tail states in $In_{0.18}Ga_{0.82}N$ epilayers and $In_{0.18}Ga_{0.82}N$ MQWs by the temperature-, excitation energy-, excitation density-, and excitation length-dependence of their emission properties. The band-tail states originate from large In alloy inhomogeneity, layer thickness variations, and/or defects. The photoluminescence peak energy has an "S-shaped" temperature dependence (redshift, blueshift, and then redshift with increasing temperature). Initially, with increasing temperature above 10 K, the charge carrier decay time increases, indicating the dominance of radiative recombination. This gives the carriers more opportunity to relax to lower energy band tail states before radiatively recombining, and this causes the initial redshift. With further temperature increases, the decay time decreases due to nonradiative processes, and this causes the blueshift. Then, with further temperature increases, the regular bandgap shrinkage causes a redshift, which is not as great as it would be without the band filling. This S-shaped temperature dependence of the PL peak energy cannot be explained in terms of an internal electric field created by piezoelectric polarization, although this has been a competing theory to that of carrier localization. Even up to RT, the relative blueshift of the spontaneous emission peak is seen for InGaN/GaN MQWs, and the emission peak energy is still lower than the mobility edge determined by energy-dependent PL and SE. This is evidence that carrier localization is important for the RT operation of InGaN/GaN MQW devices.

Optically pumped SE of InGaN/GaN MQWs was studied over a temperature range of 175 – 575 K, and the SE threshold has a characteristic temperature of 162 K. Strong evidence that SE in InGaN/GaN quantum wells is caused by recombination of

localized carriers rather than recombination in an electron-hole plasma is: (i) the SE FWHM is narrow and temperature invariant over 175 – 575 K (ii) the SE threshold density is extremely low, and (iii) the SE threshold has a rather weak temperature dependence. Also, the slopes of the integrated emission intensity below and above the SE threshold are independent of temperature. The low SE threshold and a weak temperature sensitivity of the SE threshold make InGaN MQWs attractive for the development of laser diodes operable well above RT.

The excitation energy dependence of the spontaneous and stimulated emission shows the energy boundary between localized and extended band tail states. An interesting change in PL spectra was observed with varying excitation photon energy above and below the GaN bandgap. The PL spectra were explained by the how the PLE spectra changed with detection energy. The lower energy tail states were found to be more related to the MQW interface defects and roughness than to alloy fluctuations and impurities within the InGaN wells. A mobility edge was found in both PL and SE spectra as the excitation photon energy was varied across the broadened absorption edge of the InGaN wells. The mobility edge is well above the PL and SE peak positions but well below the absorption edge, indicating that both the spontaneous and stimulated emission originate from carriers localized at low energy band-tail states due to extremely large potential fluctuations in the InGaN layers. Carrier localization was also shown to be the stimulated emission mechanism by much more evidence, such as a strong correlation between the inverse stimulated emission threshold density and the photoluminescence excitation spectrum.

The SE dependence of InGaN/GaN MQWs on excitation length and density was also investigated. Two distinctly different SE peaks were observed with different dependencies on excitation length. The high energy SE peak strongly redshifts with increasing excitation length due to competition between the gain and a saturable absorption tail, but the lower energy SE peak slightly blueshifts with increasing excitation length. The lower energy SE peak appears at higher excitation densities and/or excitation lengths and is detrimental to the higher energy SE peak, due to gain competition between the two peaks. The SE mechanism was shown to be the recombination of localized carriers, rather than recombination in an electron-hole plasma.

CHAPTER VI

OPTICAL GAIN AND NONLINEARITIES OF InGaN-BASED STRUCTURES

Optical nonlinear properties are important for optoelectronic applications, since they enable the absorption edge to be easily modified with optical excitation. This chapter presents optical gain and nanosecond nondegenerate pump-probe studies to provide insight into the mechanisms for stimulated emission and lasing in InGaN MQWs and epilayers.[74] The most distinctive nonlinear optical feature of InGaN-based structures is the pronounced filling of band tail states. Crystal imperfections, impurities, phonons, and carrier-carrier scattering broaden the absorption spectrum and create absorption tail states. The nonlinear absorption is affected by broadening, bandgap renormalization, state filling, Coulomb screening, and impurity absorption. A recent overview of the optically pumped SE and lasing properties of InGaN-based laser structures is given in Refs. 129 and 130.

Optical Gain Measurement by the Variable Stripe Method

A knowledge of the optical gain dependence on generated carrier density in InGaN-based structures is important for designing and optimizing laser diodes. We measured the optical gain of InGaN MQWs and epilayers, using the variable stripe excitation length method.[131,132] The samples were optically excited by the third harmonic (355 nm) of an injection seeded, Q-switched Nd:YAG laser (~5 ns FWHM, 10 Hz

repetition rate). The excitation beam was focused to a line on the sample surface using a cylindrical lens, and the excitation length was precisely varied with a mask controlled by a stepper motor. The emission was collected from a sample edge, coupled into a 1/4-m spectrometer, and spectrally analyzed using a UV enhanced CCD. The modal gain $g_{mod}(E)$ at energy E was determined from

$$\frac{I_1(E,L_1)}{I_2(E,L_2)} = \frac{\exp[g_{mod}(E)L_1]-1}{\exp[g_{mod}(E)L_2]-1}, \tag{15}$$

where L_1 and L_2 are two different stripe excitation lengths, and I_1 and I_2 are the corresponding emission intensities. Gain saturation effects were avoided by using stripe lengths shorter than those for which saturation occurs.

The modal gain spectra at 10 K as a function of above-gap optical excitation density are shown in Figure 35 (a) and Figure 35 (b) for an $In_{0.18}Ga_{0.82}N/GaN$ MQW and an $In_{0.18}Ga_{0.82}N$ epilayer, respectively. The excitation densities in Figure 35 are given with respect to the SE threshold measured for long (> 2000 μm) excitation lengths. The MQW has a clear blueshift in the gain peak with increasing optical excitation. This blueshift stopped for $E_{exc} > 12I_{th}$. Further increases in I_{exc} only increased the modal gain maximum. The MQW gain peaks in Figure 35 (a) are redshifted by more than 160 meV from the "soft" absorption edge of the InGaN wells. The large blueshift of the gain peak with increasing I_{exc} is consistent with band filling of localized states in the InGaN active layers. Similar behavior was observed at RT. The blueshift of the InGaN epilayer gain peak is much smaller than that of the MQW and stops at much lower excitation densities.

The 10 K PL, PLE, SE, and modal gain spectra are shown together in Figure 36 for (a) the $In_{0.18}Ga_{0.82}N/GaN$ MQW and (b) the $In_{0.18}Ga_{0.82}N$ epilayer. Note that the MQW figure covers twice the energy range of the epilayer figure. The SE spectra (solid lines) are shown for an excitation spot size of $\sim 100 \times 5000$ μm and for a pump density of $I_{exc} = 1.5I_{th}$, where I_{th} is the SE threshold. For both samples, the SE peak is at the low end of the absorption tail, but the SE peak is on the high energy side of the low power spontaneous emission PL peak for the MQW and slightly on the low energy side for the epilayer. The modal gain spectra were taken with I_{exc} much greater than I_{th} and with the excitation length less than 200 μm to minimize reabsorption. The modal gain maxima are 250 and 150 cm^{-1} for the MQW and the epilayer, respectively. The SE peak for long excitation lengths (> 5000 μm) is on the low energy tail of the gain curve measured for small excitation lengths (< 200 μm). This is explained by absorption saturation in the band tail region causing a redshift of the SE peak with increasing excitation length. Although the gain would also saturate, the absorption falls by a larger fraction across this spectral region. The modal gain curve for the MQW is much broader (FWHM of 24 nm, 160 meV) than that of the epilayer (FWHM of 7 nm, 50 meV), although the peaks of both curves are much lower than the upper side of the "soft" absorption edge. The fact that the MQW gain peak is below the mobility edge measured in excitation photon energy dependent studies described in the previous chapter is further evidence that localized states are the origin of optical gain in the InGaN/GaN MQWs. The facts that the InGaN epilayer SE peak is on the low energy side of its absorption tail and that its modal gain curve peak is below the "soft" absorption edge are evidence that carrier localization is

also the origin of optical gain in the epilayer, although the epilayer has a smaller degree of carrier localization.

Nondegenerate Pump-Probe Spectroscopy

In this section, nanosecond nondegenerate optical pump-probe absorption experiments on InGaN/GaN MQWs and InGaN epilayers provide further insight into the InGaN SE mechanism and how the "soft" absorption edge changes with increasing optical excitation density. The third harmonic of the Nd:YAG laser described above (355 nm) synchronously pumped the samples and a dye solution. The probe was the superradiant emission from the dye solution (covering the entire spectral range of the localized states) collected and focused onto the samples along with the pump beam. The probe intensity was several orders of magnitude lower than the pump beam intensity to avoid any nonlinear effects due to the probe. The probe spot size was ~1/3 that of the pump to minimize the role of variations in the pump intensity across the excitation spot. The transmitted broadband probe (with and without the pump beam) was then collected and coupled into a 1/4-m spectrometer and spectrally analyzed using a UV enhanced, gated CCD.

Figure 37 shows differential absorption spectra, $\Delta\alpha(I_{exc}) = \alpha(I_{exc}) - \alpha(0)$, of (a) the $In_{0.18}Ga_{0.82}N$ /GaN MQW and (b) the $In_{0.18}Ga_{0.82}N$ epilayer near the fundamental absorption edge at 10 K. The oscillatory structure is a result of thin film interference. With increasing I_{exc} of the above-gap pump pulse, $\alpha(I_{exc})$ decreases significantly in the band tail region. This absorption bleaching of the band tail states is clearly seen for both structures with increasing I_{exc}, and covers the entire spectral range of the absorption tails.

This bleaching saturated for I_{exc} exceeding ~2 MW/cm^2 at 10 and 300 K for the In$_{0.18}$Ga$_{0.82}$N epilayer. Similar behavior was observed for the In$_{0.18}$Ga$_{0.82}$N/GaN MQW sample, the only difference being a larger spectral region exhibiting absorption bleaching because of the larger band tailing of the MQW sample. Note that the absorption bleaching is quite large, exceeding 2×10^4 cm^{-1} at both 10 and 300 K. Both samples showed very different behavior in the $\alpha(I_{exc})$ and $\Delta\alpha(I_{exc})$ spectra than has been observed in GaN thin films.[133,134]

For both samples, the bleaching maximum (the $\Delta\alpha$ minimum) is at ~3.02 eV and is significantly blueshifted with respect to the luminescence maximum. This is because although radiative recombination is mainly from the lowest energy levels of potential minima, higher energy states are temporarily occupied by carriers relaxing from above the mobility edge. This decreases absorption to the higher energy states. Also, since the higher energy states start with a higher absorption, their absorption can be bleached more. An interesting difference between the two InGaN-based structures seen in Figure 37 is that as the pump density increases above I_{th}, the bleaching of the MQW tail states *decreases* significantly with increasing excitation, but the bleaching of the epilayer tail states continues to increase. The bleaching of the InGaN/GaN MQW decreases for excitation densities above I_{th} because of the fast depopulation of the states directly responsible for the SE. This gives carriers with energies above the SE peak a much greater number of available lower energy states, which results in a decrease in states occupied at these higher energies and, therefore, a decrease in bleaching for excitation densities above I_{th}. This is not seen in the epilayer, because its carrier lifetimes are much shorter, as shown in Figure 9, so that its states are already quickly depopulated.

This behavior has also been observed in other materials where intrinsic disorder through compositional fluctuations leads to carrier localization.[135] The fact that the carriers responsible for bleaching and SE share the same recombination channels is strong evidence that the MQW SE is due to localized state recombination. It is also important to note that the MQW bleaching maximum corresponds spectrally to the mobility edge (measured in the previous chapter), and the MQW modal gain shown in Figure 36 (a) (dotted line) corresponds spectrally with the low energy tail of the localized state absorption bleaching shown in Figure 37 (a), with the crossover from gain to absorption (the energy with zero gain on the high energy side of the gain curve) corresponding approximately with the bleaching maximum, indicating that the gain originates from localized states. The InGaN epilayer modal gain peak shown in Figure 36 (b) corresponds spectrally with the bleaching maximum shown in Figure 37 (b), rather than the low energy side of the bleaching, as is the case for the MQW. This is more evidence that the epilayer has less carrier localization than the MQW.

Summary

The nonlinear optical properties of band tail states in highly excited InGaN/GaN MQWs and InGaN epilayers were investigated by variable-stripe gain spectroscopy and nanosecond nondegenerate optical pump-probe spectroscopy. The gain maximum blueshifted a large amount with increasing above-gap optical excitation in variable stripe gain spectroscopy. This blueshift was attributed to the filling of localized band tail states due to the intense optical pump. The wide spectral region covered by the blueshift shows that there are large potential fluctuations in the InGaN active layers. Nanosecond nondegenerate optical pump-probe spectroscopy of the near band edge transitions showed

strong absorption bleaching (induced transparency) of band tail states with increasing above-gap optical excitation. The MQW bleaching decreased when SE began, indicating that the carriers responsible for bleaching and SE share the same recombination channels. These results are strong evidence for the dominance of localized state recombination in the gain and SE spectra of the InGaN/GaN heterostructures. Also, the InGaN/GaN MQW optical gain maxima (see Figure 35), both below and above the SE threshold excitation density, are below the mobility edge (~2.95 eV) measured in the excitation energy dependent PL and SE experiments, and the induced transparency maximum of the MQW (see Figure 37) corresponds spectrally to the mobility edge. The experimental results in this chapter strongly indicate that localized carriers responsible for band tail state bleaching share the same recombination channels as the carriers responsible for optical gain and SE in InGaN/GaN MQWs. This is strong evidence that the SE mechanism is the recombination of localized carriers.
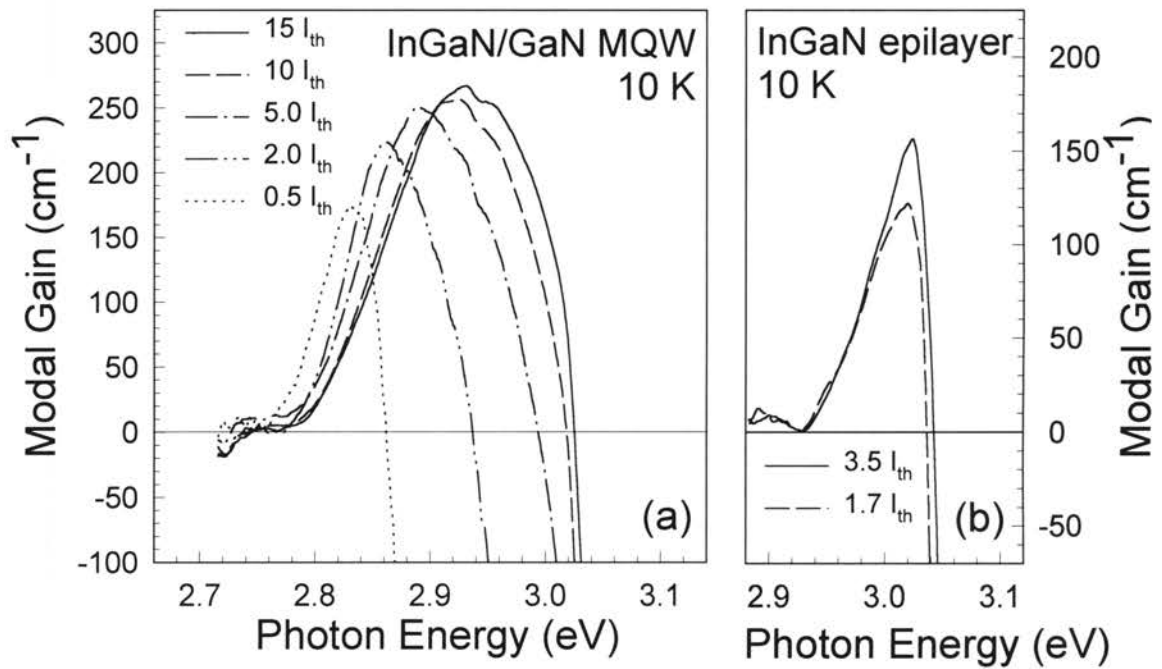
Figure 35. 10 K modal gain spectra of (a) an $In_{0.18}Ga_{0.82}N/GaN$ MQW and (b) an $In_{0.18}Ga_{0.82}N$ epilayer as a function of above-gap optical excitation density. The excitation densities are given with respect to the SE threshold I_{th} measured for long excitation lengths (> 2000 μm). A clear blueshift in the gain maximum and the gain/absorption crossover point is seen with increasing excitation density for MQW. This trend is much weaker for the epilayer.
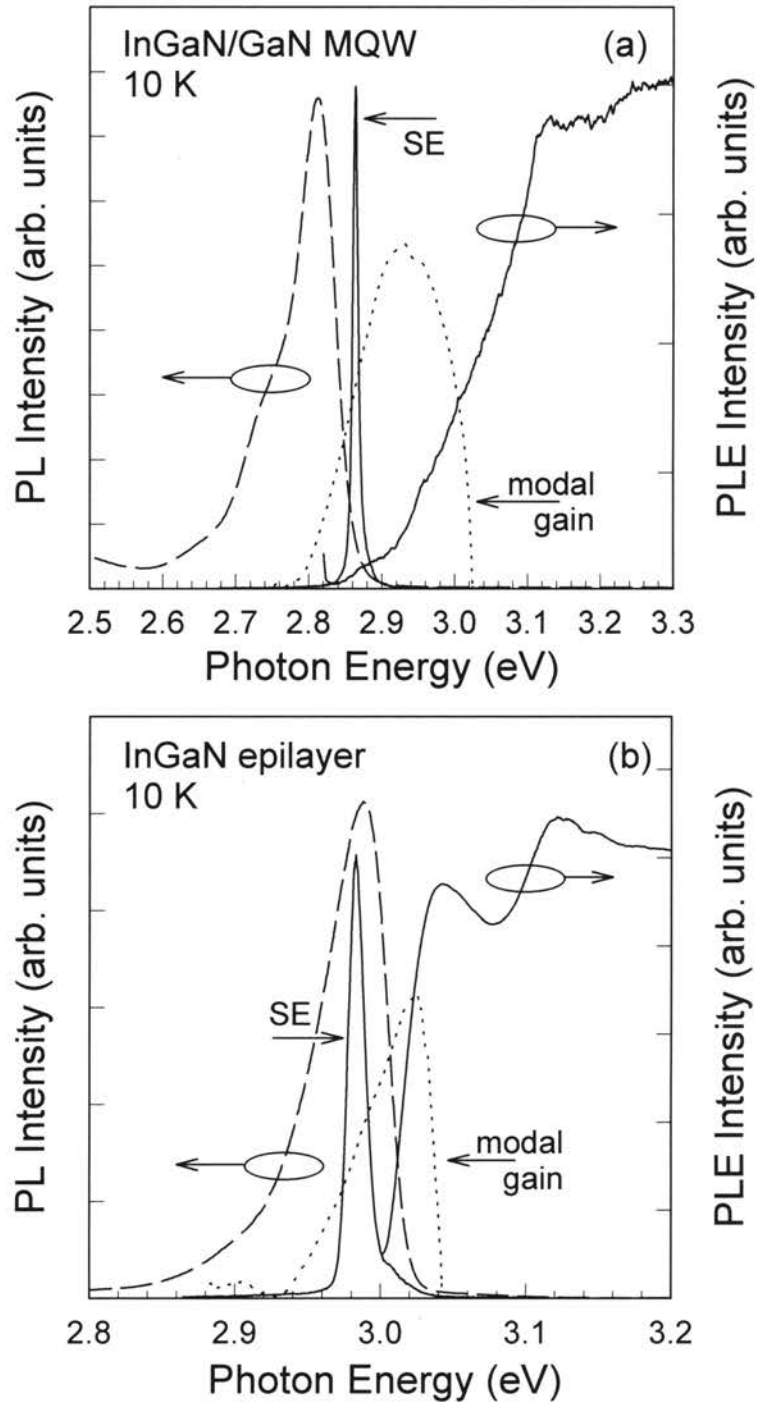
Figure 36. PL (dashed lines), SE (solid lines), and modal gain (dotted lines) spectra taken at 10 K from (a) an $In_{0.18}Ga_{0.82}N/GaN$ MQW and (b) an $In_{0.18}Ga_{0.82}N$ epilayer. The SE and gain spectra were measured for excitation lengths of > 5000 and < 200 μm, respectively. The maximum modal gain is 250 and 150 cm^{-1} for the $In_{0.18}Ga_{0.82}N/GaN$ MQW and $In_{0.18}Ga_{0.82}N$ epilayer, respectively. The low-density PLE spectra are also shown for reference.
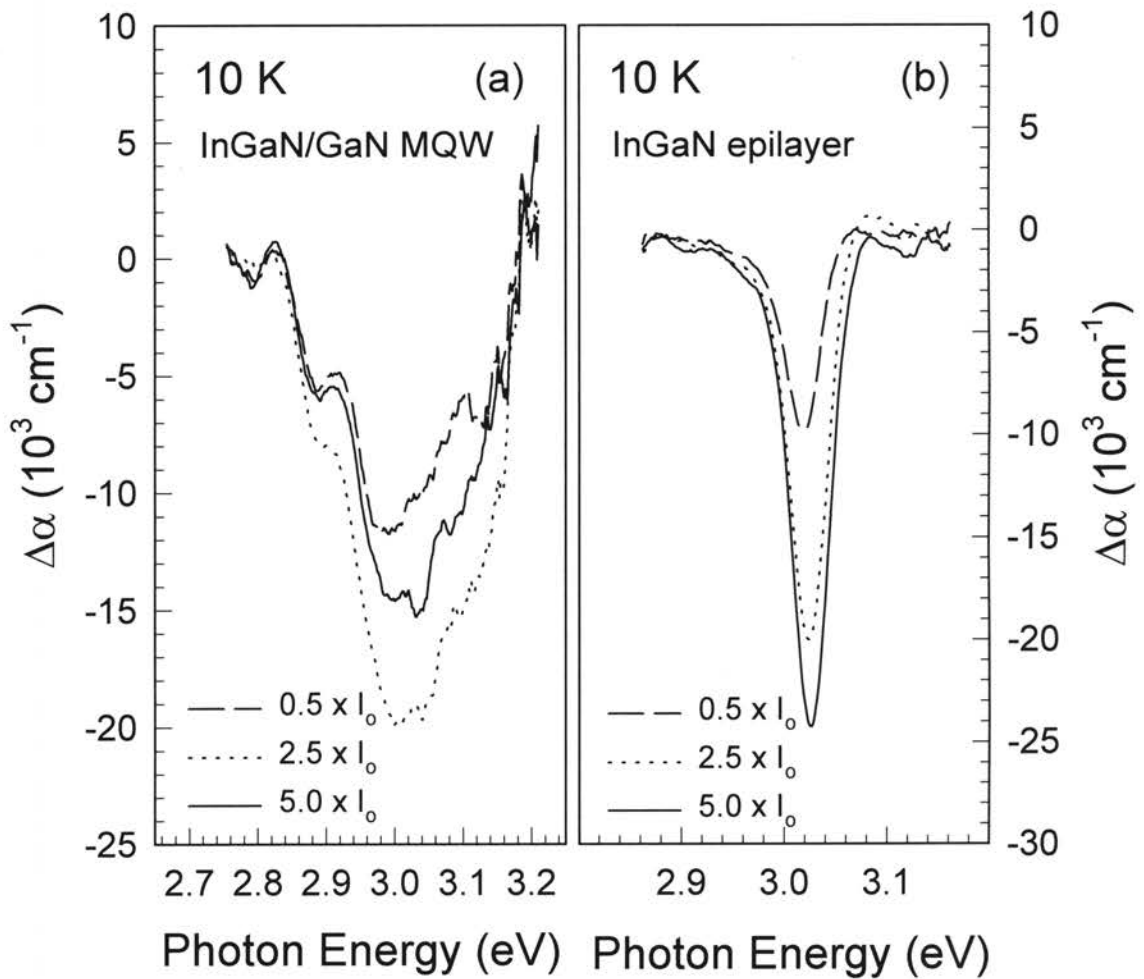
Figure 37. 10 K nanosecond non-degenerate pump-probe absorption change $\Delta\alpha$ for (a) an $In_{0.18}Ga_{0.82}N/GaN$ MQW and (b) an $In_{0.18}Ga_{0.82}N$ epilayer showing absorption bleaching ($\Delta\alpha$ negative) of band tail states with increasing excitation density, I_{exc}. $\Delta\alpha(I_{exc}) = \alpha(I_{exc}) - \alpha(0)$ and $I_0 = 100$ kW/cm^2.

CHAPTER VII

InGaN BURIED HETEROSTRUCTURES BY

EPITAXIAL LATERAL OVERGROWTH

After studying the emission mechanisms of InGaN-based devices, there are three

obvious ideas for improving device characteristics, such as efficiency, longevity, and

stimulated emission threshold. These ideas are 1) decrease the defect density, 2) decrease

the density of all defects, except the bandgap inhomogeneities caused by indium

concentration fluctuation, 3) make the indium fluctuations more uniform in size, shape,

and concentration profile, such as uniform quantum dots or quantum disks. A method

which has been very successful at greatly decreasing the defect density and improving the

device characteristics is epitaxial lateral overgrowth (ELO), which is also called lateral

epitaxial overgrowth (LEO).[136-137] Because of lattice mismatch with the substrate,

threading dislocations (edge dislocations) are created. In regular vertical growth,

threading dislocations, caused by lattice mismatch at the substrate, grow vertically

through the entire device, but lateral growth stops this. Also, Group III-nitride layers

grown vertically upon a laterally grown layer have a much lower defect density.

The ELO technique starts with growing a striped mask (SiO_2,[137,138] Si_3N_4,[139] or

SiN_x[140]) over a GaN layer. The initial GaN layer is usually grown by MOCVD on

sapphire or silicon carbide. Stripe windows in the mask are formed by reactive ion

etching or photolithography, usually along $\langle 1\bar{1}00 \rangle$ planes, and sometimes along $\langle 11\bar{2}0 \rangle$

planes. The windows are typically $5 - 8$ μm wide with a periodicity of about 20 μm. Subsequent GaN growth begins on the window areas of exposed GaN, and then, proceeds laterally over the mask, as shown in Figure 38. The growth conditions are adjusted to enhance the lateral to vertical growth ratio. The lateral growth reduces the dislocation density from between 10^8 and 10^{10} cm^{-2} to ~10^6 cm^{-2}. However, the dislocation density is still high directly above the windows and in the regions where two lateral GaN wings coalesce. For this reason, it is better to grow the device structures above a laterally overgrown wing, but not directly over a coalescence region in the center of a wing. There are many variations of ELO. For example, Motoki, *et al.* obtained freestanding GaN by ELO over a SiO$_2$ mask on GaAs.[141] The GaAs was easily dissolved in aqua regia (a mixture of nitric and hydrochloric acids). The SiO$_2$ mask had 2 μm round openings in a six-fold rotational symmetry. They grew the GaN by HVPE, which is a much faster growth technique than MOCVD, but they obtained a dislocation density in the epitaxial laterally overgrown GaN (ELOG) of only 2×10^5 cm^{-2}.

Many articles have shown that ELO improves the performance of InGaN based devices. By using ELOG, Nichia Chemical Industries fabricated InGaN MQW LDs with an estimated lifetime of 15,000 hours at a case temperature of 60°C and a continuous wave output power of 30 mW.[142] At a case temperature of 25°C, the lasing threshold current was 23 mA, which corresponded to 1.9 kA/cm^2. This performance was also enabled by improved optical and carrier confinement through cladding layers of GaN/AlGaN modulation-doped strained-layer superlattices (MD-SLSs). The GaN/AlGaN MD-SLSs were used instead of AlGaN to prevent cracking from lattice mismatch. To fabricate these LDs, they first grew ELOG by MOCVD over a sapphire

substrate. Next, they grew upon the ELOG an additional 200 μm of GaN by HVPE. Then, they polished away the ELOG and part of the HVPE GaN to obtain a freestanding 150 μm GaN substrate. Upon this freestanding GaN, they grew another ELOG layer. Finally, they grew the LD structures. The device performance was also improved because the front and rear reflective surfaces of the LDs were obtained through cleaving, which is not possible with GaN still attached to a sapphire substrate, since sapphire has a different crystallographic orientation. Tojyo *et al.* obtained reflective cleaved surfaces of less than 1 nm roughness for ELOG, which is much better than the greater than 10 nm roughness for GaN on sapphire.[143] They compared InGaN-based LDs fabricated on ELOG and sapphire. The lasing threshold current for the LD on ELOG and the LD on sapphire was 53.4 mA and 57.0 mA, respectively. The slope efficiency of the LD on ELOG and the LD on sapphire was 1.21 W/A and 0.92 W/A, respectively, so the LD on ELOG had an operating current at 30 mW light output power of 10 mA lower than the LD on sapphire. By using ELOG, Hansen *et al.* increased the internal quantum efficiency of InGaN-based LDs from 3% to 22%, and they decreased the threshold current density from 10 kA/cm^2 to 4.8 kA/cm^2.[144]

Different researchers have obtained different results for the effect of ELO on InGaN-based LEDs, but it is generally agreed that ELO very much improves LDs. By using ELOG, Sasaoka *et al.* increased the light output efficiency of InGaN MQW LEDs by a factor of three.[145] They found that the Mg diffusion, induced by threading dislocations, was much lower, and the reverse bias leakage current was reduced by two orders of magnitude. For example, Mukai *et al.* found that LEDs on ELOG and sapphire had about the same output power of 6 mW at a current of 20 mA, although the LED on

sapphire had much higher leakage current, indicating that the threading dislocations form a current leakage path.[146] Although InGaN-based LEDs on ELOG have a much smaller threading dislocation density, they still have localized states, as seen by the typical luminescence Stokes shift[147] and the blueshift with increasing excitation.[146] This shows that In fluctuation does not originate at threading dislocations. Nichia Chemical Industries compared the effect of ELO on LEDs that emit at a wavelength of less than 380 nm with those that emit above 380 nm.[148] They found that for emission below 380 nm, the external quantum efficiency was much better for InGaN-based LEDs on ELOG at high current, but the same at low current. At low current, many of the carriers are captured into localized states so that they do not migrate to nonradiative recombination centers. Although ELO reduces the density of nonradiative recombination centers, this is unnecessary at low current because of the localized states. However, at high current, many of the carriers overflow the localized states, so ELO becomes very important at high current. For LEDs that emit at less than 380 nm, but have a GaN active layer, ELOG is very helpful at both low and high current, because the GaN active layer does not have the localized states from In composition fluctuation. However, LEDs that emitted above 380 nm in the blue or green were not helped much by ELO, because their higher In concentration in the InGaN wells causes larger alloy composition fluctuations, and therefore, deeper localized energy states, which the carriers cannot easily overflow, even at high current.

The situation is different for InGaN-based LEDs and LDs. Although composition fluctuations keep carriers from migrating to nonradiative defects, the fluctuations are defects themselves and cause many problems for lasing.[149] They cause emission line

broadening, which increases internal loss and decreases differential gain, and the threshold lasing current is proportional to the emission linewidth. The fluctuations can create local fields that dissociate excitons, if they are not sufficiently confined. These defects perturb the local refractive index and scatter light. Hot spots, current filaments, and spectral hole burning also form at defects. Yamaguchi *et al.* found that, at a given In concentration in InGaN quantum wells, using an ELOG substrate decreases both the nonradiative defect density and the localized composition fluctuations.[150] Just as with LEDs, when the composition fluctuations are shallower, it is more important for the nonradiative defect density to be lower, because the carriers are more likely to overflow shallow localized states and migrate to nonradiative recombination centers. However, for stimulated emission and lasing, the composition fluctuations have other advantages and disadvantages, so the degree of fluctuation should be optimized.[151] For deep fluctuations, localized population inversion for stimulated emission occurs more easily, but the gain easily saturates and does not increase quickly with carrier density. However, for shallow fluctuations, there is a sharper rise in the density of states and the gain peak is narrower and rises more rapidly with carrier density, but a higher carrier density is required to achieve the stimulated emission threshold population inversion. Deeper fluctuations reduce the stimulated emission threshold carrier density, but they also reduce the differential gain. Fortunately, state-of-the-art InGaN-based LDs use ELO to obtain a medium, near optimum level of fluctuations while greatly decreasing the density of nonradiative recombination centers and current leakage paths.

One would suspect that InGaN-based LDs could be further improved by using ELO to obtain a buried heterostructure, as shown in Figure 39. Buried heterostructures

have the advantage of funneling carriers into a small volume, so that the lasing threshold carrier density is obtained at a much smaller current.[152,153] They also have excellent gain-guiding and index-guiding. A triangular prism shaped buried heterostructure could be used to guide carriers into a region of lower defect density. Electrons have a much higher mobility than holes in InGaN, and there is more difficulty with p-contacts and hole injection than electron injection, so with electron flow vertically upward in Figure 39, most of the recombination would be at the apex of the prism, in a region similar to a quantum wire.[154] A layer of SiO_2 over the prism top surfaces, except for the apex region, would electrically passivate these surfaces and ensure that the recombination occurred almost totally in the apex region. A disadvantage of this buried heterostructure is that the recombination region, which is similar to a quantum wire, would have a smaller volume, and therefore, a smaller output power. However, the advantages may overcome this disadvantage. Tanaka *et al.* tested GaN triangular cross section prisms that they made by selective area growth through openings in a SiO_2 mask.[155] However, their prisms were not covered with a barrier material, and only air was immediately above the prisms, so they could not be tested by electrical pumping. The benefits of buried heterostructures appear in electrical pumping, but not optical pumping. Also, threading dislocations ran from the sapphire substrates vertically through their prisms. There are various ways around this problem. For example, the prisms can be formed by ELO over a GaN layer that was previously formed by ELO, with the upper SiO_2 stripes formed over the windows in the lower SiO_2 layer. Also, the p- and n-contacts can be formed at the left and right corners at the bases of the prisms. This would cause the carrier recombination to occur mostly at the p-contact corners, because the electrons are much faster than the

holes, and unlike the holes, electrons tend to pass by defects, such as threading dislocations that may be in the middle of the prisms. Of course, it is important to optimize the growth procedures and choose a barrier material that is lattice matched to the prism InGaN active region.[156]
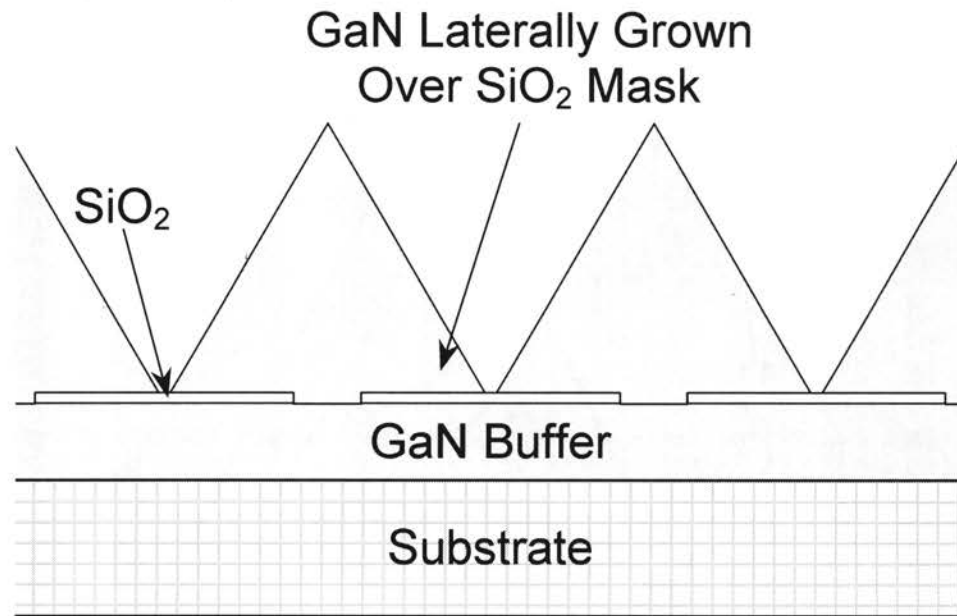
Figure 38. Epitaxial lateral overgrowth of GaN. GaN first grows vertically through openings in a SiO$_2$ mask. With the right growth conditions, the GaN forms prisms, which grow laterally over the SiO$_2$. With further growth, the prisms coalesce and form a flat top surface.
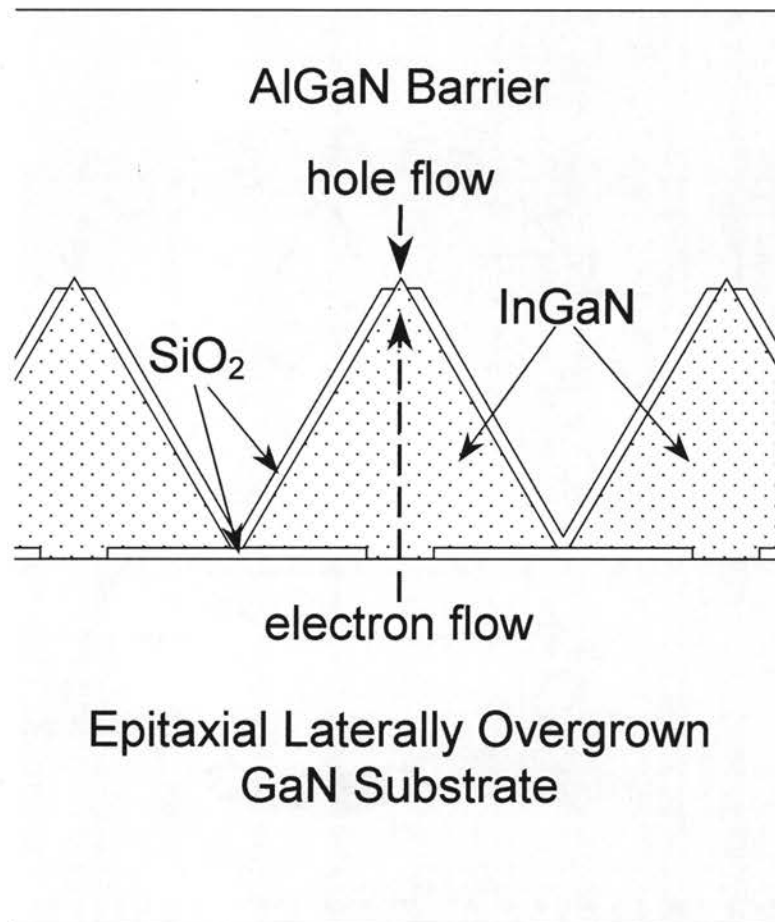
Figure 39. InGaN buried heterostructure formed by epitaxial lateral overgrowth. A SiO₂ mask is grown on a GaN substrate that was previously formed by epitaxial lateral overgrowth. Next, InGaN prisms grow from openings in the SiO₂ mask. Then, electrically passivating SiO₂ layers are grown over this structure, except for the prism apexes. A p-type barrier of GaN or AlGaN is then grown on top. Electron mobility and injection is much more efficient than that of holes, so most of the electron-hole recombination occurs near the apexes of the prisms.

BIBLIOGRAPHY

1. S. Nakamura and G. Fasol, *The Blue Laser Diode*, (Springer, New York, 1997).

2. S. Chichibu, T. Azuhata, T. Sota, and S. Nakamura, Appl. Phys. Lett. **69**, 4188 (1996); 70, 2822 (1997).

3. E. S. Jeon, V. Kozlov, Y. -K. Song, A. Vertikov, M. Kuball, A. V. Nurmikko, H. Liu, C. Chen, R. S. Kern, C. P. Kuo, and M. G. Craford, Appl. Phys. Lett. **69**, 4194 (1996).

4. P. Perlin, V. Iota, B. A. Weinstein, P. Wisniewski, T. Suski, P. G. Eliseev, and M. Osinski, Appl. Phys. Lett. **70**, 2993 (1997).

5. Y. H. Cho, J. J. Song, S. Keller, M. S. Minsky, E. Hu, U. K. Mishra, and S. P. DenBaars, Appl. Phys. Lett. **73**, 1128 (1998).

6. S. F. Chichibu, A. C. Abare, M. S. Minsky, S. Keller, S. B. Fleisher, J. E. Bowers, E. Hu, U. K. Mishra, L. A. Coldren, S. P. DenBaars, and T. Sota, Appl. Phys. Lett. **73**, 2006 (1998).

7. Y. Narukawa, Y. Kawakami, M. Funato, Sz. Fujita, Sg. Fujita, and S. Nakamura, Appl. Phys. Lett. **70**, 981 (1997).

8. Y. Narukawa, Y. Kawakami, Sz. Fujita, Sg. Fujita, and S. Nakamura, Phys. Rev. B **55**, R1938 (1997).

9. L. Nistor, H. Bender, A. Vantomme, M. F. Wu, J. Van Landuyt, K. P. O'Donnell, R. Martin, K. Jacobs, and I. Moerman, Appl. Phys. Lett. **77**, 507 (2000).

10. T. Takeuchi, H. Takeuchi, S. Sota, H. Sakai, H. Amano, and I. Akasaki, Jpn. J. Appl. Phys., Part 2 **36**, L177 (1997).

11. C. Wetzel, T. Takeuchi, S. Yamaguchi, H. Katoh, H. Amano, and I. Akasaki, Appl. Phys. Lett. **73**, 1994 (1998).

12. M. D. McCluskey, C. G. V. de Walle, C. P. Master, L. T. Romano, and N. M. Johnson, Appl. Phys. Lett. **72**, 2725 (1998).

13. S. Pereira, M. R. Correia, T. Monteiro, E. Pereira, E. Alves, A. D. Sequeira, and N. Franco, Appl. Phys. Lett. **78**, 2137 (2001).

14. S. Chichibu, K. Wada, and S. Nakamura, Appl. Phys. Lett. **71**, 2346 (1997).

15. X. Zhang, D. H. Rich, J. T. Kobayashi, N. P. Kobayashi, and P. D. Dapkus, Appl. Phys. Lett. **73**, 1430 (1998).

16. F. A. Ponce, D. P. Bour, W. Goltz, and P. J. Wright, Appl. Phys. Lett **68**, 57 (1996).

17. S. J. Rosner, E. C. Carr, M. J. Ludowise, G. Girolami, and H. I. Erikson, Appl. Phys. Lett. **70**, 420 (1997).

18. S. J. Rosner, G. Girolami, H. Marchand, P. T. Fini, J. P. Ibbetson, L. Zhao, S. Keller, U. K. Mishra, S. P. DeaBaars, and J. S. Speck, Appl. Phys. Lett. **74**, 2035 (1999).

19. D. W. Pohl, W. Denk, and M. Lanz, Appl. Phys. Lett. **44**, 651 (1984).

20. U. Dürig, D. W. Pohl, and F. Rohner, J. Appl. Phys. **59**, 3318 (1986).

21. E. Betzig, J. K. Trautman, T. D. Harris, J. S. Weiner, and R. L. Kostelak, Science **251**, 1468 (1991).

22. E. Betzig and J. K. Trautman, Science **257**, 189 (1992).

23. M. A. Paesler and P. Moyer, *Near-Field Optics: Theory, Instrumentation, and Applications* (Wiley, New York, 1996).

24. P. A. Crowell, D. K. Young, S. Keller, E. L. Hu, and D. D. Awschalom, Appl. Phys. Lett. **72**, 927 (1998).

25. A. Vertikov, M. Kuball, A. V. Nurmikko, Y. Chen, and S. -Y. Wang, Appl. Phys. Lett. **72**, 2645 (1998).

26. A. Vertikov, A. V. Nurmikko, K. Doverspike, G. Bulman, J. Edmond, Appl. Phys. Lett. **73**, 493 (1998).

27. D. L. Abraham, A. Veider, Ch. Schonenberger, H. P. Meier, D. J. Arent, and S. F. Alvarado, Appl. Phys. Lett. **56**, 1564 (1990).

28. B. Garni, J. Ma, N. Perkins, J. Liu, T. F. Kuech, and M. G. Lagally, Appl. Phys. Lett. **68**, 1380 (1996).

29. S. Evoy, C. K. Harnett, H. G. Craighead, S. Keller, U. K. Mishra, and S. P. DenBaars, Appl. Phys. Lett. **74**, 1457 (1999).

30. C. Gourdon and P. Lavallard, phys. stat. sol. (b) **153**, 641 (1989).

31. M. Oueslati, C. Benoit à la Guillaume, and M. Zouaghi, Phys. Rev. B **37**, 3037 (1988).

32. F. Bernardini, V. Fiorentini, and D. Vanderbilt, Phys. Rev. B **56**, R10024 (1997).

33. F. Bernardini and V. Fiorentini, Phys. Rev. B **57**, R9427 (1998).

34. V. Fiorentini, F. Bernardini, F. D. Sala, A. D. Carlo, and P. Lugli, Phys. Rev. B **60**, 8849 (1999).

35. M. Leroux, N. Grandjean, M. Laügt, J. Massies, B. Gil, P. Lefebvre, and P. Bigenwald, Phys. Rev. B **58**, R13371 (1998).

36. M. Leroux, N. Grandjean, J. Massies, B. Gil, P. Lefebvre, and P. Bigenwald, Phys. Rev. B **60**, 1496 (1999).

37. T. Takeuchi, S. Sota, M. Katsuragawa, M. Komori, H. Takeuchi, H. Amano, and I. Akasaki, Jpn. J. Appl. Phys., Part 2 **36**, L382 (1997).

38. T. Takeuchi, C. Wetzel, S. Yamaguchi, H. Sakai, H. Amano, I. Akasaki, Y. Kaneko, S. Nakagawa, Y. Yamaoka, and N. Yamada, Appl. Phys. Lett. **73**, 1691 (1998).

39. J. S. Im, H. Kollmer, J. Off, A. Sohmer, F. Scholz, and A. Hangleiter, Phys. Rev. B **57**, R9435 (1998).

40. A. Hangleiter, J. S. Im, H. Kollmer, S. Heppel, J. Off, and F. Scholz, MRS Internet J. Nitride Semicond. Res. **3**, 15 (1998).

41. H. Kollmer, J. S. Im, S. Heppel, J. Off, F. Scholz, and A. Hangleiter, Appl. Phys. Lett. **74**, 82 (1999).

42. R. Langer, J. Simon, O. Konovalov, N. Pelekanos, A. Barski, and M. Leszczynski, MRS Internet J. Nitride Semicond. Res. **3**, 46 (1998).

43. D. L. Smith and C. Mailhiot, Phys. Rev. Lett. **58**, 1264 (1987).

44. I. Vurgaftman, J. R. Meyer, and L. R. Ram-Mohan, J. Appl. Phys. **89**, 5815 (2000).

45. R. Langer, J. Simon, V. Ortiz, N. T. Pelekanos, A. Barski, R. André, and M. Godlewski, Appl. Phys. Lett. **74**, 3827 (1999).

46. D. A. B. Miller, D. S. Chemla, T. C. Damen, A. C. Gossard, W. Wiegmann, T. H. Wood, and C. A. Burrus, Phys. Rev. B **32**, 1043 (1985).

47. S.F. Chichibu, T. Sota, K. Wada, S.P. DenBaars, S. Nakamura, MRS Internet J. Nitride Semicond. Res. **4S1**, G2.7 (1999).

48. R. Cingolani, A. Botchkarev, H. Tang, H. Morkoç, G. Traetta, G. Coli, M. Lomascolo, A. Di Carlo, F. Della Sala, and P. Lugli, Phys. Rev. B **61**, 2711 (2000).

49. A. Bonfiglio, M. Lomascolo, G. Traetta, R. Cingolani, A. Di Carlo, F. Della Sala, P. Lugli, A. Botchkarev, and H. Morkoç, J. Appl. Phys. **87**, 2289 (2000).

50. G. Bastard, *Wave Mechanics Applied to Semiconductor Heterostructures* (Les Editions de Physique, Les Ulis Cedex, France, 1988), p. 309.

51. The simulation program used, "1D POISSON" by G. L. Snider, is available through the internet at http://www.nd.edu/~snider.

52. P. Ramvall, S. Tanaka, S. Nomura, P. Riblet, and Y. Aoyagi, Appl. Phys. Lett. **73**, 1104 (1998).

53. R. P. Leavitt and J. W. Little, Phys. Rev. B **42**, 11774 (1990).

54. C. I. Harris, B. Monemar, H. Kalt, P. O. Holtz, M. Sundaram, J. L. Merz, and A. C. Gossard, Phys. Rev. B **51**, 13221 (1995).

55. S. Chichibu, T. Sota, K. Wada, and S. Nakamura, J. Vac. Sci. Technol. B **16**, 2204 (1998).

56. W. W. Chow, H. Amano, T. Takeuchi, and J. Han, Appl. Phys. Lett. **75**, 244 (1999).

57. R. Dingle, K. L. Shaklee, R. F. Leheny, and R. B. Zetterstrom, Appl. Phys. Lett. **19**, 5 (1971).

58. J. S. Im, H. Kollmer, J. Off, A. Sohmer, F. Scholz, and A. Hangleiter, Phys. Rev. B **57**, R9435 (1998).

59. S. H. Park and S. L. Chuang, Appl. Phys. Lett. **72**, 3103 (1998).

60. R. Langer, J. Simon, V. Ortiz, N. T. Pelekanos, A. Barski, R. André, M. Godlewski, Appl. Phys. Lett. **74**, 3827 (1999).

61. F. Della Sala, A. Di Carlo, P. Lugli, F. Bernardini, V. Fiorentini, R. Scholz, and J. M. Jancu, Appl. Phys. Lett. **74**, 2002 (1999).

62. S. Bidnyk, J. B. Lam, B. D. Little, Y. H. Kwon, J. J. Song, G. E. Bulman, H. S. Kong, and T. J. Schmidt, Appl. Phys. Lett. **75**, 3905 (1999).

63. S. Nakamura, M. Senoh, S. Nahahama, N. Iwasa, T. Yamada, T. Matsushita, H. Kiyoku, and Y. Sugimoto, Jpn. J. Appl. Phys., Part 2 **35**, L217 (1996).

64. K. Domen, A. Kuramata, and T. Tanahashi, Appl. Phys. Lett. **72**, 1359 (1998).

65. S. Bidnyk, T. J. Schmidt, Y. H. Cho, G. H. Gainer, J. J. Song, S. Keller, U. K. Mishra, and S. P. DenBaars, Appl. Phys. Lett. **72**, 1623 (1998).

66. T. J. Schmidt, Y. H. Cho, G. H. Gainer, J. J. Song, S. Keller, U. K. Mishra, and S. P. DenBaars, Appl. Phys. Lett. **73**, 560 (1998).

67. H. X. Jiang and J. Y. Lin, Appl. Phys. Lett. **74**, 1066 (1999).

68. G. Frankowsky, F. Steuber, V. Härle, F. Scholz, and A. Hangleiter, Appl. Phys. Lett. **68**, 3746 (1996).

69. D. Wiesmann, I. Brener, L. Pfeiffer, M. A. Khan, and C. J. Sun, Appl. Phys. Lett. **69**, 3384 (1996).

70. M. Kuball, E. S. Jeon, Y. K. Song, A. V. Nurmikko, P. Kozodoy, A. Abare, S. Keller, L. A. Coldren, U. K. Mishra, S. P. DenBaars, and D. A. Steigerwald, Appl. Phys. Lett. **70**, 2580 (1997).

71. S. Nakamura, MRS Internet J. Nitride Semicond. Res. **2**, 5 (1997).

72. G. Mohs, T. Aoki, M. Nagai, R. Shimano, M. Kuwata-Gonokami, and S. Nakamura, Solid State Commun. **104**, 643 (1997).

73. Y. -K. Song, M. Kuball, A. V. Nurmikko, G. E. Bulman, K. Doverspike, S. T. Sheppard, T. W. Weeks, M. Leonard, H. S. Kong, H. Dieringer, and J. Edmond, Appl. Phys. Lett. **72**, 1418 (1998).

74. T. J. Schmidt, Y. H. Cho, G. H. Gainer, J. J. Song, S. Keller, U. K. Mishra, and S. P. DenBaars, Appl. Phys. Lett. **73**, 1892 (1998).

75. F. D. Sala, A. D. Carlo, P. Lugli, F. Bernardini, V. Fiorentini, R. Scholz, and J.-M. Jancu, Appl. Phys. Lett. **74**, 2001 (1999).

76. S. F. Chichibu, A. Shikanai, T. Deguchi, A. Setoguchi, R. Nakai, H. Nakanishi, K. Wada, S. P. DenBaars, T. Sota, and S. Nakamura, Jpn. J. Appl. Phys. Part 1 **39**, 2417 (2000).

77. Y. H. Cho, F. Fedler, R. J. Hauenstein, G. H. Park, J. J. Song, S. Keller, U. K. Mishra, and S. P. DenBaars, J. Appl. Phys. **85**, 3006 (1999).

78. R. W. Martin, P. G. Middleton, K. P. O'Donnel, and W. Van der Stricht, Appl. Phys. Lett. **74**, 263 (1999).

79. K. P. O'Donnell, R. W. Martin, and P. G. Middleton, Phys. Rev. Lett. **82**, 237 (1999).

80. S. Bidnyk, T. J. Schmidt, G. H. Park, and J. J. Song, Appl. Phys. Lett. **71**, 729 (1997).

81. C. I. Harris, B. Monemar, H. Amano, and I. Akasaki, Appl. Phys. Lett. **67**, 840 (1995).

82. C. K. Sun, S. Keller, G. Wang, M. S. Minsky, J. E. Bowers, and S. P. DenBaars, Appl. Phys. Lett. **69**, 1936 (1996).

83. C. K. Sun, T. L. Chiu, S. Keller, G. Wang, M. S. Minsky, S. P. DenBaars, and J. E. Bowers, Appl. Phys. Lett. **71**, 425 (1997).

84. J. S. Im, V. Härle, F. Scholz, and A. Hangleiter, MRS Internet J. Nitride Semicond. Res. **1**, 37 (1996).

85. B. K. Ridley, Phys. Rev. B **41**, 12 190 (1990).

86. J. Feldmann, G. Peter, E. O. Göbel, P. Dawson, K. Moore, C. Foxon, and R. J. Elliott, Phys. Rev. Lett. **59**, 2337 (1987).

87. W. Shan, X. C. Xie, J. J. Song, and B. Goldenberg, Appl. Phys. Lett. **67**, 2512 (1995).

88. P. Lefebvre, J. Allègre, B. Gil, A. Kavokine, H. Mathieu, W. Kim, A. Salvador, A. Botchkarev, and H. Morkoç, Phys. Rev. B **57**, R9447 (1998).

89. Y. Narukawa, S. Saijou, Y. Kawakami, S. Fujita, T. Mukai, and S. Nakamura, Appl. Phys. Lett. **74**, 558 (1999).

90. Y. H. Kwon, G. H. Gainer, S. Bidnyk, Y. H. Cho, J. J. Song, M. Hansen, and S. P. DenBaars, Appl. Phys. Lett. **75**, 2545 (1999).

91. S. Nakamura, M. Senoh, S. Nagahama, N. Iwasa, T. Yamada, T. Matsushita, H. Kiyoku, Y. Sugimoto, T. Kozaki, H. Umemoto, M. Sano, and K. Chocho, Appl. Phys. Lett. **72**, 2014 (1998).

92. X. H. Yang, T. J. Schmidt, W. Shan, J. J. Song, and B. Goldenberg, Appl. Phys. Lett. **66**, 1 (1995).

93. A. Krost, J. Böhrer, A. Dadgar, R. F. Schnabei, D. Bimberg, S. Hansmann, and H. Burkhard, Appl. Phys. Lett. **67**, 3325 (1995).

94. H. Sugiura, M. Mitsuhara, H. Oohashi, T. Hirono, and K. Nakashima, J. Cryst. Growth **147**, 1 (1995).

95. S. Ruvimov, Z. Liliental-Weber, T. Suski, J. W. Ager III, J. Washburn, J. Krueger, C. Kisielowski, E. R. Weber, H. Amano, and I. Akasaki, Appl. Phys. Lett. **69**, 990 (1996).

96. E. F. Schubert, I. D. Goepfert, W. Grieshaber, and J. M. Redwing, Appl. Phys. Lett. **71**, 921 (1997).

97. S. Keller, A. C. Abare, M. S. Minsky, X. H. Wu, M. P. Mack, J. S. Speck, E. Hu, L. A. Coldren, U. K. Mishra, and S. P. DenBaars, Material Science Forum **264-268**, 1157 (1998).

98. Y. H. Cho, T. J. Schmidt, S. Bidnyk, J. J. Song, S. Keller, U. K. Mishra, and S. P. DenBaars, MRS Internet J. Nitride Semicond. Res. **4S1**, G6.44 (1999).

99. P. A. Grudowski, C. J. Eiting, J. Park, B. S. Shelton, D. J. H. Lambert, and R. D. Dupuis, Appl. Phys. Lett. **71**, 1537 (1997).

100. S. Chichibu, D. A. Cohen, M. P. Mack, A. C. Abare, P. Kozodoy, M. Minsky, S. Fleischer, S. Keller, J. E. Bowers, U. K. Mishra, L. A. Coldren, D. R. Clarke, and S. P. DenBaars, Appl. Phys. Lett. **73**, 496 (1998).

101. A. Salvador, G. Liu, W. Kim, Ö. Aktas, A. Botchkarev, and H. Morkoç, Appl. Phys. Lett. **67**, 3322 (1995).

102. K. C. Zeng, J. Y. Lin, H. X. Jiang, A. Salvador, G. Popovici, H. Tang, W. Kim, and H. Morkoç, Appl. Phys. Lett. **71**, 1368 (1997).

103. H. J. Osten, J. Klatt, G. Lippert, B. Dietrich, and E. Bugiel, Phys. Rev. Lett. **69**, 450 (1992).

104. D. J. Eaglesham, F. C. Unterwald, and D. C. Jacobson, Phys. Rev. Lett. **70**, 966 (1993).

105. K. Uchida, T. Tang, S. Goto, T. Mishima, A. Niwa, and J. Gotoh, Appl. Phys. Lett. **74**, 1153 (1999).

106. Y. P. Varshni, Physica **34**, 149 (1967).

107. W. Shan, T. J. Schmidt, X. H. Yang, S. J. Hwang, J. J. Song, and B. Goldenberg, Appl. Phys. Lett. **66**, 985 (1995).

108. W. Shan, B. D. Little, J. J. Song, Z. C. Feng, M. Schurman, and R. A. Stall, Appl. Phys. Lett. **69**, 3315 (1996).

109. K. G. Zolina, V. E. Kudryashov, A. N. Turkin, and A. E. Yunovich, MRS Internet J. Nitride Semicond. Res. **1**, 11 (1996).

110. P. G. Eliseev, P. Perlin, J. Lee, and M. Osinski, Appl. Phys. Lett. **71**, 569 (1997).

111. Y. H. Cho, G. H. Gainer, A. J. Fischer, J. J. Song, S. Keller, U. K. Mishra, and S. P. DenBaars, Appl. Phys. Lett. **73**, 1370 (1998).

112. Y. H. Cho, B. D. Little, G. H. Gainer, J. J. Song, S. Keller, U. K. Mishra, and S. P. DenBaars, MRS Internet J. Nitride Semicond. Res. **4S1**, G2.4 (1999).

113. F. A. J. M. Driessen, G. J. Bauhuis, S. M. Olsthoorn, and L. J. Giling, Phys. Rev. B **48**, 7889 (1993).

114. K. Yamashita, T. Kita, H. Nakayama, and T. Nishino, Phys. Rev. B **55**, 4411 (1997).

115. A. Chomette, B. Deveaud, A. Regreny, and G. Bastard, Phys. Rev. Lett. **57**, 1464 (1986).

116. T. Yamamoto, M. Kasu, S. Noda, and A. Sasaki, J. Appl. Phys. **68**, 5318 (1990).

117. H. Shoji, Y. Nakata, K. Mukai, Y. Sugiyama, M. Sugawara, N. Yokoyama, and H. Ishikawa, Appl. Phys. Lett. **71**, 193 (1997).

118. P. D. Floyd and D. W. Treat, Appl. Phys. Lett. **70**, 2493 (1997).

119. H. Jeon, J. Ding, A. V. Nurmikko, W. Xie, D. C. Grillo, M. Kobayashi, R. L. Gunshor, G. C. Hua, and N. Otsuka, Appl. Phys. Lett. **60**, 2045 (1992).

120. J. M. Gaines, R. R. Drenten, K. W. Haberern, T. Marshall, P. Mensz, and J. Petruzzello, Appl. Phys. Lett. **62**, 2462 (1993).

121. Y. H. Cho, J. J. Song, S. Keller, U. K. Mishra, and S. P. DenBaars, Appl. Phys. Lett. **73**, 3181 (1998).

122. T. J. Schmidt, Y. H. Cho, S. Bidnyk, J. J. Song, S. Keller, U. K. Mishra, and S. P. DenBaars, SPIE Proc. Ultrafast Phenomena in Semiconductors III **3625**, 57 (1999).

123. T. Deguchi, T. Azuhata, T. Sota, S. Chichibu, M. Arita, H. Nakanishi, and S. Nakamura, Semicond. Sci. Technol. **13**, 97 (1998).

124. T. J. Schmidt, S. Bidnyk, Y. H. Cho, A. J. Fischer, J. J. Song, S. Keller, U. K. Mishra, and S. P. DenBaars, Appl. Phys. Lett. **73**, 3689 (1998).

125. T. J. Schmidt, S. Bidnyk, Y. H. Cho, A. J. Fischer, J. J. Song, S. Keller, U. K. Mishra, and S. P. DenBaars, MRS Internet J. Nitride Semicond. Res. **4S1**, G6.54 (1999).

126. N. Peyghambarian, S. W. Koch, and A. Mysyrowicz, *Introduction to Semiconductor Optics*, (Prentice-Hall, Inc., Englewood Cliffs, New Jersey, 1993).

127. G. Mohs, T. Aoki, M. Nagai. R. Shimano, M. Kuwata-Gonokami, and S. Nakamura, Proceedings of the 2nd International Conference on Nitride Semiconductors, Tokushima, Japan, 234 (1997).

128. M. P. Mack, A. Abare, M. Aizcorbe, P. Kozodoy, S. Keller, U. K. Mishra, L. Coldren, and S. P. DenBaars, MRS Internet J. Nitride Semicond. Res. **2**, 41 (1997).

129. J. J. Song and W. Shan, *Group III Nitride Semiconductor Compounds: Physics and Applications*, Edited by B. Gil, (Oxford Univ. Press, New York, 1998), pp. 182-241.

130. J. J. Song and W. Shan, *Properties, Processing, and Applications of Gallium Nitride and Related Semiconductors*, Edited by J. H. Edgar, S. Strite, I. Akasaki, H. Amano, and C. Wetzel (Michael Faraday House, London, 1999), pp. 596-602.

131. K. L. Shaklee and R. F. Leheny, Appl. Phys. Lett. **18**, 475 (1971).

132. K. L. Shaklee, R. E. Nahory, and R. F. Leheny, J. Lumin. **7**, 284 (1973).

133. T. J. Schmidt, J. J. Song, Y. C. Chang, B. Goldenberg, and R. Horning, Appl. Phys. Lett. **72**, 1504 (1998).

134. T. J. Schmidt, Y. C. Chang, and J. J. Song, SPIE Conf. Proc. **3419**, 61 (1998).

135. T. Breitkopf, H. Kalt, C. Klingshirn, and A. Reznitsky, J. Opt. Soc. Am. B. **13**, 1251 (1996).

136. A. Usui, H. Sunakawa, A. Sakai, and A. A. Yamaguchi, Jpn. J. Appl. Phys. Part 2 **36**, L899 (1997).

137. O. H. Nam, M. D. Bremser, T. S. Zheleva, and R. F. Davis, Appl. Phys. Lett. **71**, 2638 (1997).

138. S. Nakamura, M. Senoh, S. I. Nagahama, H. Iwasa, T. Yamada, T. Matsushita, H. Kiyoku, Y. Sugimoto, T. Kozaki, H. Umemoto, M. Sano, and K. Chocho, Appl. Phys. Lett. **72**, 211 (1998).

139. J. A. Smart, E. M. Chumbes, A. T. Schremer, and J. R. Shealy, Appl. Phys. Lett. **75**, 3820 (1999).

140. D. I. Florescu, V. M. Asnin, F. H. Pollak, A. M. Jones, J. C. Ramer, M. J. Schurman, and I. Ferguson, Appl. Phys. Lett. **77**, 1464 (2000).

141. K. Motoki, T. Okahisa, N. Matsumoto, M. Matsushima, H. Kimura, H. Kasai, K. Takemoto, K. Uematsu, T. Hirano, M. Nakayama, S. Nakahata, M. Ueno, D. Hara, Y. Kumagai, A. Koukitu, and H. Seki, Jpn. J. Appl. Phys. Part 2, **40**, L140 (2001).

142. S. Nagahama, N. Iwasa, M. Senoh, T. Matsushita, Y. Sugimoto, H. Kiyoku, T. Kozaki, M. Sano, H. Matsumura, H. Umemoto, K. Chocho, and T. Mukai, Jpn. J. Appl. Phys. Part 2, **39**, L647 (2000).

143. T. Tojyo, T. Asano, M. Takeya, T. Hino, S. Kijima, S. Goto, S. Uchida, and M. Ikeda, Jpn. J. Appl. Phys. Part 1, **40**, 3206 (2001).

144. M. Hansen, P. Fini, L. Zhao, A. C. Abare, L. A. Coldren, J. S. Speck, and S. P. DenBaars, Appl. Phys. Lett. **76**, 529 (2000).

145. C. Sasaoka, H. Sunakawa, A. Kimura, M. Nido, A. Usui, and A. Sakai, J. Cryst. Growth **189/190**, 61 (1998).

146. T. Mukai, K. Takekawa, and S. Nakamura, Jpn. J. Appl. Phys. Part 2, **37**, L839 (1998).

147. T. Mukai, M. Yamada, and S. Nakamura, Jpn. J. Appl. Phys. Part 1, **38**, 3976 (1999).

148. T. Mukai and S. Nakamura, Jpn. J. Appl. Phys. Part 1, **38**, 5735 (1999).

149. J. Pankove, *Properties, Processing, and Applications of Gallium Nitride and Related Semiconductors*, Edited by J. H. Edgar, S. Strite, I. Akasaki, H. Amano, and C. Wetzel (Michael Faraday House, London, 1999), pp. 632-633.

150. A. A. Yamaguchi, Y. Mochizuki, and M. Mizuta, Jpn. J. Appl. Phys. Part 1, **39**, 2402 (2000).

151. A. A. Yamaguchi, M. Kuramoto, A. Kimura, M. Nido, and M. Mizuta, Jpn. J. Appl. Phys. Part 2, **40**, L548 (2001).

152. S. L. Chuang, *Physics of Optoelectronic Devices*, (Wiley, New York, 1995), pp 419-421.

153. D. Wood, *Optoelectronic Semiconductor Devices*, (Prentice Hall, New York, 1994), pp 173-176.

154. K. Domen and A. Kuramata, *Properties, Processing, and Applications of Gallium Nitride and Related Semiconductors*, Edited by J. H. Edgar, S. Strite, I. Akasaki, H. Amano, and C. Wetzel (Michael Faraday House, London, 1999), pp. 607-615.

155. T. Tanaka, K. Uchida, A. Watanabe, and S. Minagawa, Appl. Phys. Lett. **68**, 976 (1996).

156. M. A. Khan, J. W. Yang, G. Simin, R. Gaska, M. S. Shur, H. C. zur Loye, G. Tamulaitis, A. Zukauskas, D. J. Smith, D. Chandrasekhar, and R. B. Tassius, Appl. Phys. Lett. **76**, 1161 (2000).

APPENDICES

APPENDIX A

PUBLICATIONS RELATED TO THIS THESIS

"Well thickness dependence of emission from GaN/AlGaN separate confinement heterostructures," G. H. Gainer, Y. H. Kwon, J. B. Lam, S. Bidnyk, A. Kalashyan, J. J. Song, S. C. Choi and G. M. Yang, Appl. Phys. Lett. **78**, 3890 (2001).

"Time-resolved photoluminescence of InGaN/GaN multiple quantum well structures: effect of Si doping in the barriers," C. K. Choi, Y. H. Kwon, B. D. Little, G. H. Gainer, J. J. Song, Y. C. Chang, S. Keller, U. K. Mishra, and S. P. DenBaars, (submitted to Phys. Rev. B on 3/27/01).

"MOCVD InGaN/GaN MQWs growth interruption effects," T. Sugahara, S. K. Shee, G. H. Park, S. J. Hwang, G. H. Gainer, J. J. Song, and S. Sakai, (submitted to J. Cryst. Growth on 3/22/01).

"Optical properties and lasing in (In,Al)GaN-based structures," S. Bidnyk, G. H. Gainer, S. K. Shee, J. B. Lam, B. D. Little, T. Sugahara, J. Krasinski, Y. H. Kwon, G. H. Park, S. J. Hwang, J. J. Song, G. E. Bulman, and H. S. Kong, phys. stat. sol. (a) **183**, 105 (2001).

"Comparative study of HVPE- and MOCVD-grown nitride structures for UV lasing application," J. B. Lam, G. H. Gainer, S. Bidnyk, Amal Elgawadi, G. H. Park, J. Krasinski, J. J. Song, D. V. Tsvetkov, and V. A. Dmitriev, Mat. Res. Soc. Symp. **639**, G6.4 (2001).

"Optical Properties of (Al)GaN-Based Structures for Near- and Deep-Ultraviolet Emitters," S. Bidnyk, J. B. Lam, B. D. Little, G. H. Gainer, Y. H. Kwon, J. J. Song, G. E. Bulman, and H. S. Kong (submitted to Jpn. J. Appl. Phys. in 9/00).

"MOCVD growth, stimulated emission and time resolved PL studies of InGaN/(In)GaN MQWs: well and barrier thickness dependence," S. K. Shee, Y. H. Kwon, J. B. Lam, G. H. Gainer, G. H. Park, S. J. Hwang, B. D. Little, and J. J. Song, J. Cryst. Growth **221**, 373 (2000).

"Optical properties of (Al)GaN-based structures for near- and deep-ultraviolet emitters," S. Bidnyk, J. B. Lam, Y. H. Kwon, G. H. Gainer, B. D. Little, and J. J. Song, Proc. Int. Workshop on Nitride Semiconductors (IWN2000), IPAP Conf. Series 1, 567 (2000).

"Linear and nonlinear optical properties of InGaN/GaN heterostructures," Y. H. Cho, T. J. Schmidt, S. Bidnyk, G. H. Gainer, J. J. Song, S. Keller, U. K. Mishra, and S. P. DenBaars, Phys. Rev. B **61,** 7571 (2000).

"Dynamics of anomalous optical transition in Al$_x$Ga$_{1-x}$N alloys," Y. H. Cho, G. H. Gainer, J. B. Lam, J. J. Song, Phys. Rev. B **61**, 7203 (2000).

"Study of gain mechanisms in AlGaN in the temperature range of 30-300 K," J. B. Lam, S. Bidnyk, G. H. Gainer, B. D. Little, J. J. Song, and W. Yang, Appl. Phys. Lett. **77**, 4101 (2000).

"Time-resolved study of yellow and blue luminescence in Si- and Mg-doped GaN," Yong-Hwan Kwon, S. K. Shee, G. H. Gainer, G. H. Park, S. J. Hwang, and J. J. Song, Appl. Phys. Lett. **76**, 840 (2000).

"Study of gain mechanisms in Al$_x$Ga$_{1-x}$N in the temperature range of 30 to 300 K," J. B. Lam, S. Bidnyk, G. H. Gainer, B. D. Little, J. J. Song, and W. Yang, Conference on Lasers and Electro-Optics (CLEO) 2000 Technical Digest, CMG1 (2000).

"GaN/AlGaN SCH UV semiconductor lasers: Effect of GaN well thickness on lasing efficiency," G. H. Gainer, Y. H. Kwon, J. B. Lam, A. Kalashyan, J. J. Song, S. C. Choi, and G. M. Yang, Conference on Lasers and Electro-Optics (CLEO) 2000 Technical Digest, CMG4 (2000).

"A comparative study of AlGaN and GaN-based lasing structures for near- and deep-UV applications," S. Bidnyk, J. B. Lam, G. H. Gainer, B. D. Little, Y. H. Kwon, J. J. Song, G. E. Bulman, and H. S. Kong, Mat. Res. Soc. Symp. Proc. T3.8, 316 (2000).

"Comparison study of structural and optical properties of In$_x$Ga$_{1-x}$N/GaN quantum wells with different In compositions," Y. H. Kwon, G. H. Gainer, S. Bidnyk, Y. H. Cho, J. J. Song, M. Hansen, and S. P. DenBaars, Mat. Res. Soc. Symp. Proc. **595** and MRS Internet J. Nitride Semicond. Res. **5S1**, W12.7 (2000).

"Dynamics of anomalous temperature-induced emission shift in MOCVD-grown (Al, In)GaN thin films," Y. H. Cho, G. H. Gainer, J. B. Lam, J. J. Song, W. Yang, and W. Jhe, Mat. Res. Soc. Symp. Proc. **595** and MRS Internet J. Nitride Semicond. Res. **5S1**, W11.57 (2000).

"Microstructure-based lasing in GaN/AlGaN separate confinement heterostructures," S. Bidnyk, J. B. Lam, B. D. Little, G. H. Gainer, Y. H. Kwon, J. J. Song, G. E. Bulman, and H. S. Kong, Mat. Res. Soc. Symp. Proc. **595**, W11.22 (1999); MRS Internet J. Nitride Semicond. Res. **5S1**, W11.22 (2000).

"Comparative study of near-threshold gain mechanisms in GaN epilayers and GaN/AlGaN separate confinement heterostructures," S. Bidnyk, J. B. Lam, B. D. Little, G. H. Gainer, Y. H. Kwon, J. J. Song, G. E. Bulman, and H. S. Kong, The International Society for Optical Engineering (SPIE) Conf. Proc. **3947**, 126 (2000).

"Structural and optical characteristics of In$_x$Ga$_{1-x}$N/GaN multiple quantum wells with different In compositions," Y. H. Kwon, G. H. Gainer, S. Bidnyk, Y. H. Cho, J. J. Song, M. Hansen, and S. P. DenBaars, Appl. Phys. Lett. **75**, 2545 (1999).

"Critical issues of localization in the development of InGaN/GaN laser diodes," S. Bidnyk, Y.-H. Cho, T. J. Schmidt, G. H. Gainer, J. J. Song, S. Keller, U. K. Mishra,

S. P. DenBaars, W. Jhe, Proceedings of Conference on Lasers and Electro-Optics (CLEO)/Pacific Rim '99, Technical Digest **2**, 286 (1999).

"Comparison of spontaneous and stimulated emission from UV-blue photonic materials," B. D. Little, Y.-H. Cho, T. J. Schmidt, G. H. Gainer, J. B. Lam, J. J. Song, W. Yang, S. Keller, U. K. Mishra, S. P. DenBaars, W. Jhe, Proceedings of Conference on Lasers and Electro-Optics (CLEO)/Pacific Rim '99, Technical Digest **2**, 290 (1999).

"Carrier recombination dynamics of $Al_xGa_{1-x}N$ epilayers grown by MOCVD," Y. H. Cho, G. H. Gainer, J. B. Lam, J. J. Song, W. Yang, and S. A. McPherson, Mat. Res. Soc. Symp. Proc. **572**, 457 (1999).

"Carrier dynamics of abnormal temperature-dependent emission shift in MOCVD-grown InGaN epilayers and InGaN/GaN quantum wells," Y. H. Cho, B. D. Little, G. H. Gainer, J. J. Song, S. Keller, U. K. Mishra, and S. P. DenBaars, MRS Internet J. Nitride Semicond. Res. **4S1**, G2.4 (1999).

"Effects of carrier localization on the optical characteristics of MOCVD-grown InGaN/GaN heterostructures," Y. H. Cho, T. J. Schmidt, A. J. Fischer, S. Bidnyk, G. H. Gainer, J. J. Song, S. Keller, U. K. Mishra, S. P. DenBaars, D. S. Kim, and W. Jhe, phys. stat. sol. **216**, 181 (1999).

"A comparison of the optical characteristics of AlGaN, GaN, and InGaN thin films," Y. H. Cho, T. J. Schmidt, G. H. Gainer, J. B. Lam, J. J. Song, S. Keller, U. K. Mishra, S. P. DenBaars, W. Yang, D. S. Kim, and W. Jhe, phys. stat. sol. **216**, 227 (1999).

"Time-resolved photoluminescence studies of GaN, InGaN, and AlGaN grown by metalorganic chemical vapor deposition," Y. H. Cho, G. H. Gainer, J. J. Song, S. Keller, U. K. Mishra, S. P. DenBaars, W. Yang, and S. A. McPherson, The International Society for Optical Engineering (SPIE) Conf. Proc., *Ultrafast Phenomena in Semiconductors III*, **3624**, 283 (1999).

"Optical characteristics of group III nitride quantum structures," Y. H. Cho, W. Jhe, T. J. Schmidt, S. Bidnyk, G. H. Gainer, and J. J. Song, Proceedings of the 3rd Korea-China Joint Workshop on Advanced Materials, (invited), 351 (1999).

"Comparison of spontaneous and stimulated emission from UV-blue photonics materials," B.D. Little, Y.H. Cho, T.J. Schmidt, G.H. Gainer, J.B. Lam, J.J. Song, W. Yang, S. Keller, U.K Mishra, S.P. DenBaars, and W. Jhe, Conference on Laser and Electro-Optics, CLEO/Pacific Rim '99, Technical Digest vol 2, 290 (1999).

"Nonlinear optical spectroscopy of highly excited InGaN/GaN multiple quantum well blue laser structures," T.J. Schmidt, S. Bidnyk, Y.H. Cho, G.H. Gainer, J.J. Song, 1999 CLEO Technical Digest Series, CtuU4, 202 (1999).

"Pump-probe spectroscopy of band tail states in metalorganic chemical vapor deposition-grown InGaN," T.J. Schmidt, Y.H. Cho, G.H. Gainer, J.J. Song, S. Keller, U.K. Mishra, and S.P. DenBaars, Appl. Phys. Lett. **73**, 1892 (1998).

125

"Energy selective optically pumped stimulated emission from InGaN/GaN multiple quantum wells," T.J. Schmidt, Y.H. Cho, G.H. Gainer, J.J. Song, S. Keller, U.K. Mishra, and S.P. DenBaars, Appl. Phys. Lett. **73**, 560 (1998).

"S-shaped temperature-dependent emission shift and carrier dynamics in InGaN/GaN multiple quantum wells," Y.H. Cho, G.H. Gainer, A.J. Fischer, J.J. Song, S. Keller, U.K. Mishra, and S.P. DenBaars, Appl. Phys. Lett. **73**, 1370 (1998).

"High-temperature stimulated emission in optically pumped InGaN/GaN multi-quantum wells," S. Bidnyk, T.J. Schmidt, Y.H. Cho, G.H. Gainer, J.J. Song, S. Keller, U.K. Mishra and S.P. DenBaars, Appl. Phys. Lett. **72**, 1623 (1998).

APPENDIX B

CONFERENCE PRESENTATIONS RELATED TO THIS THESIS

"Effect of well thickness on GaN/AlGaN separate confinement heterostructure emission," G. H. Gainer, Y. H. Kwon, J. B. Lam, S. Bidnyk, A. Kalashyan, J. J. Song, S. C. Choi, and G. M. Yang, Fourth International Conference on Nitride Semiconductors (ICNS-4), P10.2, Denver, CO, (July 16 – 20, 2001).

"The excitonic ac Stark effect in a GaN epilayer," C. K. Choi, J. B. Lam, G. H. Gainer, S. K. Shee, J. J. Song, and Y. C. Chang, Fourth International Conference on Nitride Semiconductors (ICNS-4), P19.22, Denver, CO, (July 16 – 20, 2001).

"MOCVD growth interruption effects on InGaN/GaN MQWs," T. Sugahara, S. K. Shee, G. H. Park, S. J. Hwang, G. H. Gainer, J. J. Song, and S. Sakai, Fourth International Conference on Nitride Semiconductors (ICNS-4), A3.5, Denver, CO, (July 16 – 20, 2001).

"Temperature dependence of transmission and emission spectra in MOCVD-grown AlGaN ternary alloys," Y. H. Cho, G. H. Gainer, J. B. Lam, J. J. Song, and W. Yang, Fourth International Conference on Nitride Semiconductors (ICNS-4), P17.9, Denver, CO, (July 16 – 20, 2001).

"Optical properties and lasing in (In,Al)GaN-based structures," J. J. Song, S. Bidnyk, J. B. Lam, G. H. Gainer, and Y. H. Kwon, ISPSA 2000 (invited), Cheju, Korea (November 1 – 3, 2000).

"Absorption, emission, and carrier dynamics study of MOCVD-grown $Al_xGa_{1-x}N$ Alloys," Y. H. Cho, G. H. Gainer, J. B. Lam, J. J. Song, W. Yang, and T. W. Kang, ISPSA 2000, Cheju, Korea (November 1 –3, 2000).

"Optical properties and lasing in (In,Al)GaN-based structures," S. Bidnyk, J. B. Lam, Y. H. Kwon, G. H. Gainer, S. K. Shee, G. H. Park, S. J. Hwang, B. D. Little, and J. J. Song, International Workshop on Physics of Light-matter Coupling in Nitrides, France (October 8 – 12, 2000).

"Optical properties of (Al)GaN-based structures for near- and deep-ultraviolet emitters," S. Bidnyk, J. B. Lam, Y. H. Kwon, G. H. Gainer, B. D. Little, and J. J. Song, Int. Workshop on Nitride Semicond. (IWN2000), TA2-3, Nagoya, Japan (September 24 - 27, 2000).

"MOCVD growth, stimulated emission and time resolved PL studies of InGaN/(In)GaN MQWs: well and barrier thickness dependence," S. K. Shee, Y. H. Kwon, J. B. Lam, G. H. Gainer, G. H. Park, S. J. Hwang, B. D. Little, J. J. Song, The Tenth International Conference on Metalorganic Vapor Phase Epitaxy (ICMOVPE-X), Sapporo, Japan (June 5 - June 9, 2000).

"Study of gain mechanisms in $Al_xGa_{1-x}N$ in the temperature range of 30 to 300 K," J. B. Lam, S. Bidnyk, G. H. Gainer, B. C. Little, J. J. Song, and W. Yang, Conference on Lasers and Electro-Optics (CLEO) 2000, CMG1, 76, San Francisco, CA (May 7 - 12, 2000).

"GaN/AlGaN SCH UV semiconductor lasers: Effect of GaN well thickness on lasing efficiency," G. H. Gainer, Y. H. Kwon, J. B. Lam, A. Kalashyan, J. J. Song, S. C. Choi and G. M. Yang, Conference on Lasers and Electro-Optics (CLEO) 2000, CMG4, San Francisco, CA (May 7 - 12, 2000).

"Comparative study of gain mechanisms in GaN epilayers and GaN/AlGaN separate confinement heterostructures," S. Bidnyk, J. B. Lam, B. D. Little, G. Gainer, J. J. Song, American Physical Society March Meeting, R17.10, 739, Minneapolis, MN (March 20-24, 2000).

"Study of stimulated emission in AlGaN thin films in the temperature range of 30 K to 300 K," J. B. Lam, S. Bidnyk, G. Gainer, B. Little, J. J. Song, and W. Yang, American Physical Society March Meeting, R17.11, 740, Minneapolis, MN (March 20-24, 2000).

"Comparative study of near-threshold gain mechanisms in GaN epilayers and GaN/AlGaN separate confinement heterostructures," S. Bidnyk, J. B. Lam, B. D. Little, G. H. Gainer, Y. H. Kwon, and J. J. Song, The International Society for Optical Engineering (SPIE) Photonics West 2000, 3947-24, 126, San Jose, CA (January 23-28, 2000).

"Dynamics of anomalous temperature-induced emission shift in MOCVD-grown (Al, In)GaN thin films," Yong-Hoon Cho, G. H. Gainer, J. B. Lam, J. J. Song, W, Yang, and W. Jhe, Mat. Res. Soc. Fall 99, Boston, MA (November 29 - December 3, 1999).

"Mechanism of efficient ultraviolet lasing in a GaN/AlGaN separate confinement heterostructure," S. Bidnyk, J. B. Lam, B. D. Little, G. H. Gainer, Y. H. Kwon, J. J. Song, G. E. Bulman, and H. S. Kong, Mat. Res. Soc. Fall 99, Boston, MA (November 29 - December 3, 1999).

"Comparison study of structural and optical properties of $In_xGa_{1-x}N$/GaN quantum wells with different In compositions," Yong-Hwan Kwon, G. H. Gainer, S. Bidnyk, Y. H. Cho, J. J. Song, M. Hansen, and S. P. DenBaars, Mat. Res. Soc. Fall 99, Boston, MA (November 29 - December 3, 1999).

"Optical characteristics of group III nitride quantum structures," (invited), Yong-Hoon Cho and W. Jhe (Center for Near-field Atom-photon Technology and Department of Physics, Seoul National University), T. J. Schmidt, S. Bidnyk, G. H. Gainer, and J. J. Song (Center for Laser and Photonics Research and Department of Physics,

Oklahoma State University), 3rd Korea-China Joint Workshop on Advanced Materials, Cheju, Korea (August 23–27, 1999).

"Optical emission characteristics of GaAs and GaN based materials using near-field and far-field optics," (invited) Yong-Hoon Cho, Sang-Kee Eah, S. C. Hohng, D. S. Kim, W. Jhe (Seoul National University) T. J. Schmidt, S. Bidnyk, G. H. Gainer, and J. J. Song (Oklahoma State University), Korea Physics Society 99 Fall Meeting, I-05, Korea (October 15–16, 1999).

"Comparison of spontaneous and stimulated emission from UV-blue photonic materials," B. D. Little, Y.-H. Cho, T. J. Schmidt, G. H. Gainer, J. B. Lam, J. J. Song, W. Yang, S. Keller, U. K. Mishra, S. P. DenBaars, and W. Jhe, Conference on Lasers and Electro-Optics (CLEO)/Pacific Rim '99, WP5, Seoul, Korea (August 30 - September 3, 1999).

"Critical issues of localization in the development of InGaN/GaN laser diodes," S. Bidnyk, Y.-H. Cho, T. J. Schmidt, G. H. Gainer, J. J. Song, S. Keller, U. K. Mishra, S. P. DenBaars, and W. Jhe, Conference on Lasers and Electro-Optics (CLEO)/Pacific Rim '99, WP3, Seoul, Korea (August 30 - September 3, 1999).

"Effects of carrier localization on the optical characteristics of MOCVD-grown InGaN/GaN heterostructures," Y. H. Cho, T. J. Schmidt, A. J. Fischer, S. Bidnyk, G. H. Gainer, J. J. Song, S. Keller, U. K. Mishra, S. P. DenBaars, D. S. Kim, and W. Jhe, The Third International Conference on Nitride Semiconductors (ICNS3), We P093, Montpellier, France (July 5-9, 1999).

"A comparison of the optical characteristics of AlGaN, GaN, and InGaN thin films," Y. H. Cho, T. J. Schmidt, G. H. Gainer, J. B. Lam, J. J. Song, S. Keller, U. K. Mishra, S. P. DenBaars, W. Yang, D. S. Kim, and W. Jhe, The Third International Conference on Nitride Semiconductors (ICNS3), Montpellier, France (July 5-9, 1999).

"Carrier recombination dynamics of Al$_x$Ga$_{1-x}$N epilayers grown by MOCVD," Y. H. Cho, G. H. Gainer, J. B. Lam, J. J. Song, W. Yang, and S. A. McPherson, Mat. Res. Soc. Spring Meeting, San Francisco, CA (April 5-9, 1999).

"Time-resolved photoluminescence studies of GaN, InGaN, and AlGaN grown by metalorganic chemical vapor deposition," Y.H. Cho, G.H. Gainer, J.J. Song, S. Keller, U.K. Mishra, S.P. DenBaars, W. Yang, and S.A. McPherson, SPIE Proc., *Ultrafast Phenomena in Semiconductors III*, The International Society for Optical Engineering (SPIE) Photonics West 1999, 3624, San Jose, CA (January 25-29, 1999).

"Carrier dynamics of abnormal temperature-dependent emission shift in MOCVD-grown InGaN epilayers and InGaN/GaN quantum wells," Y.H. Cho, B.D. Little, G.H. Gainer, J.J. Song, S. Keller, U.K. Mishra, and S.P. DenBaars, Mat. Res. Soc. Symp. Proc. Fall (1998).

"Effect of Si doping on the optical properties of InGaN/GaN multiple quantum wells," Y.H. Cho, G.H. Gainer, J.J. Song, S. Keller, U.K. Mishra, and S.P. DenBaars, OSA Annual Meeting ILS-XIV: 14th Interdisciplinary Laser Science Conference, Baltimore, Maryland (1998).

"S-shaped temperature dependent emission shift and carrier dynamics in MOCVD-grown InGaN/GaN multiple quantum wells," Y.H. Cho, G.H. Gainer, A.J. Fischer, J.J. Song, S. Keller, U.K. Mishra, and S.P. DenBaars, APS March Meeting, **43**, 87 [C18.05] (1998).

VITA ∂

Gordon H. Gainer, Jr.

Candidate for the Degree of

Doctor of Philosophy

Thesis: EMISSION MECHANISMS OF InGaN-BASED III-NITRIDE
HETEROSTRUCTURES

Major Field: Physics

Biographical:

Personal Data: Born in Newark, Ohio on January 16, 1960, the son of Gordon H.
Gainer, Sr. and Caroline Gainer.

Education: Graduated from Heath High School, Heath, Ohio in May 1978; received
a Bachelor of Science degree in Engineering Physics from The Ohio State
University, Columbus, Ohio in June 1982; obtained a Master of Science
Degree in Engineering Physics from the Air Force Institute of Technology,
Wright-Patterson AFB, Ohio in December 1987. Completed the requirements
for the Doctor of Philosophy Degree with a major in Physics at Oklahoma
State University in August 2001.

Professional Experience: Project Officer and Program Manager in the U. S. Air
Force, September 1982 to April 1995; Research Assistant, Department of
Physics and Center for Laser and Photonics Research, Oklahoma State
University, January 1996 to present.

Professional Memberships: American Physical Society.